

**Exploratory Experiments to Determine Effects of Injected Aerosolized Water,  
Hydrochloric Acid, and Sodium Chloride Solutions on Lab-Scale Flare Emissions**

by

**Amy Melina Jefferson**

A thesis submitted to The Faculty of Graduate Studies and Research

in partial fulfilment of the degree requirements of

**Master of Applied Science in Mechanical Engineering**

Ottawa-Carleton Institute for

Mechanical and Aerospace Engineering

Department of Mechanical and Aerospace Engineering

Carleton University

Ottawa, Ontario, Canada

April 2017

Copyright © 2017 – Amy Melina Jefferson

The undersigned recommend to  
the Faculty of Graduate Studies and Research  
acceptance of the thesis

Exploratory Experiments to Determine Effects of Injected Aerosolized Water,  
Hydrochloric Acid, and Sodium Chloride Solutions on Lab Scale Flare Emissions

Submitted by **Amy Melina Jefferson**

in partial fulfilment of the requirements for the degree of

**Master of Applied Science in Mechanical Engineering**

---

Dr. Matthew Johnson, Thesis Supervisor

---

Dr. Ronald Miller, Chair, Department of Mechanical and Aerospace Engineering

Carleton University

2017

# Abstract

During the flowback process of well-completion at hydraulic fracturing sites, there is the potential for liquid aerosol carry-over into gases sent to a flare. This thesis presents an exploratory investigation into the potential effects of non-hydrocarbon aerosols on flare emissions based on controlled experiments on lab-scale flares. Combustion emission and particulate matter optical properties were measured from lab-scale flares injected with industry relevant aerosolized liquids (water, aqueous HCl, and aqueous NaCl). Effects of liquid concentration, droplet size and liquid loading were compared to dry and distilled water base cases. Concentrations of NaCl (5%<sub>m</sub> and 15%<sub>m</sub>) and HCl (3.17%<sub>m</sub> and 9.51%<sub>m</sub>) solutions were chosen to match chlorine content, and liquid loadings up to 14.3% (kg/kg flare gas × 100%) were tested.

Generally, water and HCl caused similar and relatively weak changes in gas-phase species yields relative to dry flame emission results. Conversely, NaCl solutions affected gas-phase measurements significantly: CO yields increased up to a factor of 25 and NO<sub>x</sub> yields decreased by 26% compared to that of dry flame results. Methane emissions were zero for all cases except those with injected NaCl aerosols.

Particulate matter emission rates and optical properties were effectively identical for dry flames and flames with water and HCl aerosols at all tested liquid loadings and concentrations considered in the study. However, NaCl test results indicated that liquid loading and concentration affected both the amount and form of the particulate. Absorption coefficient, scattering coefficient, and soot yield results indicated that these augmented

particulate emissions may include stand-alone, highly scattering NaCl particles as well as increased amounts of light absorbing particles such as internally mixed NaCl-soot particles.

Overall, the results in this thesis have shown that entrained aerosols can profoundly affect emissions of lab-scaled flares and demonstrate the need for further investigation to determine whether there are potential alterations in flare emissions at conditions that may be occurring during flowback operations in the field.

# Acknowledgements

To my supervisor, Prof. Johnson, thank you for being supportive, encouraging, and for always taking the time to work through all the issues I ran into.

To my Energy and Emissions Research Lab colleagues: Jay, Nick H., Nick B., Dave, Brian, Simon, Steve, Carol, and especially Darcy. Thank you for all your support and it has been a pleasure working with all of you.

To my supporters in the Mechanical and Aerospace department: Irene and Janet in the office for their help with all my questions/room bookings/extension forms, Neil and Bruce for unlocking my MAENT account more times than reasonable to ask over 2.5 years, and Alex, Ian, and Kevin in the shop, and Steve and Dave in the lab for their above and beyond help with any machining or odd jobs.

To my family, for putting up with my request for edits and advice and my complaints of whichever instrument was broken at the time, and for being my cheerleaders, I love you all so much.

And finally, thank you to my friends, who tried so hard (with minimal success) to improve my work-life balance.

# Contents

Abstract .....	3
Acknowledgements.....	5
List of Tables .....	8
List of Figures.....	9
Nomenclature.....	16
Chapter 1 Introduction.....	18
1.1 Hydraulic Fracturing Fluids .....	20
1.2 Flowback Fluids.....	24
1.2.1 U.S. and Canadian Regulations for the Disposal of FB and PW Liquids and Gases .....	30
1.3 Flaring .....	32
1.4 Potential Effects of Entrained Aerosols on Flare Emissions.....	34
1.5 Thesis Motivation and Objectives.....	40
Chapter 2 Experimental Setup.....	42
2.1 Carleton University Lab Scale Flare (CLSF) Facility.....	42
2.1.1 Fuel Delivery .....	44
2.1.2 Burner and Aerosol Generation .....	46
2.1.3 Ultrasonic Atomizers .....	49
2.2 Gas and Solid-Phase Combustion Emissions Measurements .....	53
2.2.1 Nitrogen Oxides (NO <sub>x</sub> ).....	54
2.2.2 Carbon Monoxide, Carbon Dioxide, Methane.....	55
2.2.3 Aerosol Species.....	55
2.2.4 Experimental Methodology .....	59

Chapter 3	Initial Results and Data Reduction .....	61
3.1	Summary and Design of Experiments.....	61
3.2	Repeatability of Aerosol Injection System.....	64
3.2.1	Data Processing and Outlier Detection of 5% and 15% Salt Solution Tests Cases .....	65
Chapter 4	Results and Discussion .....	70
4.1	Effect of Liquid Loading on Carbon Monoxide and Methane Emissions .....	70
4.2	Nitrogen Oxides (NO <sub>x</sub> ).....	77
4.3	Effect of Injected Aerosols on Emitted Particulate Matter .....	80
Chapter 5	Conclusions and Recommendations .....	93
5.1	Future Recommendations.....	95
Appendix A	Machine Drawings of the Atomizing Burner .....	107
Appendix B	Calibration Procedure for Absorption and Scattering Coefficients .....	115
Appendix C	Tap Water Chemical Composition.....	122
Appendix D	Repeatability Tests .....	124
Appendix E	Scattering and Absorption Characteristics at 532 nm and 870 nm .....	132

# List of Tables

Table 1.1: Water-Based Hydraulic Fracturing Fluids: Purpose and Examples of Commonly Used Additives.....	22
Table 2.1: Hydrocarbon fuel MFC specifications and purity .....	46
Table 2.2: Sono-Tek ultrasonic atomizer specifications and operation conditions .....	50
Table 2.3: Gas- and solid-phase combustion emission analyzer specifications and calibration methods.....	54
Table 3.1: Experimental Matrix.....	62
Table 3.2: Summary of Grubbs' Test of outliers (Trial 1, 95% confidence) for repeated tests of 15% NaCl experiments.....	68
Table 4.1: Measured $B_{\text{abs}}$ and $B_{\text{scat}}$ and estimated uncertainties dry cases and tests with 19 $\mu\text{m}$ aerosols of DW, TW, 3.17% HCl, and 9.51% HCl.....	82
Table 4.2: Measured $B_{\text{abs}}$ and $B_{\text{scat}}$ and estimated uncertainties tests with 19 $\mu\text{m}$ and 13 $\mu\text{m}$ aerosols of 5% and 15% NaCl.....	85
Table C.1: Properties and Anion Analysis Results of Aerosolized Tap Water .....	122
Table C.2: Dissolved Metal Analysis Results of Aerosolized Tap Water.....	123

# List of Figures

Figure 1.1: Trends in HF fluids derived from the USGS database for HF fluids in the U.S. (Gallegos and Varela, 2015a). Data for 1,763,800 fracturing treatments from 1947 to 2010 compiled from states reporting hydraulic fracturing treatments; those with over 1000 treatments include TX, OK, PA, OH, NM, CO, WV, KS, WY, KY, LA, CA, IL, MI, UT, NY, AR, MT, AL, VA, IN, ND, NE, MS, TN, AK. ....	21
Figure 1.2: Temporally resolved FB composition of a) TDS, b) chloride, and c) sodium ions, over a span of 44 days. ....	25
Figure 1.3: Box and whisker plot showing median, upper, and lower quartile (red) and maximum and minimum concentrations of various species in formation water. Data are compiled from 599 samples representing 14 formation ages (Dresel and Rose, 2010; Osborn and McIntosh, 2010; Balashov et al., 2015; Hobbs et al., 2011; Worden, 1996; Martini et al., 1998; Cowie et al., 2014; Kharaka and Hanor, 2007; and Dollar et al., 1991). ....	27
Figure 1.4: Plot of Figure 1.2 with overlaid quartiles of FW data compiled from 599 samples. ....	28
Figure 1.5: Flaring Volumes in a) Canada, and b) U.S. Plot b) includes the percentage of oil and gas production in the U.S. from unconventional sources of oil and gas... 33	
Figure 1.6: Transmission electron microscope (TEM) images of particulate matter from work in Kazemimanesh (2014) from : (a) dry flames; (b) DW (74 mL/min); (c) 10% NaCl (74 mL/min) and; 1% HCl (74 mL/min).....	37
Figure 2.1: CLFS facility schematic. Adapted from Corbin (2014). ....	43
Figure 2.2: Fuel supply, conditioning, and delivery and atomizer liquid supply, delivery, and frequency generator. ....	45
Figure 2.3: Custom atomizing burner assembly. ....	47
Figure 2.4: Details of atomizing burner assembly: a) flow straightener located in the atomizing burner, b) custom designed 2-inch burner nozzle, and 1-inch stack, and c) detail of atomizer holder. ....	48
Figure 2.5: Sono-Tek atomizers manufacturer specified droplet diameter distributions for the 120 kHz (red), and 180 kHz (black) atomizers. ....	51
Figure 2.6: Atomizing streams of the 120 kHz nozzle with co-flow of ambient temperature air (20°C) at 0.00175 kg/s (matching the mass flow rate of fuel at 109.45 SLPM) at (a) 2 mL/min and (b) 15 mL/min of distilled water. ....	52
Figure 2.7: Gas- and solid-phase species sampling and exhaust setup. ....	54

- Figure 3.1: (a) CO yield of Heavy 4 flare gas at 109.45 SLPM versus liquid loading of injected 19  $\mu\text{m}$  (nominal) aerosols of 5% (red) and 15% (pink) aqueous NaCl. A comparable dry case (without injected aerosols) is also shown (black). Dotted error bars represent true total uncertainties, solid error bars represents bias, and shaded regions represent an extrapolated total uncertainty for bias-only measurements. Plot (b) is a re-scaled plot of (a) to better illustrate dry and DW test results and uncertainties. .... 64
- Figure 3.2: CO yield of Heavy 4 flare gas at 109.45 SLPM versus liquid loading of 19  $\mu\text{m}$  15% aqueous NaCl. Instrument bias errors are included on each individual data point. Grey diamonds represent the average of the repeated trials at each liquid loading set point. Error bars on the diamonds are the calculated total uncertainty of the average excluding any outliers. .... 66
- Figure 4.1: CO yield vs liquid loading of dry (i.e. 0% loading), DW, TW, 3.17% HCl, and 9.51% HCl aerosols of median diameter of 19  $\mu\text{m}$ . Shaded bands represent approximate total uncertainties and error bars represent instrument bias. True total uncertainties were calculated for: dry; 10% loading of DW indicated by the dotted error bars. .... 71
- Figure 4.2: CO yield vs. liquid loading of dry (i.e. 0% loading), DW, TW, 3.17% HCl, 9.51% HCl, 5% NaCl, and 15% NaCl aerosols of median diameter 19  $\mu\text{m}$ . Shaded bands represent approximate total uncertainties and error bars represent instrument bias. True total uncertainties were calculated for: dry; 10% loading of DW; 7.5% loading of 5% NaCl and; all loadings of 15% NaCl indicated by the dotted error bars. .... 74
- Figure 4.3: CH<sub>4</sub> yield vs liquid loading of dry (i.e. 0% loading), 5% NaCl, and 15% NaCl aerosols of median diameter 19  $\mu\text{m}$ , and 5% NaCl and 15% NaCl aerosols of median diameter 13  $\mu\text{m}$ . Shaded bands represent approximate total uncertainties and error bars represent instrument bias. True total uncertainties were calculated for: dry; 7.5% loading of 5% NaCl (19  $\mu\text{m}$ ) and; all loadings of 15% NaCl (19  $\mu\text{m}$ ) indicated by the dotted error bars. .... 76
- Figure 4.4: CO yield vs liquid loading of dry (i.e. 0% loading), 5% NaCl, and 15% NaCl aerosols of median diameter 19  $\mu\text{m}$ , and 5% NaCl and 15% NaCl aerosols of median diameter 13  $\mu\text{m}$ . Shaded bands represent approximate total uncertainties and error bars represent instrument bias. True total uncertainties were calculated for: dry; 7.5% loading of 5% NaCl (19  $\mu\text{m}$ ) and; all loadings of 15% NaCl (19  $\mu\text{m}$ ) indicated by the error bars. .... 77
- Figure 4.5: NO<sub>x</sub> yield vs liquid loading of dry (i.e. 0% loading), DW, TW, 3.17% HCl, 9.51% HCl, 5% NaCl, and 15% NaCl aerosols of median diameter 19  $\mu\text{m}$ . Shaded bands represent approximate total uncertainties and error bars represent instrument bias. True total uncertainties were calculated for: dry; 10% loading of DW; 7.5% loading of 5% NaCl and; all loadings of 15% NaCl indicated by the dotted error bars. .... 79

Figure 4.6: NO <sub>x</sub> yield vs. liquid loading for 5% NaCl, and 15% NaCl aerosols of median diameter 13 and 19 μm. Shaded bands represent estimated total uncertainties and error bars represent calculated instrument bias. True total uncertainties were calculated for: dry; 7.5% loading of 5% NaCl (19 μm) and; all loadings of 15% NaCl (19 μm) indicated by the dotted error bars. ....	80
Figure 4.7: Absorption (solid fill) and scattering (lighter stacked fill) coefficients vs. liquid loading for flames injected with 19 μm aerosols of DW, TW, 3.17% HCl, and 9.51% HCl. The total extinction is represented by the sum of each component. Total uncertainties are presented in Table 4.1. ....	81
Figure 4.8: Absorption (solid fill) and scattering (lighter stacked fill) coefficients vs. liquid loading of 5% NaCl, and 15% NaCl aerosols of 13 μm and 19 μm median diameter. See Table 4.2 for total uncertainty estimates. ....	84
Figure 4.9: Measured scattering to absorption coefficient ratios at 405 nm for 19 μm aerosols of DW, TW, 3.17% HCl and 9.51% HCl. Error bars represent total uncertainties, which were directly calculated for the dry flame and the flame with 19 μm aerosols of DW at 10% loading. Plotted uncertainties for other cases were estimated based on the measured precision of a similar case. ....	86
Figure 4.10: Measured scattering to absorption coefficient ratios at 405 nm for 13 and 19 μm aerosols of 5% and 15% NaCl solutions. Error bars represent total uncertainties, which were directly calculated for the dry flame and the flames with 19 μm aerosols of 5% NaCl at 7.5% loading and 19 μm aerosols of 15% NaCl at all loadings. Plotted uncertainties for other cases were estimated based on the measured precision of a similar case. ....	87
Figure 4.11: Comparison of soot yields derived from PASS-3 measurements at 405 nm and LII measurements. Results are shown for the dry flame and for flames injected with 19 μm aerosols of DW, TW, and 3.17% and 9.51% HCl solutions. An effective E(m) <sub>λ</sub> value was estimated by scaling the soot yields derived from the PASS-3 measurements to match those derived from the LII measurements. Error bars represent total uncertainties, which were directly calculated for the dry flame and the flame with 19 μm aerosols of DW at 10% loading and dry flames. Plotted uncertainties for other cases were estimated based on the measured precision of a similar case. ....	90
Figure 4.12: Perceived soot yields from the LII measurements versus the PASS-3 measurements at 405 nm from flames with injected 13 and 19 μm aerosols of 5% and 15% NaCl solutions. Error bars represent total uncertainties, which were directly calculated for the 19 μm aerosols of 5% NaCl at 7.5% loading and 19 μm aerosols of 15% NaCl at all loadings. Plotted uncertainties for other cases were estimated based on the measured precision of a similar case. ....	92
Figure A.1: Assembly drawing of atomizing burner .....	107

Figure A.2: Machine drawing of 1” high stack for 2” diameter burner (Units in inches). .....	108
Figure A.3: Machine drawing of 2” exit diameter burner (Units in inches). .....	108
Figure A.4: Machine drawing of the top of the burner body (Units in inches) .....	109
Figure A.5: Machine drawing of turbulence grid (Units in inches).....	109
Figure A.6: Drawing of burner body bottom with four ½” NPT fuel inlet ports (Units in inches).....	110
Figure A.7: Burner base plate with liquid injection port in centre (Units in inches).....	110
Figure A.8: Example assembly of atomizer holder .....	111
Figure A.9: Machine drawing for 120 kHz nozzle holder (Units in inches) .....	112
Figure A.10: Machine drawing of 180 kHz nozzle holder (Units in inches).....	113
Figure A.11: Nozzle holder stem (Units in inches) .....	114
Figure B.1: DMT nebulizer flow diagram. The nebulizer is used to deliver dry, PSL- laden air to the PASS-3.....	116
Figure B.2: Example data from PASS-3 calibration. Pre- and post-zero laser power readings represent $I_0$ (red circles) and the laser power reading during sampling with PSL or soot represent $I$ (black circles). The X marks represented the $I_0$ and $I$ signal at the midpoint of the filtered and non-filtered linear fit and are used in the attenuation calculation. ....	117
Figure B.3: Example calibration result. Weighted linear regression through the origin of calibration points.....	119
Figure B.4: NRC inverted flame burner and dilution system for delivering absorbing particle source to the PASS-3 for $B_{abs,\lambda}$ calibration. ....	121
Figure D.1: CO yield of Heavy 4 flare gas at 109.45 SLPM at dry conditions and versus liquid loading of 19 $\mu\text{m}$ of DW and 5% aqueous NaCl. Instrument bias errors are included on each individual data point. Open circles represent the average of the repeated trials at each liquid loading set point. Error bars on the closed circles are instrument bias and error bars on the open circles are the calculated total uncertainty of the average excluding any outliers. ....	124
Figure D.2: NO <sub>x</sub> yield of Heavy 4 flare gas at 109.45 SLPM at dry conditions and versus liquid loading of 19 $\mu\text{m}$ of DW and 5% aqueous NaCl. Instrument bias errors are included on each individual data point. Open circles represent the average of the repeated trials at each liquid loading set point. Error bars on the closed circles are instrument bias and error bars on the open circles are the calculated total uncertainty of the average excluding any outliers. ....	125

- Figure D.3: NO<sub>x</sub> yield of Heavy 4 flare gas at 109.45 SLPM versus liquid loading of 19 μm 15% aqueous NaCl. Instrument bias errors are included on each individual data point. Grey diamonds represent the average of the repeated trials at each liquid loading set point. Error bars on the diamonds are the calculated total uncertainty of the average excluding any outliers. .... 125
- Figure D.4: (a) absorption and (b) scattering coefficients at 405 nm of Heavy 4 flare gas at 109.45 SLPM at dry conditions and versus liquid loading of 19 μm of DW and 5% aqueous NaCl. Instrument bias errors are included on each individual data point. Open circles represent the average of the repeated trials at each liquid loading set point. Error bars on the closed circles are instrument bias and error bars on the open circles are the calculated total uncertainty of the average excluding any outliers. .... 126
- Figure D.5: (a) absorption and (b) scattering coefficients at 405 nm of Heavy 4 flare gas at 109.45 SLPM versus liquid loading of 19 μm 15% aqueous NaCl. Instrument bias errors are included on each individual data point. Grey diamonds represent the average of the repeated trials at each liquid loading set point. Error bars on the diamonds are the calculated total uncertainty of the average excluding any outliers..... 127
- Figure D.6: (a) absorption and (b) scattering coefficients at 532 nm of Heavy 4 flare gas at 109.45 SLPM at dry conditions and versus liquid loading of 19 μm of DW and 5% aqueous NaCl. Instrument bias errors are included on each individual data point. Open circles represent the average of the repeated trials at each liquid loading set point. Error bars on the closed circles are instrument bias and error bars on the open circles are the calculated total uncertainty of the average excluding any outliers. .... 128
- Figure D.7: (a) absorption and (b) scattering coefficients at 532 nm of Heavy 4 flare gas at 109.45 SLPM versus liquid loading of 19 μm 15% aqueous NaCl. Instrument bias errors are included on each individual data point. Grey diamonds represent the average of the repeated trials at each liquid loading set point. Error bars on the diamonds are the calculated total uncertainty of the average excluding any outliers..... 129
- Figure D.8: (a) absorption and (b) scattering coefficients at 870 nm of Heavy 4 flare gas at 109.45 SLPM at dry conditions and versus liquid loading of 19 μm of DW and 5% aqueous NaCl. Instrument bias errors are included on each individual data point. Open circles represent the average of the repeated trials at each liquid loading set point. Error bars on the closed circles are instrument bias and error bars on the open circles are the calculated total uncertainty of the average excluding any outliers. .... 130
- Figure D.9: (a) absorption and (b) scattering coefficients at 870 nm of Heavy 4 flare gas at 109.45 SLPM versus liquid loading of 19 μm 15% aqueous NaCl. Instrument bias errors are included on each individual data point. Grey diamonds represent the average of the repeated trials at each liquid loading set point. Error bars on

the diamonds are the calculated total uncertainty of the average excluding any outliers.....	131
Figure E.1: Measured scattering to absorption coefficient ratios at 532 nm for 19 $\mu\text{m}$ aerosols of DW, TW, 3.17% HCl and 9.51% HCl. Error bars represent total uncertainties, which were directly calculated for the dry flame and the flame with 19 $\mu\text{m}$ aerosols of DW at 10% loading. Plotted uncertainties for other cases were estimated based on the measured precision of a similar case. ....	132
Figure E.2: Measured scattering to absorption coefficient ratios at 532 nm for 13 and 19 $\mu\text{m}$ aerosols of 5% and 15% NaCl solutions. Error bars represent total uncertainties, which were directly calculated for the dry flame and the flames with 19 $\mu\text{m}$ aerosols of 5% NaCl at 7.5% loading and 19 $\mu\text{m}$ aerosols of 15% NaCl at all loadings. Plotted uncertainties for other cases were estimated based on the measured precision of a similar case. ....	132
Figure E.3: Measured scattering to absorption coefficient ratios at 870 nm for 19 $\mu\text{m}$ aerosols of DW, TW, 3.17% HCl and 9.51% HCl. Error bars represent total uncertainties, which were directly calculated for the dry flame and the flame with 19 $\mu\text{m}$ aerosols of DW at 10% loading. Plotted uncertainties for other cases were estimated based on the measured precision of a similar case. ....	133
Figure E.4: Measured scattering to absorption coefficient ratios at 870 nm for 13 and 19 $\mu\text{m}$ aerosols of 5% and 15% NaCl solutions. Error bars represent total uncertainties, which were directly calculated for the dry flame and the flames with 19 $\mu\text{m}$ aerosols of 5% NaCl at 7.5% loading and 19 $\mu\text{m}$ aerosols of 15% NaCl at all loadings. Plotted uncertainties for other cases were estimated based on the measured precision of a similar case. ....	133
Figure E.5: Comparison of soot yields derived from PASS-3 measurements at 532 nm and LII measurements. Results are shown for the dry flame and for flames injected with 19 $\mu\text{m}$ aerosols of DW, TW, and 3.17% and 9.51% HCl solutions. An effective $E(m)_\lambda$ value was estimated by scaling the soot yields derived from the PASS-3 measurements to match those derived from the LII measurements. Error bars represent total uncertainties, which were directly calculated for the dry flame and the flame with 19 $\mu\text{m}$ aerosols of DW at 10% loading and dry flames. Plotted uncertainties for other cases were estimated based on the measured precision of a similar case.....	134
Figure E.6: Perceived soot yields from the LII measurements versus the PASS-3 measurements at 532 nm from flames with injected 13 and 19 $\mu\text{m}$ aerosols of 5% and 15% NaCl solutions. Error bars represent total uncertainties, which were directly calculated for the 19 $\mu\text{m}$ aerosols of 5% NaCl at 7.5% loading and 19 $\mu\text{m}$ aerosols of 15% NaCl at all loadings. Plotted uncertainties for other cases were estimated based on the measured precision of a similar case. ....	134
Figure E.7: Comparison of soot yields derived from PASS-3 measurements at 870 nm and LII measurements. Results are shown for the dry flame and for flames	

injected with 19  $\mu\text{m}$  aerosols of DW, TW, and 3.17% and 9.51% HCl solutions. An effective  $E(m)_\lambda$  value was estimated by scaling the soot yields derived from the PASS-3 measurements to match those derived from the LII measurements. Error bars represent total uncertainties, which were directly calculated for the dry flame and the flame with 19  $\mu\text{m}$  aerosols of DW at 10% loading and dry flames. Plotted uncertainties for other cases were estimated based on the measured precision of a similar case..... 135

Figure E.8: Perceived soot yields from the LII measurements versus the PASS-3 measurements at 870 nm from flames with injected 13 and 19  $\mu\text{m}$  aerosols of 5% and 15% NaCl solutions. Error bars represent total uncertainties, which were directly calculated for the 19  $\mu\text{m}$  aerosols of 5% NaCl at 7.5% loading and 19  $\mu\text{m}$  aerosols of 15% NaCl at all loadings. Plotted uncertainties for other cases were estimated based on the measured precision of a similar case. .... 135

# Nomenclature

<b>Acronym</b>	<b>Description</b>	<b>First Use: Page</b>
AER	Alberta Energy Regulator	19
ANSI	American National Standards Institute	60
API	American Petroleum Institute	31
ASME	American Society of Mechanical Engineers	60
BCOGC	British Columbia Oil & Gas Commission	23
CE	Combustion efficiency	34
CMB	Coal bed methane	33
CRD	Cavity ring-down	54
DAQ	Data acquisition	42
DRE	Destruction removal efficiency	34
DW	Distilled water	62
ECON	Saskatchewan Ministry of the Economy	31
FB	Flowback	19
FG	Flare gas	63
FW	Formation water	25
HF	Hydraulic fracturing	18
IQR	Interquartile range	28
LII	laser induced incandescence	55
M/N	Model number	44
MFC	Mass flow controller	44
NIOSH	National Institute for Occupational Safety and Health	58
PASS-3	Photo-acoustic soot spectrometer 3 wavelength	55
PCB	Polychlorinated Biphenyls	24
PM	Particulate Matter	55
PSL	Polystyrene Latex	57
PTAC	Petroleum Technology Alliance of of Canada	29
PTFE	Polytetrafluoroethylene	56
PW	Produced water	19
RDG	Rayleigh-Debye-Gans	58
SLPM	Standard litres per minute	42
SW	Slick water	20
TDS	Total dissolved solids	24
TEM	Transmission Electron Microscopy	36
TW	Tap water	62
USGS	United States Geological Survey	20
UWI	Unique well identifier	29

<b>Symbol</b>	<b>Description</b>	<b>Unit</b>	<b>First Use: Equation</b>	<b>First Use: Page</b>
$\alpha$	Significance level	-	-	67
$B_{abs,\lambda}$	Absorption coefficient	1/Mm	(2.1)	56
$B_{ext,\lambda}$	Extinction coefficient	1/Mm	(2.1)	56
$B_{scat,\lambda}$	Scattering coefficient	1/Mm	(2.1)	56
$d_p$	Particle mobility diameter	m	-	58
$E(m)_\lambda$	Soot refractive index	-	(2.4)	58
$f_v$	Soot volume fraction	-	(2.4)	58
$G$	Grubb statistic	-	(3.1)	66
$G_{crit}$	Critical Grubb value	-	(3.2)	67
$I$	Transmitted laser power with particle-laden sample in PASS-3	mW	(2.2)	57
$I_0$	Transmitted laser power with particle-free sample in PASS-3	mW	(2.2)	57
$L$	Laser path length	m		57
$\lambda$	Wavelength	nm	(2.4)	58
$\mu$	Mean	-	(3.1)	67
$P$	Precision	-	(3.3)	68
$\sigma$	Standard deviation	-	(3.1)	58
$t$	Two-tailed student t-value	-	(3.2)	68
$n$	Number of samples	-	(3.2)	67
$X_{outlier}$	Value of suspected outlier	-	(3.1)	67

# Chapter 1

## Introduction

Hydraulic fracturing (HF) is a method commonly used in oil and gas extraction. High pressure liquids are injected into the oil or gas reservoir via perforations in the well-bore, and fissures in the impermeable formation are formed. Well-bores for HF can be strictly vertical, directional (i.e. angled), or horizontal (combination of a vertical section and a horizontal section forming an 'L' shape to cover more of the resource area). Vertical depths can vary from 0.2 to 23 km, with horizontal sections from 0.5 to 4 km (Blondes et al., 2016; Arthur et al., 2008; Gandossi, 2013; Tyner and Johnson, 2014). The upper portion of the well-bore (considered the portion that extends to below local freshwater aquifers) is generally lined with several concentric layers of steel pipe and cement, collectively known as the casing. Controlled explosive packs are either placed at specific depths in a vertical well, or along the horizontal portion of a horizontal well creating perforations in the surrounding well-casing. Large volumes (9,000 to 80,000 m<sup>3</sup>) of HF fluids are then injected at high pressure (35,000 to 70,000 kPa) into the well and out through the casing perforations created by the explosive packs to fracture the surrounding impermeable formations and induce artificial porosity (Xu et al., 2015; Lampe and Stolz, 2015; Gallegos and Varela, 2015a; Elsner and Hoelzer, 2016).

Solid particles, known as proppant and typically comprised of sand, or other ceramic particles (URS Corporation, 2011), are mixed into the fracturing liquid and act to hold these fractures open allowing the oil and/or gas to flow. Prior to initiating production

however, the injected liquids must be cleared from the well in a process known as flowback (FB), which is a central part of a “well-completion” (i.e. the preparation of a well for production). FB fluids returning to the surface are typically high in dissolved solids and salts, primarily due to mixing with the fluids in the formations. Fluids returned to the surface prior to production are known simply as FB fluids, while any fluids produced concurrently with the oil and gas are known as produced water (PW).

Common practice in the oil and gas industry is to separate the fluid returned to the surface into its respective phases and flare the collected gases. Although there are no known publicly available data on the presence or composition of entrained aerosols that may pass through the separator and flow with the gas directed to a flare, there is anecdotal evidence that this may be common. The Alberta Energy Regulator (AER) has recently initiated a small study to collect gas and aerosol samples directed toward a flare during flowback. Although the challenges of collecting samples in the field during a well-completion are significant and this study is currently underway, early indications are that aerosols are present in the flare stream although their concentrations and compositions remain unknown.

The prime motivation for this work is to investigate the potential effects of selected entrained non-hydrocarbon liquid aerosols on flare behavior and emissions. As flaring at oil and gas sites increases in North America along with increased production of unconventional oil and gas resources (U.S. EIA, 2016a; U.S. EIA, 2016b; U.S. EIA, 2016c; AER, 2016a), it appears prudent to investigate any alterations to flare emissions that such aerosols could cause.

## 1.1 Hydraulic Fracturing Fluids

Though a large variety of base fluids are used in HF, the majority of the industry employs water-based fracturing procedures (Gandossi, 2013; Gallegos and Varela, 2015b). Water-based fluids include slick water (water with small quantities of chemical additives and proppant), liquid nitrogen and carbon dioxide foam (water, surfactant, and liquefied gas), and gelled/cross-linked fluids (water with added polymers, typically guar-based) (Gandossi, 2013; Gallegos and Varela, 2015b; Harper, 2008; U.S. EPA, 2004).

Trends in HF fluids used in wells in the U.S. are plotted in Figure 1.1 using data from Gallegos and Varela (2015a)<sup>1</sup>. Slick water (SW) fracturing is of interest as it has seen rapid growth in popularity in the U.S. since 2005 as a specialized HF method for shale gas extraction. By 2010, SW fracturing had accounted for 27% of HF that were included in the United States Geological Survey (USGS) database. Undefined “water-based” fracturing accounted for 40%, and undisclosed fracturing methods for 15% (Gallegos and Varela, 2015b).

---

<sup>1</sup> U.S. Geological Survey (USGS) HF fluid database is derived from a proprietary database by IHS that is available with daily and monthly updates to subscribers. USGS omitted certain identifiers (e.g. unique well identifier, UWIs) from its publicized version to ensure trade secrets and other proprietary information were not released. Additionally, parts of the data were aggregated spatially and temporally, as was required by IHS prior to giving its permission to distribute the data in a public forum (Gallegos and Varela, 2015b; IHS, n.d.).

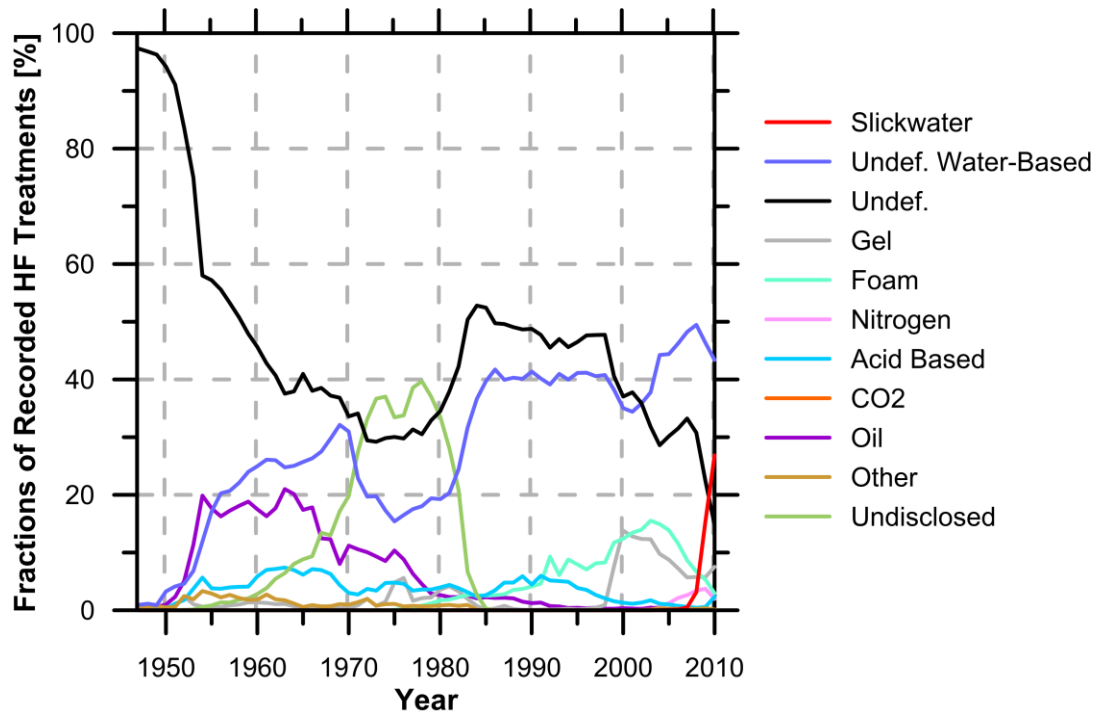


**Figure 1.1: Trends in HF fluids derived from the USGS database for HF fluids in the U.S. (Gallegos and Varela, 2015a). Data for 1,763,800 fracturing treatments from 1947 to 2010 compiled from states reporting hydraulic fracturing treatments; those with over 1000 treatments include TX, OK, PA, OH, NM, CO, WV, KS, WY, KY, LA, CA, IL, MI, UT, NY, AR, MT, AL, VA, IN, ND, NE, MS, TN, AK.**

Table 1.1 summarizes the categories and general uses of chemicals found in SW HF fluids. The process of HF often consists of several stages of fluid injection pre- and post-fracture, where each separate stage can involve different fluid compositions (URS Corporation, 2011). Exact compositions and volume of fluids required for each well vary depending on depth and size, formation geology, and water retention characteristics of the formation. Also listed in Table 1.1 are common chemicals used for each type of HF fluid and their intended purpose. This is not an exhaustive list of all materials used; FracFocus and recent literature has shown that there are numerous other chemicals used in HF fluids (URS Corporation, 2011; FracFocus, 2012).

**Table 1.1: Water-Based Hydraulic Fracturing Fluids: Purpose and Examples of Commonly Used Additives**

<b>Fluid Type</b>	<b>Chemical Examples</b>	<b>Purpose</b>
<b>Acids</b>	Hydrochloric Acid (3-28% concentration by mass) <sup>a</sup>	Remove mineral build-up in well-bore <sup>c</sup> Precursor to HF fluid injection to initiate cracks in rock <sup>b,d,e</sup>
<b>Base Fluid</b>	Water <sup>e</sup>	Constitutes the majority (85-99% by mass) of SW fluids <sup>e,f</sup>
<b>Biocides</b>	2,2-Dibromo-3-nitrilopropionamide <sup>a,g,h</sup>	Inhibit bacteria growth when organic fracturing fluids are used <sup>a</sup>
<b>Breakers</b>	Peroxydisulfates <sup>a,e</sup>	Break polymer chains for fluid recovery <sup>g,h</sup>
<b>Corrosion Inhibitors</b>	Glutaraldehyde <sup>b</sup> Acetone <sup>h</sup> Isopropanol <sup>d</sup>	Prevent corrosion in well-bore pipe <sup>b,d,h</sup>
<b>Friction Reducers</b>	Polyacrylamide <sup>i,b</sup>	Reduce wall friction <sup>b</sup>
<b>Scale Inhibitor</b>	Ethylene glycol <sup>ij</sup>	Remove scale build up in pumping equipment and well-bore pipe <sup>i</sup>
<b>Surfactants</b>	Ethanol <sup>d</sup> Isopropyl alcohol <sup>dj</sup>	Used in SW <sup>e</sup> Reduce HF fluid surface tension <sup>d</sup>

a URS Corporation (2011)

b Gregory (2010)

c Steliga et al. (2015)

d Vidic et al. (2013)

e Gallegos and Varela (2015a)

f FracFocus (2012)

g U.S. House of Representatives (2011)

h US EPA (2004)

i Lampe and Stolz (2015)

j Arthur et al. (2008)

Though general details on types of chemicals and their purpose in HF fluids are well-known, detailed chemical composition data for SW and other fracturing fluids used in the U.S. and Canada were, until recently, unavailable to the public. Responding to public and governmental pressures to disclose fracking fluid chemistry due to concerns over groundwater contamination, certain U.S. states, Canadian provinces, and oil and gas

corporations<sup>2</sup> began submitting general compositions of the injected fluid online at the public internet site ‘FracFocus’. The chemical registry was initiated in the U.S. in 2011 by the Ground Water Protection Council and Interstate Oil and Gas Compact Commission, and in Canada in 2012 by the British Columbia Oil and Gas Commission (BCOGC). AER joined later in 2012 with the publication of Directive 059 updating reporting requirements for Albertan oil and gas companies (FracFocus, 2011; FracFocus, 2012; AER, 2012).

Chemical composition data for individual wells in any province that submits to FracFocus are most often specified as concentration ranges of individual compounds and are only available as separate files for each well in PDF format. Moreover, on data files where the “carrier fluid” (i.e. base fluid) is reported as water, the type of water used (e.g. fresh or salt-water) is not specified. Downloadable PDF Hydraulic Fracturing Fluid Product Component Information Disclosures for Albertan wells available at [http://fracfocus.ca/find\\_well/download/](http://fracfocus.ca/find_well/download/) note that “total water volume sources may include fresh water, produced water, recycled water, and/or other water types”. According to Directive 059, the “other water types” could include “surface water, non-saline groundwater, saline groundwater, recycled fracturing water, non-oilfield waste water, drinking water, and other oilfield water such as produced water or waste water,” (AER, 2012). Although 29% of U.S. wells state the general type of water used, this information is of little value as specific composition details for the general water types are not provided (U.S. EPA, 2015). This lack of specificity is also noted in the literature (Hayes, 2009). In general, because water composition is not disclosed even though it can account for >90%

---

<sup>2</sup> In Canada, Albertan well operators are required to submit data to FracFocus.ca (AER, 2012; BC Oil & Gas Commission, 2015). In the U.S., a full list of participating companies is listed here: <http://fracfocus.org/links>. Each state has different reporting requirements for HF fluids.

of the total volume of HF fluids, the available FracFocus data lack the specifics to properly analyze HF fluid composition (FracFocus, 2012; FracFocus, 2011; Gallegos and Varela, 2015b; Hayes, 2009).

## **1.2 Flowback Fluids**

Notwithstanding the ambiguity in the exact composition of HF fluids, PW and FB are ultimately the fluids of interest, as these are the recovered materials that must be disposed of, treated, or reused in other HF processes (Vengosh et al., 2014; Arthur et al., 2005; FracFocus, 2012; FracFocus, 2011). Recent studies have highlighted the importance of characterizing FB and PW and have shown that the composition of these fluids is quite different than that of the injected fluids. In addition, the compositions of FB fluids vary in time as the FB event progresses over days to months. Figure 1.2 shows the changes in concentrations of: (a) total dissolved solids (TDS, a measure of salinity) and the two most prevalent species found in the FB and PW data (b) chlorine and (c) sodium ions. The data are derived from 32 hydraulic fracturing sites in North America spanning up to a 44-day period. As emphasized by the logarithmic scale of the vertical axes, there are significant changes in composition during the first ~two days of well-completion, where TDS, chlorine and sodium ions all tend to rapidly increase. It is apparent that the final composition of the FB liquid is quite different than the injected HF fluid.

Hayes (2009) conducted a study of temporal trends in FB in 19 wells for the Marcellus Shale Coalition (black and grey lines in Figure 1.2). They analyzed general chemistry, halogen ions, (semi-) volatile organic compounds, metals, pesticides, and polychlorinated biphenyls (PCBs). Red lines in Figure 1.2 show data from McElreath (2011) on two wells of undisclosed location.

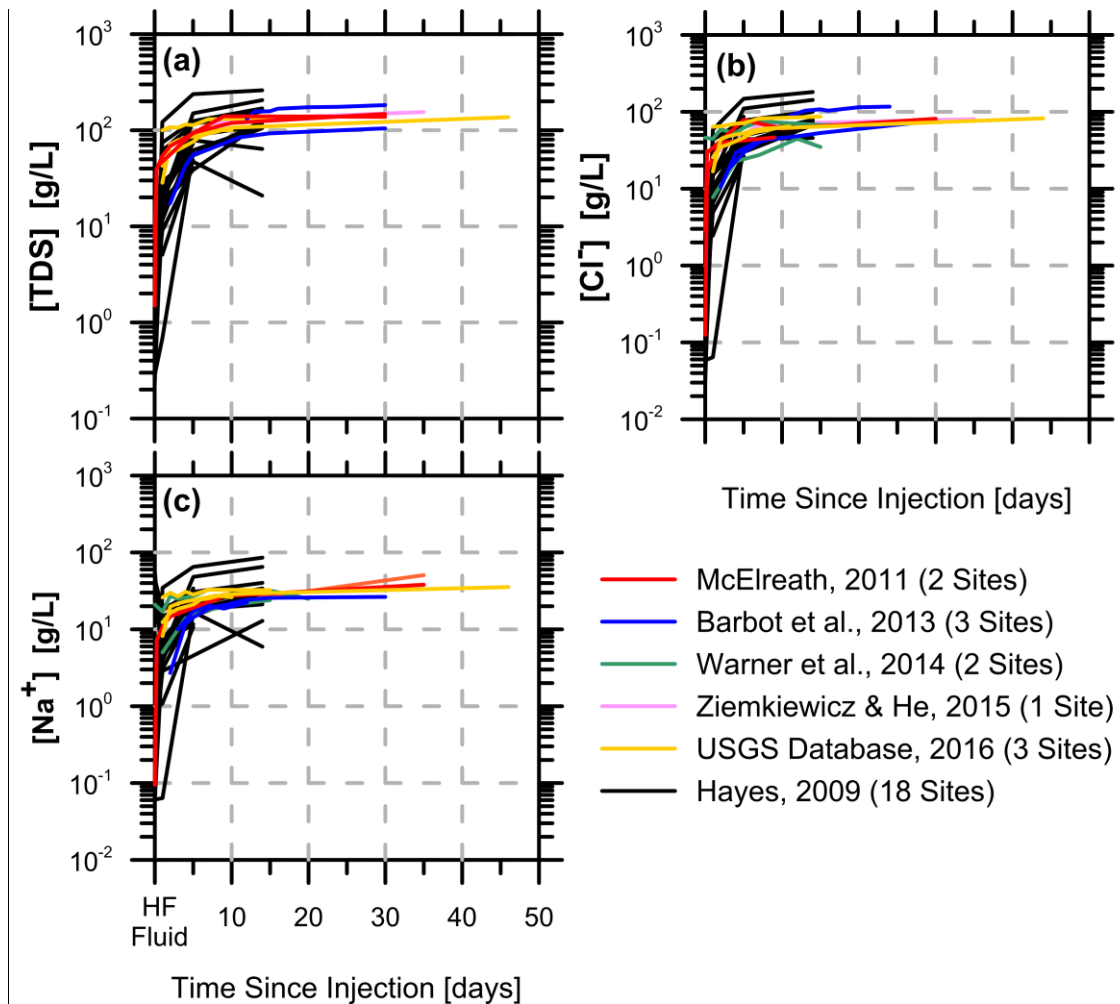


Figure 1.2: Temporally resolved FB composition of a) TDS, b) chloride, and c) sodium ions, over a span of 44 days.

Barbot et al. (2013) (blue lines in Figure 1.2) conducted a study on three wells of undisclosed locations and compared the results to seawater evaporation trends highlighting similarities and differences between pure formation water (FW) and FW mixed with HF fluids. FW is known in the literature as basinal brine, basinal water, connate fluids, or oil-field brines. During the sedimentation process that formed the resource, groundwater or sea water was trapped in pores along with the organic material that was transformed over geological time into natural gas and other fossil fuels. The salinity of the FW measured

in TDS<sup>3</sup> varies greatly from fresh (TDS<1000 mg/L) to brine (TDS> 3.5 × 10<sup>4</sup> mg/L) originating from the seawater originally trapped and from dissolution of formation salts in the water (Kharaka and Hanor, 2007).

It is recognized that the dominant factor causing the change in concentration is due to the mixing of HF fluids with FW (Ziemkiewicz and Thomas, 2015; Barbot et al., 2013; Wasylshen and Fulton, 2012; Haluszczak et al., 2013; Hayes, 2009; Capo et al., 2014). Barbot et al. (2013) and similar studies including Ziemkiewicz and Thomas (2015) and Warner et al. (2014) (pink and green lines in Figure 1.2, respectively) concluded that the changes in composition can also be partially attributed to chemical reactions, dissolution of formation geological features, and fracturing pressure and temperature. This is demonstrated by the similarity in FW behaviour with that of seawater via relationships between certain key ion concentrations (e.g. bromide, chloride, magnesium, calcium, and strontium) through the evaporation and dilution process. Subsequently, by comparing seawater evaporation to PW samples, discernable differences in behaviors in ion relative concentrations are seen.

Figure 1.3 shows concentration statistics of TDS (a measure of salinity) and the 17 most common species found in FW. Considering the logarithmic axes, it is clear that in the 599 individual samples from formations across the globe, chlorine, sodium, and calcium comprise the majority of FW. The significant variation in the data is as expected – the FW samples in the data set are from a wide range of age and formation types.

---

<sup>3</sup> TDS can be measured, calculated via conductivity, or calculated by summing the major ions. Depending on the method used, this can lead to some discrepancy in the presented data (i.e.  $TDS \neq \sum m_{ions}$ )

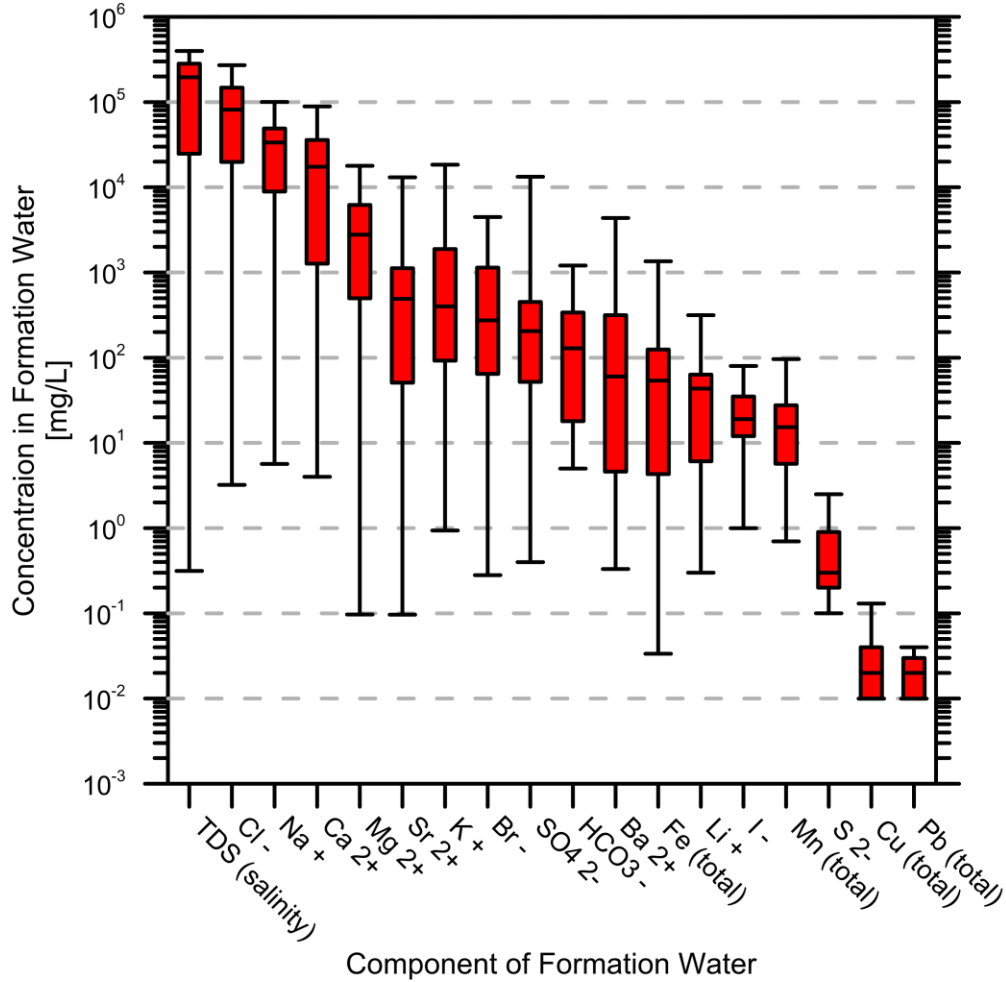


**Figure 1.3: Box and whisker plot showing median, upper, and lower quartile (red) and maximum and minimum concentrations of various species in formation water. Data are compiled from 599 samples representing 14 formation ages (Dresel and Rose, 2010; Osborn and McIntosh, 2010; Balashov et al., 2015; Hobbs et al., 2011; Worden, 1996; Martini et al., 1998; Cowie et al., 2014; Kharaka and Hanor, 2007; and Dollar et al., 1991).**

It is possible then, that the quasi-asymptotic trends seen in Figure 1.2 could represent the time for HF fluids and FW to reach a diffusion and chemical equilibrium (Ziemkiewicz and Thomas, 2015). Figure 1.4 replots a subset of the data from Figure 1.2 to show compositions from day 2 to 46 after initiation of flowback. Overlaid as red lines on Figure 1.4 are the upper quartile, lower quartile, and median data for formation water from Figure 1.3. Beyond two days after initiation of flowback, Figure 1.4 demonstrates

that the concentration of the FB generally remains within the inter-quartile range (IQR) of the FW. It should be noted, however, that the IQR for these species vary nearly a full order of magnitude emphasizing the high degree of variability in FW concentrations from well to well and formation to formation. Given this variation in FW, it follows that as FB fluids become dominated by dilution with FW, their compositions would show equivalent variations in chemistry.

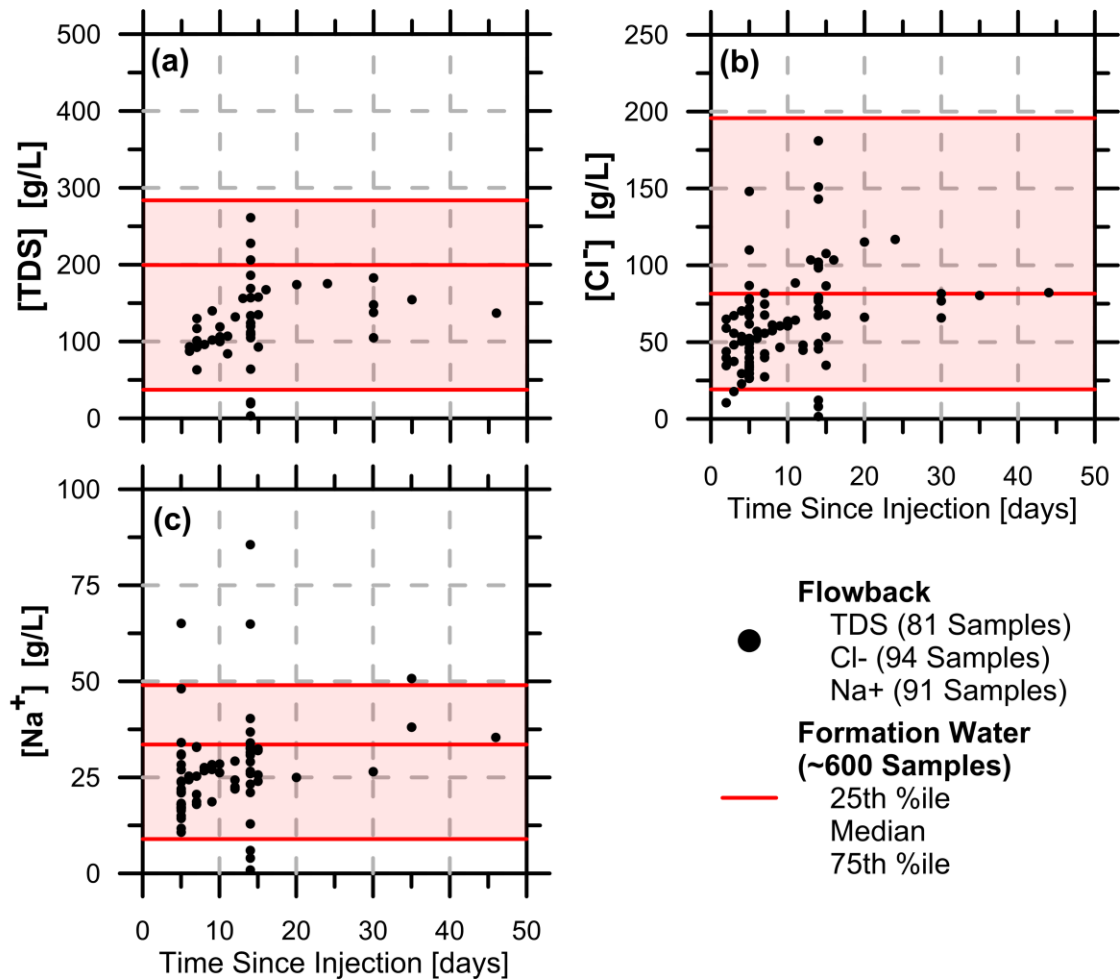


Figure 1.4: Plot of Figure 1.2 with overlaid quartiles of FW data compiled from 599 samples.

Much of the literature on FB or PW is lacking one or more critical pieces of information such as temporally resolved data, HF fluid composition, exact location, or FW samples from the same well. Most commonly however, is the omission of time-resolved

data. This is clearly vital; based on Figure 1.2, characterization of flowback composition as a single value or range would not be capturing the true nature of FB composition, particularly if the sample was taken within the rapidly-changing time-frame immediately after fracturing. The USGS Produced Water Database (updated as recently as 2016) is a large compilation of FB and PW information. Of the over 11,000 entries (as of September 2016) on shale and tight oil and gas wells, only 14 wells had “time series” data, and only three of those has sufficient composition data to be included on Figure 1.2 (yellow lines). A report prepared for the Petroleum Technology Alliance of includes only single number concentrations for PW, but does provide HF fluid concentrations (Wasylishen and Fulton, 2012). Michel et al. (2015) shows only single number concentrations for FB and indicates that the value is (presumably time-) averaged. Similarly, a study on organic compounds found in PW by Maguire-Boyle and Barron (2014) examined PW (i.e., gas was being produced at the time of sampling) from three formations (Marcellus, Barnett, and Eagle Ford), though no data on the length of time, since neither well-completion nor time-series were included in the paper.

Of the 32 data sources considered for obtaining FB and FW data, only nine considered temporal effects on FB salinity and general composition. Another key component to consider is the location of a well. Samples were rarely seen with a Unique Well Identifier (UWI) or GPS coordinates, which generally precludes connecting FW data with FB and PW samples.

Adding to the ambiguity, the term PW is often used interchangeably with FB and FW in the literature. For example, Alley et al. (2011) (a paper aggregating several studies on “produced water”) defines produced waters as fluids “generated during processes such

as fossil fuel extraction, fossil fuel energy production, and industrial operations,” indicating potential for all three uses of the word as defined in this thesis. However, sources for their shale gas “produced water” comes from, 1) the USGS Produced Water Database (Blondes et al., 2016) where it is clear that parts of the samples are FB (and in some cases even time-resolved); and 2) two sources that use “produced water” in the sense of FW (McIntosh and Walter, 2005; McIntosh et al., 2002).

### **1.2.1 U.S. and Canadian Regulations for the Disposal of FB and PW Liquids and Gases**

U.S. regulations for disposal and treatment of PW and FB are mandated by individual states and can be managed by the following methods: enhanced oil recovery, disposal well injection (as Class II injection wells), on- and off-site disposal (at private or municipal treatment facilities), surface discharge, evaporation ponds, or reuse in fracturing procedures (Wasylishen and Fulton, 2012; Haghshenas and Nasr-El-Din, 2014; Clark and Veil, 2015).

However, management of PW and FB fluids between the time the liquid returns to the surface and prior to the aforementioned disposal methods, is federally regulated. FB and PW must be directed to a separator where the gas phase and any entrained liquids are removed (CFR, 2016). The regulation states that gases must be, in order of priority, directed to an existing gas line “as soon as practical” if salable, or if not, directed to a flare with a continuous pilot light. The effectiveness or minimum droplet size that the separator

must remove is not stated in this regulation; however, American Petroleum Institute (API) Standard 521 states droplets 300-600 µm in diameter must be removed<sup>4</sup>.

In Canada, the oil and gas industry is regulated provincially. Alberta is the largest producer of oil and gas resources in Canada (representing 67% of Canada's natural gas total production and 42% of light crude oil production, and 85% of heavy oil production (NEB, 2017a; NEB, 2017b)) and other jurisdictions (e.g. SK, the second largest oil producer, or BC the second largest gas producer) tend to base their regulations on those of Alberta (AER, 2016b; BC Oil & Gas Commission, 2016; Government of Saskatchewan, 2015a). Flowback flares are designated as temporary flares by the AER, BCOGC and the Saskatchewan Ministry of the Economy (ECON). Directive 060 and BCOGC's Flaring and Venting Reduction Guideline requires producers to apply for a temporary flaring permit, the application for which must include an evaluation of flaring reduction opportunities such as tying in the gas lines prior to the well-completion. The evaluation criteria are not explicitly stated however. The AER, BCOGC, and SK ECON place time limits on temporary flaring, but extensions can be applied for if the flowback procedure is not fully completed, which in practice makes the time limit regulation irrelevant to flowback flares (AER, 2016b; BC Oil & Gas Commission, 2016; Government of Saskatchewan, 2015a).

Regulations state that liquids must be separated from the gases prior to the gases entering the flare line. AER Directive 060 and ECON S-20 states that droplets

---

<sup>4</sup> The intent of the legislation is to allow only droplet sizes that will evaporate fully as they pass through the flame; droplets of larger size (though less likely remain entrained through the piping network) could result in the significant safety hazard of "burning rain". The droplet size is given as a range to allow for variations in flare size and fuel flow rate (API, 2012).

“300-600 µm in diameter or larger” must be removed, referencing API Standard 521 (AER, 2016b; Government of Saskatchewan, 2015b; API, 2012). BCOCG regulations do not indicate a threshold for droplet size removal for separators (BC Oil and Gas Commission, 2010; BC Oil & Gas Commission, 2016). Treatment of the separated liquid then falls under AER Directive 058 (AER, 2006) which states “common/acceptable practices” are recycling and/or recovering hydrocarbons and/or injecting into a disposal well.

### **1.3 Flaring**

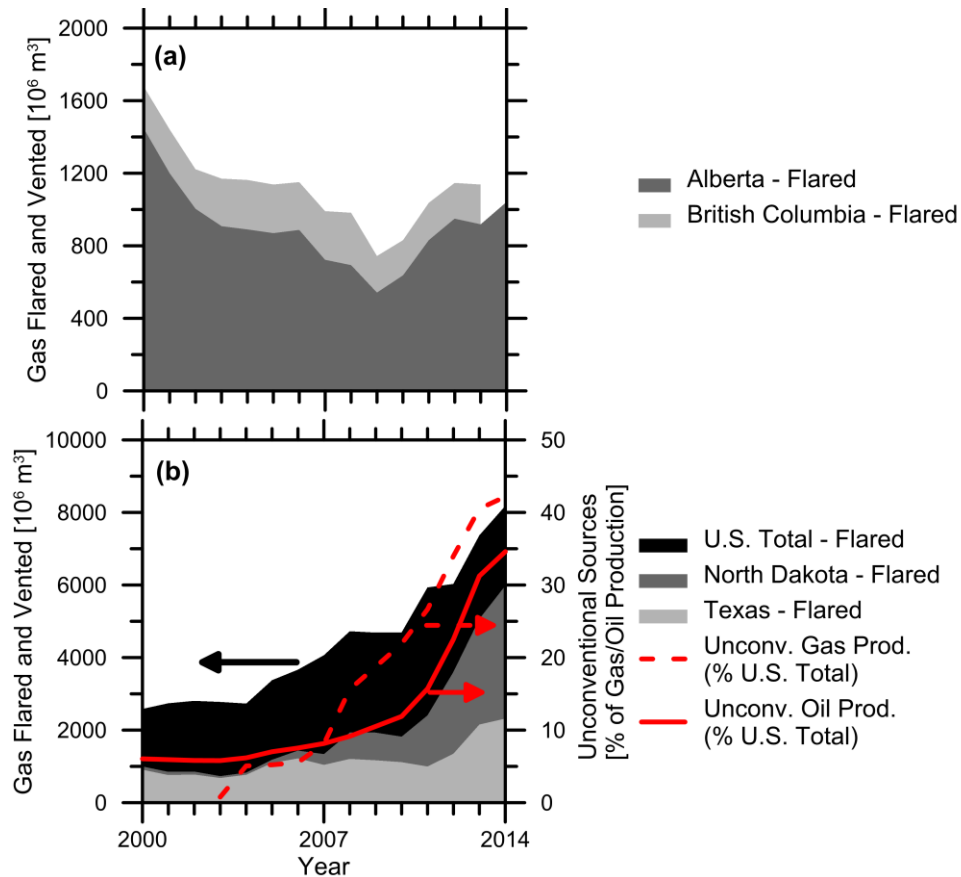
Flaring is the practice of combusting unwanted or uneconomically viable flammable gases and is common in a multitude of industries. Recent satellite data suggest that approximately 140 billion cubic meters of gas are flared globally each year, an amount equivalent to 3.5% of global natural gas production (Elvidge et al., 2016; BP, 2015). Reported flared volumes in Canada and the U.S. have increased in recent years. Figure 1.5(a) shows available reported flaring volumes in Alberta from 2000 to 2014 and BC from 2000 to 2013. Though flaring to production ratios in Alberta have remained between 3.7 and 6.9% since 2000, total flared volumes have increased with production expansion. In the AER annual flaring and venting reports from 2009-2013, the AER has attributed the province’s yearly increases in flared gas to the creation of new large-scale HF wells (Johnson and Tyner, 2015; AER, 2016a).

Figure 1.5(b) shows U.S. flared volumes have been increasing since 2000<sup>5</sup>. Total volumes of flaring amounted to 0.5% of gas production in the U.S. in 2000 and increased steadily to 2.7% in 2014. Though flaring data parsed by well type (conventional or

---

<sup>5</sup> Venting volumes are included in these figures, though ND law prohibits venting and TX law prohibits venting via total time (24 hours maximum for a single event, or 72 hours total per month).

unconventional) are unavailable to the public, parsed production data are accessible. Increases in production are most notably seen in Bakken Shale in North Dakota, the Eagle Ford and Haynesville Shales in Texas, and the Marcellus Shale in Pennsylvania, New York and Ohio. The U.S. production ratios of shale and coal bed methane (CBM) gas to total gas (dashed red line) and shale oil to total oil (solid red line) for the U.S are shown in Figure 1.5(b) (Unfortunately, similar data were not available for Canadian production). In 2014, 42% of total gas production in the U.S. was from unconventional sources (shale and CBM), and 35% of total oil production was from shale sources. In 2015 (not plotted), shale oil industry penetration continued to rise to 43% (U.S. EIA, 2016a; U.S. EIA, 2016b; U.S. EIA, 2016c).



**Figure 1.5: Flaring Volumes in a) Canada, and b) U.S. Plot b) includes the percentage of oil and gas production in the U.S. from unconventional sources of oil and gas.**

## 1.4 Potential Effects of Entrained Aerosols on Flare Emissions

Air pollutant emissions from flares may include greenhouse gases such as carbon dioxide and methane, as well as criteria air contaminants such as carbon monoxide (CO), nitrogen oxides (NO<sub>x</sub>), sulfur oxides (SO<sub>x</sub>, in the case of sour gas), and particulate matter (primarily in the form of black carbon), and potentially other volatile organic compounds (VOCs) from unburned or partially combusted fuel. These species are known to have a range of human health and environmental impacts. NO<sub>x</sub> and SO<sub>x</sub> lead to acid rain (Nevers, 1995); VOCs, NO<sub>x</sub>, and particulate promote the production of smog and ground-level ozone (Nevers, 1995); and black carbon (BC) is linked to respiratory illnesses and fatality (Grahame et al., 2014).

Emissions from flares burning gaseous fuel mixtures have been the subject of several recent laboratory and field measurement studies (Conrad and Johnson, 2017; Corbin and Johnson, 2014; McEwen and Johnson, 2012). However, to the author's knowledge there have been no published studies specifically considering effects of entrained non-hydrocarbon aerosols (as could occur during flowback) on flare performance. Recent work by Torres et al.(2012) investigated effects of steam injection on flare emissions, where steam-assisted flares are commonly used in industry to suppress visible soot emissions. Their results revealed that steam injection could cause dramatic decreases in flare efficiency when steam:gas ratios exceeded 50% (by mass) (Torres et al., 2012). Both destruction removal efficiency (DRE, % hydrocarbon in fuel converted) and combustion efficiency (CE, % of carbon from fuel converted to CO<sub>2</sub>) were shown to decrease, suggesting that added steam leads to emissions of unburned fuel.

Available literature on combustion systems with droplets of non-liquid aerosols is primarily focused on furthering the fire safety industry by determining optimal criteria for flame extinguishment using water. Lab-scale studies primarily used well-defined combustion setups, such as: co-flow burners (Prasad et al., 1998; Morgan and Rosocha, 2012; Sakurai et al., 2013; Kazemimanesh et al., 2012), counter-flow (Lentati and Chelliah, 1998; Lazzarini et al., 2000; Yoshida et al., 2015), and pre-mixed burners (Fuss et al., 2002; Fleming et al., 2002). Models of these two-phase, chemically reacting flows have been developed with monodisperse droplets for laminar pre-mixed flames (Modak et al., 2006; Chelliah, 2007; Yang and Kee, 2002) and counter-flow flames (Chelliah, 2007) and with polydisperse droplets for pre-mixed flames (Blouquin and Joulin, 1998). Most commonly, distilled water was aerosolized and droplet sizes ranged from sub-micron to 200 microns.

The findings in these studies are generally similar in that droplet size is a significant factor in affecting extinguishment up to a certain diameter. The critical droplet size was found to vary among studies, flame type, liquid loading, and fuel flow rates. However, the criteria remained the same: the largest effect on the flame was found to be when the droplet fully evaporated before leaving the flame front. It was subsequently concluded that at this critical diameter, the heat loss due to the vaporization of water was maximized (Yoshida et al., 2015; Yang and Kee, 2002; Chelliah, 2007). Lentati and Chelliah (1998) added to this, isolating the radical-forming area of the flame (methane, counter-flow) as the region most affected by the temperature decrease and responsible for flame strain rate decreases. There is debate in the literature as to the relative significance of the thermal versus chemical effect of water aerosols in flames. The injection of water provides the catalyst by which

the water-gas shift reaction<sup>6</sup> occurs and provides combustion reactions with additional OH radicals that contribute to the full oxidation of CO to CO<sub>2</sub> (Dethlefs and Schladert, 1976; Atreya et al., 2000; Turns, 2012). The presence of dissolved species or additives in the water can induce additional chemical effects on flame performance (Lazzarini et al., 2000).

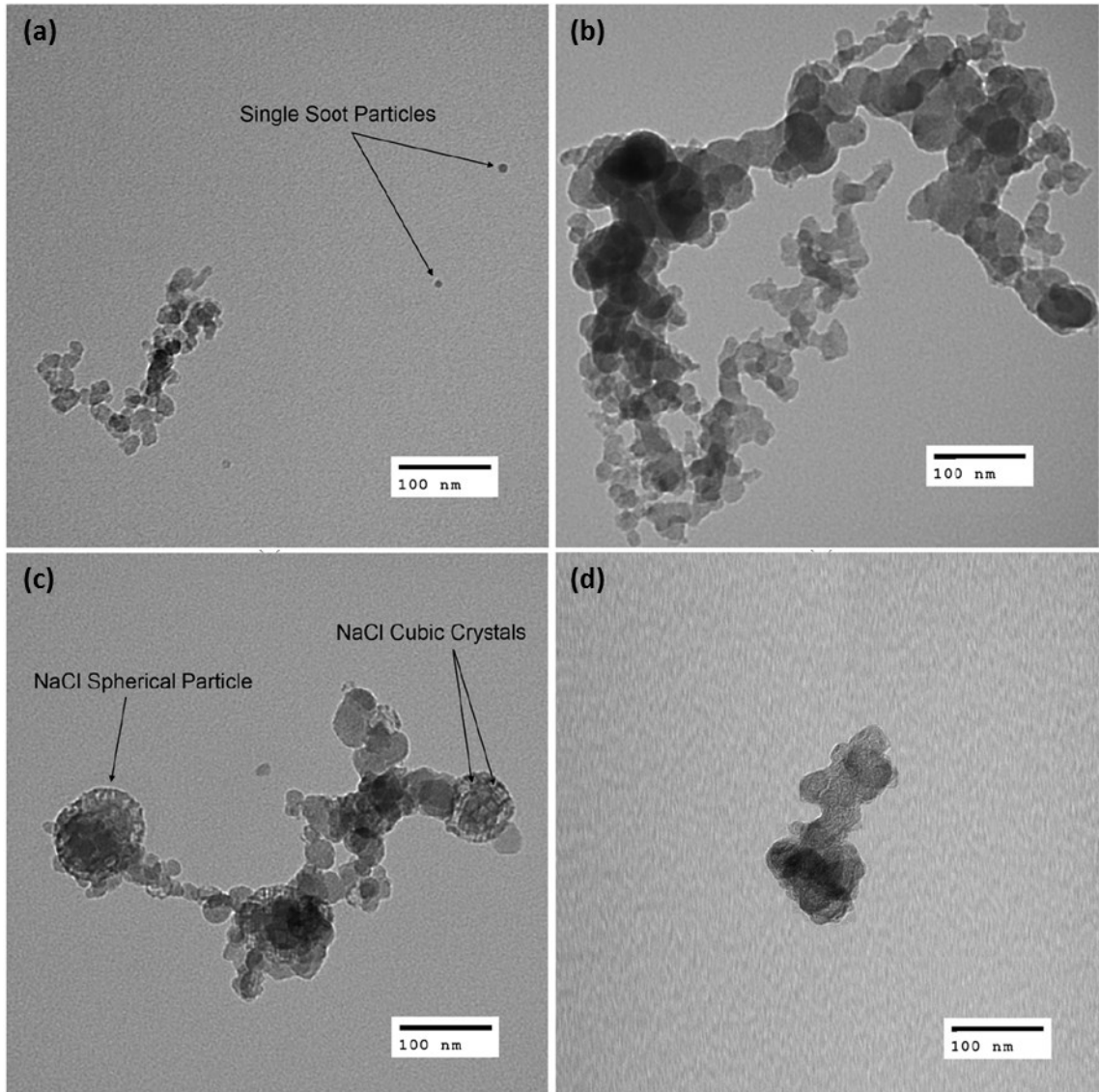
In experiments conducted at the CLSF facility with an earlier model of the custom atomizing burner discussed in Section 2.1.2, Kazemimanesh (2014) identified some effects of non-hydrocarbon liquid aerosols (water, aqueous NaCl, and aqueous HCl) on particle mobility diameters of solid-phase combustion products. Using transmission electron microscopy (TEM) imaging, solid NaCl crystals were found in the soot particles of the saltwater tests. NaCl aerosol tests also showed a 2× increase in soot number density. Kazemimanesh (2014) suspected that the particles measured were NaCl as well as nucleated NaCl particles that form the aforementioned internally and externally mixed soot particles.

Figure 1.6 shows TEM images from Kazemimanesh (2014). Considering a droplet of aqueous NaCl, as the water evaporates due to the increased temperatures near or in the flame, the dissociated Na<sup>+</sup> and Cl<sup>-</sup> can reach concentrations such that recrystallizations begins. Alternatively, it is also possible that, depending on the temperature of the flame, the NaCl<sub>(s)</sub> residue could dissociate into its respective plasmas (Na<sub>(g)</sub> and Cl<sub>(g)</sub>) (Morgan and Rosocha, 2012; Whitten et al., 1982). Morgan and Rosocha (2012) presented a reduced mechanism of Na and Cl plasma chemistry involving Na<sup>+</sup>, Cl<sup>-</sup>, Cl<sub>2</sub>, Na<sub>2</sub>, and excited states of each. While sodium could have a significant effect on solid-phase combustion products,

---

<sup>6</sup> Water-gas shift reaction is:  $\text{CO} + \text{H}_2\text{O} \leftrightarrow \text{CO}_2 + \text{H}_2$

the addition of the highly reactive ionized chlorine could affect the gas-phase combustion products.



**Figure 1.6: Transmission electron microscope (TEM) images of particulate matter from work in Kazemimanesh (2014) from : (a) dry flames; (b) DW (74 mL/min); (c) 10% NaCl (74 mL/min) and; 1% HCl (74 mL/min)**

The effect of chlorine and chlorine compounds in flames is generally characterized by the competition for key combustion radicals between carbon monoxide and chlorine. Gokulakrishnan and Lawrence (1998) examined CO emissions from a fluidized bed reactor

of pyridine fluidized with an addition of  $\text{HCl}_{(g)}$ . The authors found significant increases in CO emissions with a higher concentration of HCl introduced to the system; at what was noted to be a reasonable C:Cl ratio for coal combustion (100 ppm HCl), CO concentrations doubled compared to that of an identical non-chlorinated system. At the highest concentration of HCl tested (6000 ppm) CO concentrations were 20× higher than the base case. It was also found that temperature of the fluidized bed played a notable role in CO emissions. Experiments were conducted at 750 and 900°C and showed more significant increases in CO emissions at the lower temperatures. Interestingly, 900°C tests over a wide range of HCl concentrations total carbon content from CO and  $\text{CO}_2$  remained constant, whereas tests at 750°C generally showed a decrease in total gaseous carbon content with increased concentrations of HCl. It is hypothesized that, with the lack of other hydrocarbon readings via FTIR, the “missing” carbon was converted to soot.

With the introduction of chlorine into the combustion system, it has been long identified that key combustion radicals are “scavenged” by HCl and other reactive chlorine species. In particular, OH radicals may be consumed by Cl in the following reaction:



This can then compete with the main reaction by which CO is oxidized to form  $\text{CO}_2$ :



At temperatures that could occur in a flame or combustion scenario, the rate of reaction of Reaction (1.1) is significantly faster than that of Reaction (1.2) ( $k_{1.1}/k_{1.2}$  decreases with temperature from 7.8 at 500 K to 2.3 at 3000 K) (Miller and Bowman, 1989; Chang et al., 1987).

Literature regarding the inhibition pathways of HCl on entrained flow reactors (Wei et al., 2009; Wu et al., 2016), counter-flow non-premixed (Zhou et al., 2015; Hua Yang et al., 1994), and fluidized bed reactors (Wang and Anthony, 2009; Gokulakrishnan and Lawrence, 1998) reveals similar effects. For systems not directly introducing HCl, the acid can be formed via reactions (1.3) and (1.4).



Gokulakrishnan and Lawrence (1998) and Chang et al. (1987) note that because HCl can be readily formed from chlorine gas and chlorine radicals, a cyclic production/destruction is possible. This then suggests the efficacy of chlorine's scavenging is underestimated by a simple ratio of rates of reactions, since without a comprehensive understanding of all the scavenging and reforming reactions that may be at play, it is difficult to quantify the true inhibiting effect of chlorinated species in combustion environment.

Gokulakrishnan and Lawrence (1998) investigated NO<sub>x</sub> formation and showed that chlorine addition to the combustion environment inhibited the formation of nitrogen oxides. NO<sub>x</sub> is formed in high temperature environments via combustion radicals (O and OH) and hydrogen cyanide (HCN) (Turns, 2012; Gokulakrishnan and Lawrence, 1998). NO<sub>x</sub> formation was subjected to the same radical scavenging as CO<sub>2</sub>, and showed a marked decrease in formation, though to a much lesser absolute extent than the effect on CO. At 6000 ppm (the highest concentration tested) NO<sub>x</sub> decreased by a maximum of 75% vs. a 20× increase in CO.

The cited studies demonstrate that in well-defined flame or burner experiments, the addition of chlorine- and/or sodium-containing species can significantly alter combustion emissions. The main mechanism by which this occurs is through the consumption of critical combustion radicals by chlorinated species either introduced to the system or reformed in the consumption process, which affects both the oxidation of CO into CO<sub>2</sub> as well as NO<sub>x</sub>. Available evidence suggests that sodium and sodium chloride particles may also play a significant role in influencing the form of solid-phase combustion products.

## **1.5 Thesis Motivation and Objectives**

The motivation for this work is to investigate potential effects of non-hydrocarbon aerosols on emissions and performance of lab-scale flares. With the rise of hydraulic fracturing in North America and globally, the flaring-intensive FB event has the potential for combustion emissions distinct from those of regular flaring operations in the industry. The possibility of aerosolized FB and FW, high in dissolved sodium chloride, coupled with regulations that could allow these aerosols to reach the flare, provide the necessary components to significantly affect flame performance.

To the author's knowledge there is no research or field data examining combustion emissions of FB flares (full- or lab-scale). The rapid rise in HF and subsequent flaring volumes, coupled with the legitimate potential for FB and FW aerosols to reach the flare, justify examination of any effects on combustion emissions. However, without detailed information on the potential amounts or compositions of aerosols that may or may not survive the separation process and be entrained into a flare stream during flowback, this study is intended to be exploratory only where the goal is to inform and possibly bound the range of any observed effects that might occur.

Accordingly, the following are the objectives of this thesis:

- Design and modify current CLSF to facilitate a new atomizing burner and acquire and calibrate the necessary gas- and solid-phase combustion product analyzers;
- Conduct flare experiments with liquid aerosol injection of fluids similar in composition to FB and FW to provoke an effect on combustion product species yield;
- Investigate possible causes for any emission trends when changing droplet size, liquid flow rate, or liquid type; and
- Conclude as to whether this provocation warrants further investigation and provide insight for future experiments.

# Chapter 2

## Experimental Setup

### 2.1 Carleton University Lab Scale Flare (CLSF) Facility

Experiments were performed at the CLSF facility which permits controlled experiments on flames up to approximately three meters tall at flare gas flow rates up to approximately 600 SLPM (standard litres per minute, defined at 273.15 K, 1 atm) depending on the selected fuel composition. A National Instruments (NI) data acquisition (DAQ) system running software written in LabVIEW was used to control and monitor a multicomponent fuel delivery system, gas and particulate analyzers, a variable speed exhaust fan, and ancillary temperature sensors.

Figure 2.1 depicts the general layout of the lab and primary components necessary to conduct flare experiments. The flare burner is located in a 1.88 m deep, hexagonal pit. A large hexagonal fume hood with 3.1 m included diameter is suspended 3.4 m above the floor of the pit. To ensure the flame is not affected by the presence of the pit walls, supplementary air supply is delivered through a perforated pipe (4 in diameter) laid along the perimeter of the pit. In addition, two concentric cylindrical metal mesh settling screens (mesh size 12, 1.5 m and 3.1 m diameters) suspended from the exhaust hood and reaching to the pit floor surround the burner. These screens settle any dominant flow patterns in the large lab space and allow the flame to remain vertical. During a flare experiment, the entire

flare plume and additional entrained air are drawn into the large exhaust hood. The hood feeds into a 40.6 cm diameter duct.

Sample probes are inserted into this duct, approximately 10.6 m downstream of the hood. The probes connect to heated sample lines which feed the various emissions analysis instruments. A 3.7 kW variable speed fan (IAP Vane Axial VAX 180) drives the duct flow which exhausts to the exterior of the building.

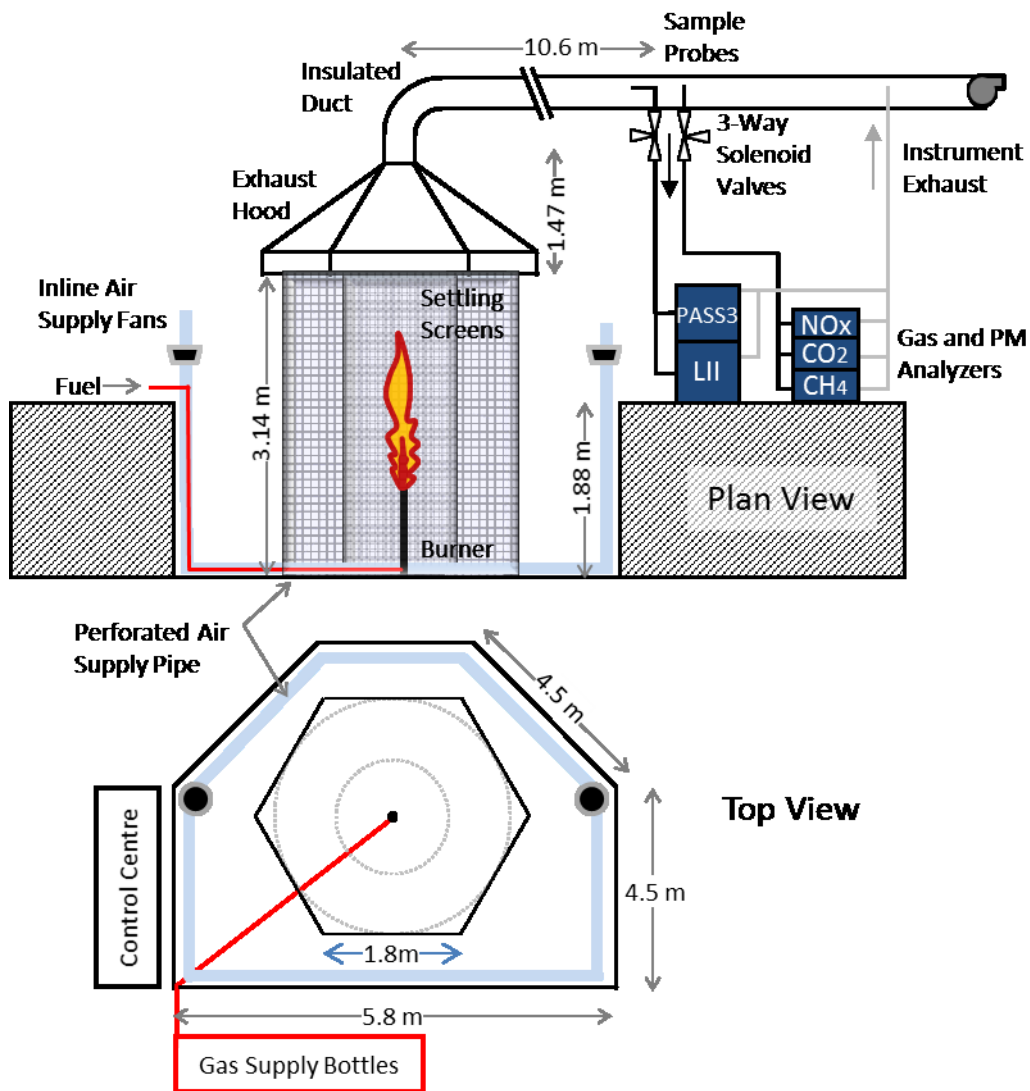
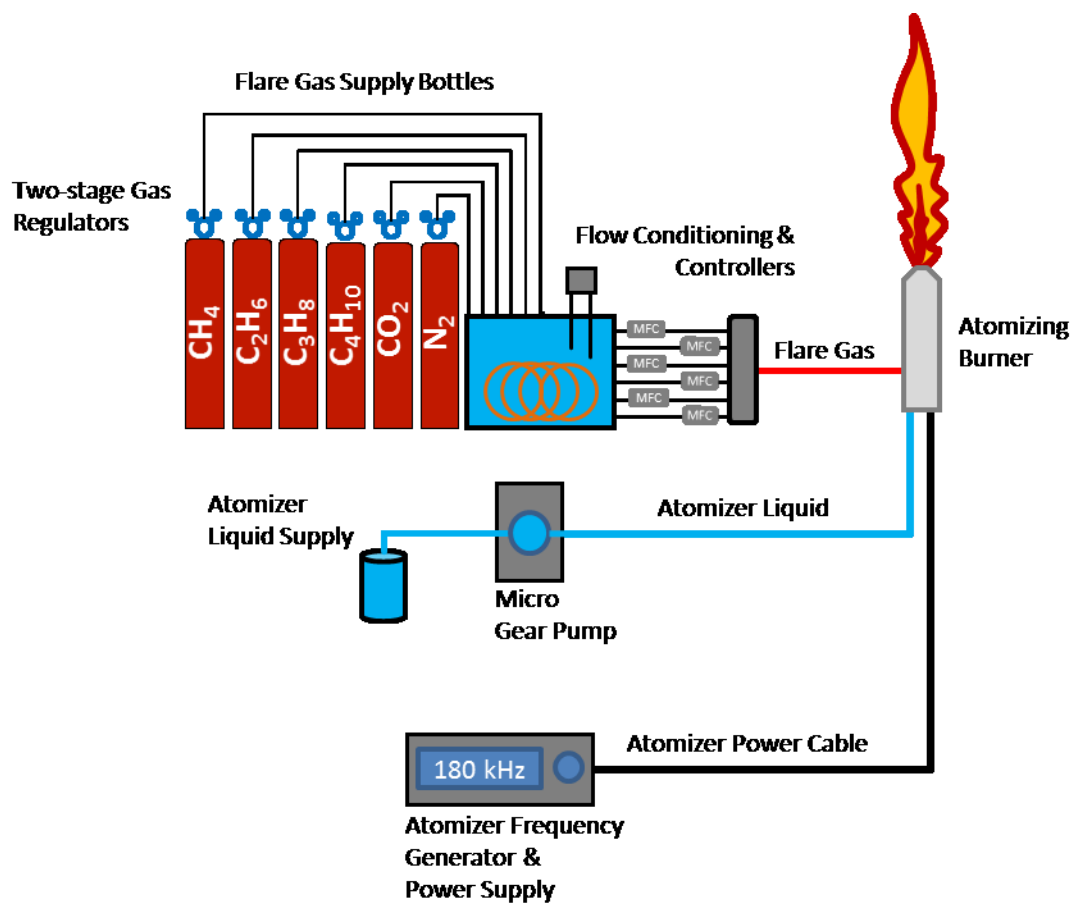


Figure 2.1: CLFS facility schematic. Adapted from Corbin (2014).

### 2.1.1 Fuel Delivery

The CLSF facility allows for flaring of custom gaseous fuel mixtures generated through a series of mass flow controllers shown schematically in Figure 2.2. Pure gases – methane ( $\text{CH}_4$ ), ethane ( $\text{C}_2\text{H}_6$ ), propane ( $\text{C}_3\text{H}_8$ ), and butane ( $\text{C}_4\text{H}_{10}$ ), carbon dioxide ( $\text{CO}_2$ ) and nitrogen ( $\text{N}_2$ ) – from pressurized cylinders are regulated to approximately 40 psig. As the pressurized gases expand, Joule-Thomson cooling is sufficiently strong to risk affecting the performance of the thermal mass flow controllers (MFCs, Brooks Smart mass flow series). To condition the gases to a stable temperature prior to reaching of the MFCs, the pressurized gases are fed through individual copper pipes approximately 7.5 meters long, coiled in a large water bath kept at a constant  $25^\circ\text{C}$  via a Thermo Scientific immersion heater (model number (M/N): SC 150).

Since the maximum flow rates of methane were much higher than other species, exacerbating the cooling effect, methane required two additional stages of thermal conditioning to provide a consistent temperature at the inlet of the MFC across all flow conditions. First, the methane was passed through a water-heated regulator (Alternative Fuel Systems, M/N: AFS 30-02029, heated using a second Thermo Scientific SC-150 immersion heater) and subsequently through approximately five meters of coiled copper tubing hung in the air space of the lab. The methane line then passed through the heated bath used by the remaining gases.



**Figure 2.2: Fuel supply, conditioning, and delivery and atomizer liquid supply, delivery, and frequency generator.**

The MFCs were calibrated using either a Sensidyne Gilibrator 2 bubble calibrator (for flows up to 30 LPM) or a Siemens Sitrans F C Mass 2100 Coriolis flowmeter (for higher flow rates). Table 2.1 summarizes the purity of the gases used, calibrated flow range, and the model number of each mass flow controller. Calibration curves were determined via linear least squares regression with 95% confidence interval for any given set point flow within the calibrated flow range. Each calibration point and its variance was determined via 10 readings of the Gilibrator 2 or Sitrans FC 2100 for a single set point.

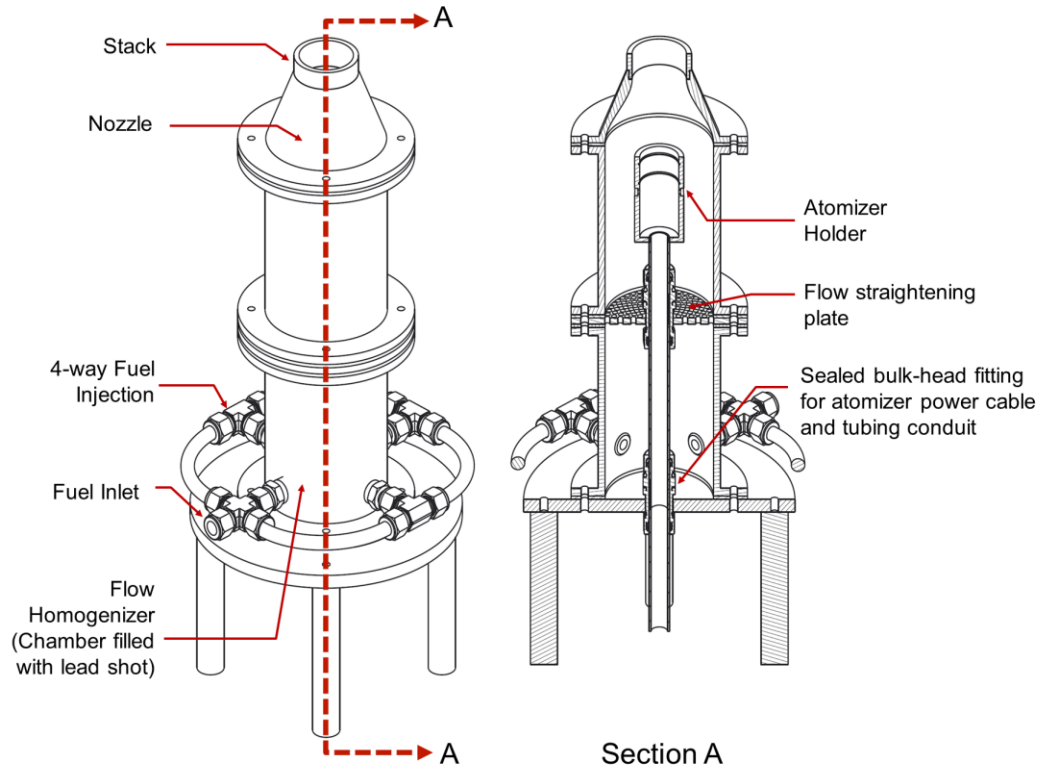
**Table 2.1: Hydrocarbon fuel MFC specifications and purity**

<b>Gas Species</b>	<b>MFC M/N</b>	<b>Purity [%]</b>	<b>Calibrated Range [SLPM]</b>	<b>Max Cal. Uncertainty [%]</b>
<b>Methane</b>	5853S	99.0	12-210	0.5%
<b>Ethane</b>	SLA5851S	99.0	3-49	3.15%
<b>Propane</b>	SLA5851S	99.0	1.25-23.75	4%
<b>Butane</b>	SLA5851S	99.0	0.25-3	1.5%

Approximately 0.3 m downstream of the MFCs, the gas lines were plumbed to a 0.60 m long, 50.8 mm diameter manifold which connected to approximately 12 m of  $\frac{3}{4}$  inch stainless steel tubing leading to the burner. A single fuel mix (referred to as “Heavy-4”) was used for the present experiments based on data detailed in Johnson and Coderre (2012). This mix contained 74.54%<sub>v</sub> methane, 15.47%<sub>v</sub> ethane, 6.83%<sub>v</sub> propane, and 3.16%<sub>v</sub> butane.

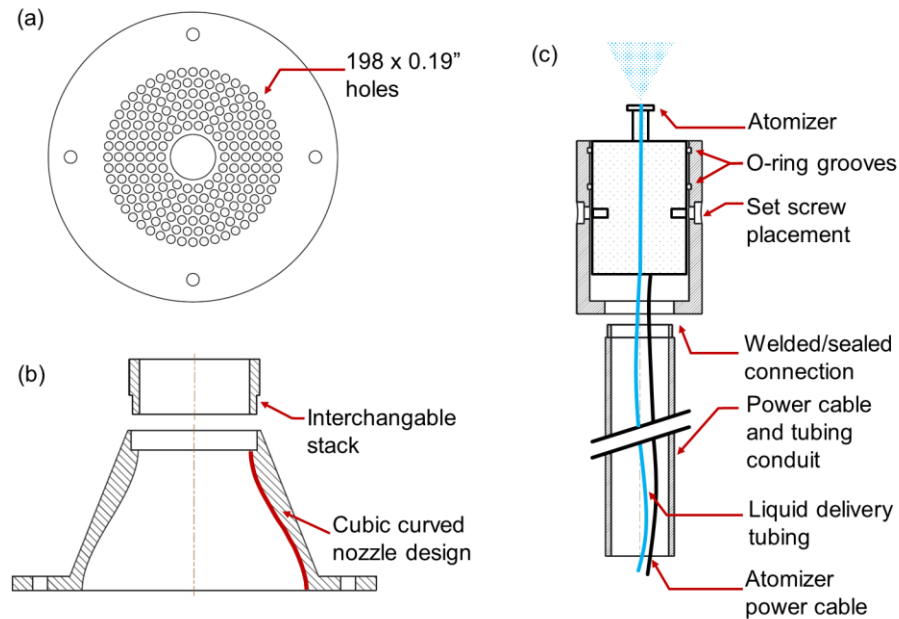
### **2.1.2 Burner and Aerosol Generation**

Figure 2.3 shows the custom-designed burner used in the present experiments. Originally designed by the University of Alberta, additions and modifications were made to improve functionality and allow for newer and smaller liquid atomizers (discussed in Section 2.1.3) to be located within the burner at an adjustable height. Machine drawings of each component of the burner can be found in Appendix A. The atomizers were used to inject liquid aerosols representative of the composition of FB/PW into the flare gas stream, mimicking a potential scenario of a FB flare. Each component of the burner will be discussed in this section.



**Figure 2.3: Custom atomizing burner assembly.**

As shown in Figure 2.3, fuel was injected into the lower portion of the burner via four equally spaced ports. This lower chamber was filled with lead shot of nominal 2 mm diameter to homogenize the flow prior to entering the flow straightener plate shown in the assembly, and in Figure 2.4(a) in more detail. The quarter-inch thick, 316 stainless steel flow-straightener plate consisted of six concentric rings of 0.19-inch diameter holes surrounding a central 25.9-mm diameter hole to accommodate the sealed tube containing the wires and liquid line for the atomizer. There were 18 equally spaced holes in the innermost, 36.3-mm diameter ring. Each successive ring was offset radially one-quarter inch from the previous ring and contained six additional holes.



**Figure 2.4: Details of atomizing burner assembly: a) flow straightener located in the atomizing burner, b) custom designed 2-inch burner nozzle, and 1-inch stack, and c) detail of atomizer holder.**

The burner exit components were modular such that 2- and 3-inch nozzles and stacks were easily interchanged. The cubic contour nozzles, Figure 2.4(b), contracted from the four-inch diameter body of the burner to the nominal diameter of the exit (2 or 3 inches) over a height of 2.5 inches. Each nozzle was threaded at its top with standard UNF threads (2.250"-16 and 3.250"-16) that were used to attach stacks of 1, 3, or 5 in heights. For the present experiments, only the 2-inch burner, with a 1-inch tall stack was used.

Atomizers were held concentrically in the burner with a custom-designed apparatus specific to each uniquely dimensioned atomizer as shown in Figure 2.3, and in more detail in Figure 2.4(c). Two O-rings sealed the atomizer from any liquid on the top of the atomizer holder from reaching the electrical connections underneath. The atomizers were secured in place with two M4 bolts. The conduit, also sealed, further separated the

electrical connections and liquid delivery from the flare gas stream. The burner base plate and straightening plate each had a straight-through  $\frac{3}{4}$ -inch bulkhead compression fitting with Teflon ferrules that allowed for simple height adjustment to place the atomizing tip at any height within the burner's upper section. The bulkhead fittings were equipped with a sealing washer, ensuring no gas leaked from the burner. The atomizer tips were placed three inches below the stack exit plane.

### **2.1.3 Ultrasonic Atomizers**

Two ultrasonic atomizers, manufactured by Sono-Tek, were used in the present experiments as detailed in Table 2.2. The operating frequency of each atomizer, 120- or 180-kHz, corresponded to a nominal droplet size. Manufacturer-specified expected droplet diameter distributions when atomizing water are plotted in Figure 2.5. The distributions were noted to be very similar, which is likely why it was difficult to detect any droplet size effects as further discussed in Chapter 4. Both atomizers were cylindrical with a diameter of 1.44 inches and height of 1.49 or 1.59 inches (120- and 180-kHz versions respectively). The 120-kHz atomizer was made of a proprietary corrosion-resistant alloy to preserve the life-span of the nozzle when subjected to the corrosive saltwater mixtures used in the present experiments. The 180-kHz was not available in the anti-corrosive material.

The atomizers were powered by an ultrasonic generator (Sono-Tek, M/N: ECHO) that was externally controlled via a LabVIEW VI. The generator allowed for precise load-levelling to ensure optimal power was delivered to the atomizer for a specific flow rate and type of liquid. Flow rate ranges and operating points were determined via discussion with the manufacturer and testing at various power levels. While the atomizer was active, the load levelling was manually reduced until the atomizer stalled (i.e. ceased to atomize, or

atomized inconsistently). A setting 5-10% above this stall point was initially chosen as the optimal operating point based on fluid type, and qualitative inspection of the atomization. The highest sustainable operating load was at 50% of maximum power. The 180-kHz nozzle required an extra cable converter for the present experiments that was suspected to cause a power loss. This subsequently required the nozzle to operate at 50% power for all liquid flow rates.

**Table 2.2: Sono-Tek ultrasonic atomizer specifications and operation conditions**

<b>Atomizer <math>f</math> [Hz]</b>	<b>M/N</b>	<b>Median <math>\emptyset</math> [<math>\mu\text{m}</math>]</b>	<b>Sauter mean <math>\emptyset</math> [<math>\mu\text{m}</math>]</b>	<b>Flow rate range [mL/min]</b>	<b>Optimal Power Setting [%]</b>
<b>120 kHz</b>	NZL120CO	19	41	2-15	36-45%
<b>180 kHz</b>	NZL180	13	26	1-8	50%

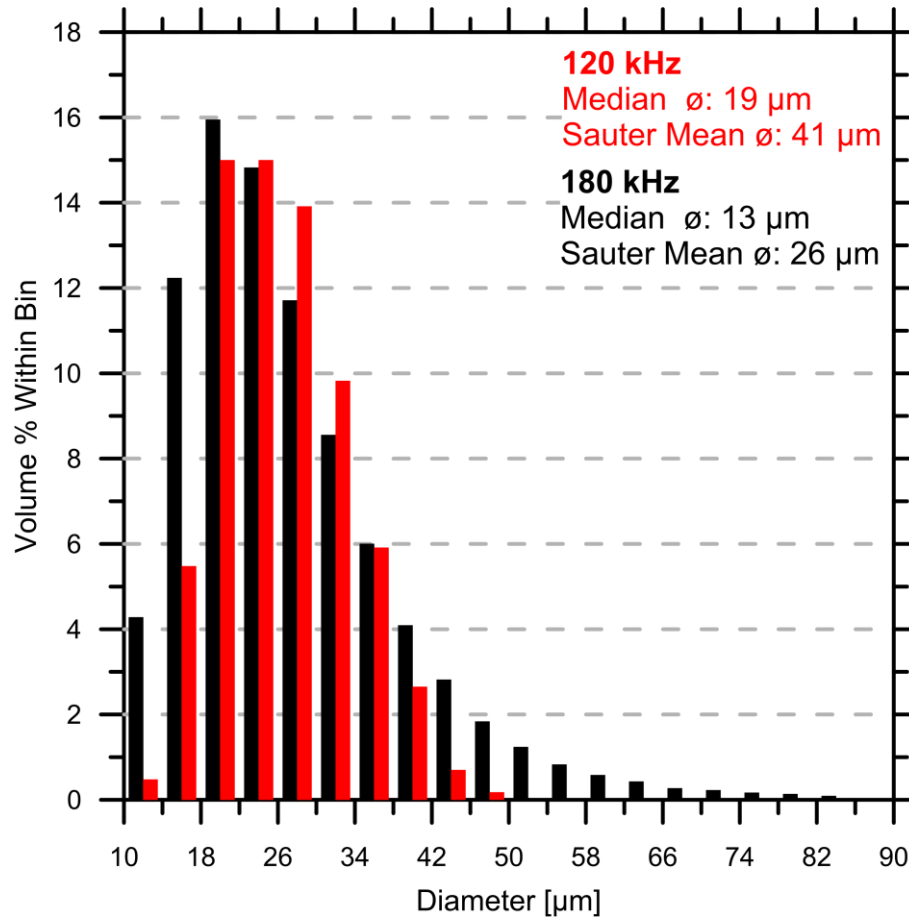


**Figure 2.5: Sono-Tek atomizers manufacturer specified droplet diameter distributions for the 120 kHz (red), and 180 kHz (black) atomizers.**

Liquid was delivered to the atomizer via a precision micro gear pump (Ismatec/Cole-Parmer ISM901B) with a suction-shoe head (Ismatec/Cole-Parmer L21834) that was capable of pumping liquids from 0.85 mL/min to 85 mL/min with a 3% bias error. The pump was calibrated by measuring the total mass of water pumped over a specific time to determine a mass flow rate, which was converted to a volume flow rate using the fluid density corresponding to the measured room temperature. When switching among liquid types, the line was purged with distilled water to avoid cross-contamination of the liquid reaching the flare.

Tests with distilled water at maximum and minimum flow rates through the atomizers for each nozzle showed that at less than or equal to the three-inch level, few to no liquid droplets hit the inner sides of the burner or stack for the range of flow rates capable by the atomizers. Figure 2.6 shows results of a visual observation of the flow pattern of the aerosols when injected via the 120-kHz nozzle into a co-flow of ambient temperature air (20°C) at 0.00175 kg/s (matching the mass flow rate of fuel at 109.45 SLPM). The figure shows that the spray pattern was a narrow cone and droplets would be expected to enter the flame along its centerline rather than impinging on the burner walls. Similar behavior was seen with the 180-kHz nozzle.

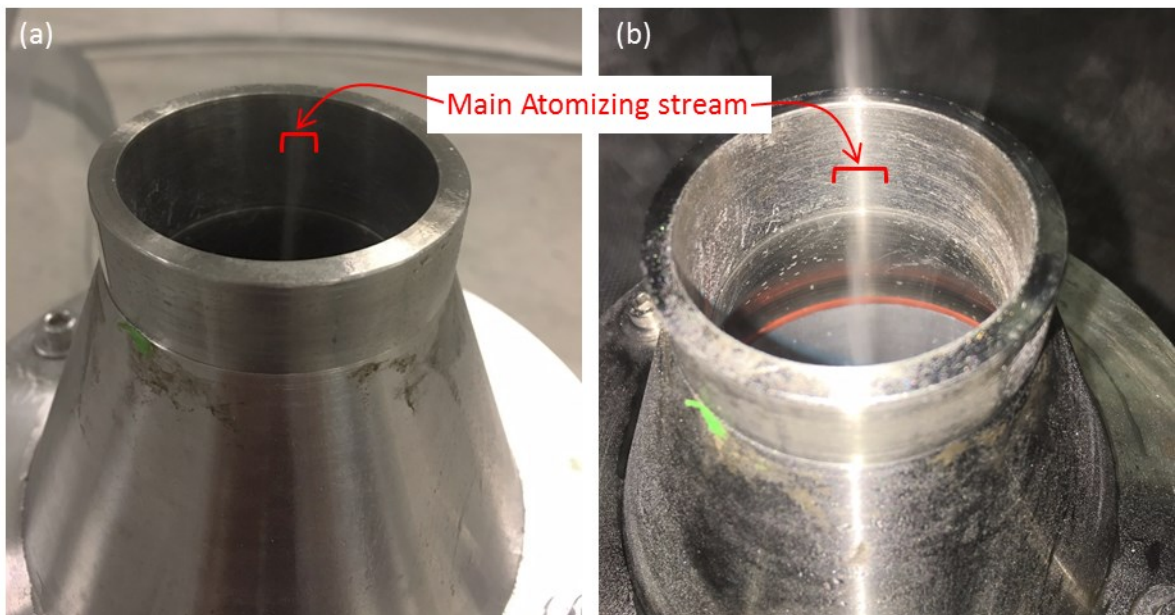


**Figure 2.6: Atomizing streams of the 120 kHz nozzle with co-flow of ambient temperature air (20°C) at 0.00175 kg/s (matching the mass flow rate of fuel at 109.45 SLPM) at (a) 2 mL/min and (b) 15 mL/min of distilled water.**

Based on the  $D^2$  evaporation law (Turns, 2012), the adiabatic flame temperature of the flare (2241 K), and droplet sizes from 10 to 50  $\mu\text{m}$ , the droplets would be expected to have lifetimes on the order of 0.1 to 1 ms. Alternatively, noting that the temperature rises along the centerline of the flame, for a nominal constant temperature of 150°C the

maximum droplet lifetime would be approximately 50 ms. Considering a nominal flare exit plane velocity of 0.9 m/s, these droplets would be expected to travel no more than approximately 50 mm before evaporating.

## **2.2 Gas and Solid-Phase Combustion Emissions Measurements**

Combustion emissions mixed with dilution air were sampled via either a heated conductive sample line (for particulates) or an unheated sample line (for gaseous species). As detailed in Table 2.3, a range of primary combustion emissions analyzers for CO<sub>2</sub>, CO, CH<sub>4</sub>, NO<sub>x</sub>, and particulate matter were used. Figure 2.7 shows a schematic of the gas- and solid-phase species sampling probe set up. Gases were sampled from a closed-ended, 1/4" diameter, multi-holed stainless steel probe inserted 13.9" into the bottom of the 15.7" diameter duct. Four 1/8" diameter upstream facing holes were drilled along the probe. The gas sampling probe extended out of the duct via a sealed fitting, and connected through a cross fitting to unheated 1/4" Teflon tubes extending down to the NO<sub>x</sub>, CO/CO<sub>2</sub> and CH<sub>4</sub> analyzers.

To reduce time needed per test, a post-background reading (see section 2.2.4) was taken near the gas analyzing equipment, allowing the burner to stay lit (at a lower flow rate to conserve gas) and remain at or near its stabilized temperature. Solenoid valves (1/4" for gas-phase Assured Automation M/N: A33DGXV4B; 3/8" for solid-phase Assured Automation M/N: B33DGXV4B) were triggered to either sample from the duct, or sample ambient air. Instrument exhaust gases were plumbed directly to a downstream port of the sampling duct so as not to interfere with background readings.

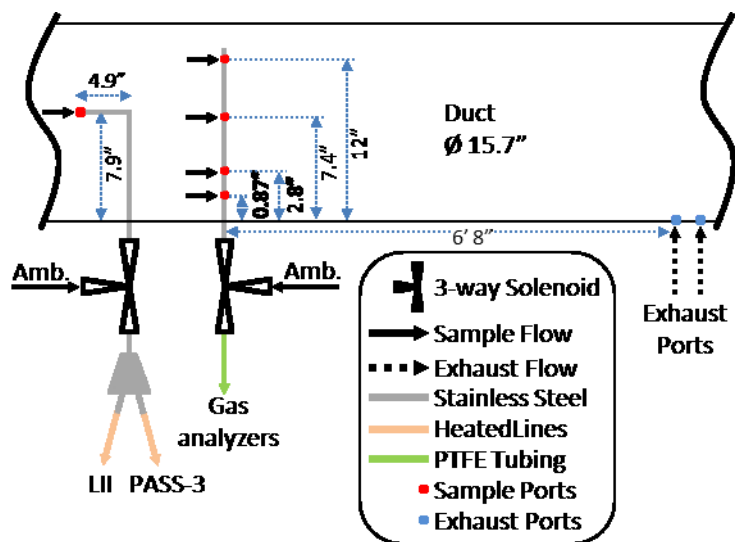


Figure 2.7: Gas- and solid-phase species sampling and exhaust setup.

Table 2.3: Gas- and solid-phase combustion emission analyzer specifications and calibration methods

Instrument	Measured Species	MDL	Precision	Calibration Range	
Thermo Fisher Scientific 42i	NO	0.4 ppb	1%	0.205-5.03 ppm (NO)	
	NO <sub>2</sub>	0.4 ppb	1%		
Los Gatos Research CRD (CO/CO <sub>2</sub> )	CO	0.5 ppb	1%	Manufacturer's Calibration	
	CO <sub>2</sub>	200 ppb			
	H <sub>2</sub> O	3 ppm			
Los Gatos Research CRD (CH <sub>4</sub> /C <sub>2</sub> H <sub>2</sub> )	CH <sub>4</sub>	2 ppb	1%	Manufacturer's Calibration	
	C <sub>2</sub> H <sub>2</sub>	1 ppb			
	H <sub>2</sub> O	100 ppm			
Droplet Measurement Technologies PASS-3	Particulate Matter: $\sim 20$ 1/Mm $B_{abs,\lambda}$ & $B_{scat,\lambda}$	1% (Typical)	$\lambda$	$B_{abs,\lambda}$ [1/Mm]	$B_{scat,\lambda}$ [1/Mm]
			405 nm:	550-54,000	200-18,000
			532 nm:	360-37,000	120-12,000
			870 nm:	230-23,000	45-4,500
Artium LII Soot Spectrometer	Soot volume fraction	1 ppt	20%	0.02-0.2 ppb	

## 2.2.1 Nitrogen Oxides (NO<sub>x</sub>)

NO<sub>x</sub> was measured using a Thermo Fisher Scientific 42i Chemiluminescent analyzer. The instrument was calibrated using compressed bottles of zero air, 0.205 ppm NO in N<sub>2</sub> (0.207 ppm total NO<sub>x</sub>)  $\pm$  2% (low-range), and 5.03 ppm NO in N<sub>2</sub> (5.06 ppm total NO<sub>x</sub>)  $\pm$  2% (high-range). A third bottle of calibration gas (1.02 ppm NO in N<sub>2</sub>, 1.03 ppm total NO<sub>x</sub>,  $\pm$  2%) was used as a final calibration check. Calibration was completed each day

experiments were conducted. During experiments, the instrument was operated in dual range mode: 0.2 to 2 ppm (low) and 2 to 200 ppm (high), in which the instrument automatically selected the appropriate range.

### **2.2.2 Carbon Monoxide, Carbon Dioxide, Methane**

Two Los Gatos Research cavity ringdown (CRD) gas analyzers were used to measure carbon monoxide, carbon dioxide, and methane concentrations in the exhaust duct. The instruments do not require regular calibration, per manufacturer's instructions, though calibration gas was periodically sampled to ensure no significant drift was seen in the readings. Calibration gases used were 850 ppm CO<sub>2</sub>, 0.3 ppm CO and 0.65 ppm CH<sub>4</sub> ( $\pm 10\%$ ); 1500 ppm CO<sub>2</sub>, 1.5 ppm CO and 2.5 ppm CH<sub>4</sub> ( $\pm 5\%$ ); and 5400 ppm CO<sub>2</sub>, 5 ppm CO and 3.5 ppm CH<sub>4</sub> ( $\pm 5\%$ ).

### **2.2.3 Aerosol Species**

Optical properties of solid-phase combustion products samples were measured with a Droplet Measurement Technologies (DMT) PASS-3 (photoacoustic soot spectrometer) and an Artium laser induced incandescence (LII) soot spectrometer. The PASS-3 was used to measure absorption and scattering coefficients of particulate matter (PM) emitted by the flare, whether carbonaceous or otherwise. The LII instrument was used as a complementary aerosol sampling method, where for typical combustion systems (i.e. without entrained salts) the LII measured the carbonaceous component of soot. Used in tandem, disparity in the composition of the PM created by the flare can be deduced. Both instruments sampled from a 3/8" stainless steel tube bent 90° such that the opening of the probe faces upstream in the duct. The probe extended vertically through a sealed port in the bottom of the duct (see Figure 2.7). The sample is divided via a custom-built Y-splitter

and the pipe fittings are heated to 65°C. From this junction, heated lines (Technical Heaters, M/N: 212, 10 ft for LII and 7 ft for PASS-3) directed samples to the LII and PASS-3. The sample tubes of the heated lines were constructed of carbon-impregnated PTFE hose to reduce any sample loss due to static build up. The probe, fittings, and sample lines were heated to reduce thermophoretic losses.

### ***2.2.3.1 Photoacoustic Soot Spectrometer Calibration***

The PASS-3 employs lasers at 405, 532, and 870 nm wavelengths to induce a photoacoustic effect in its sample chamber, which is used to measure the absorption coefficient of the particulate in the sample. Scattering coefficients are simultaneously measured via nephelometry. In series, each laser is modulated via a square wave and successively directed through the sample resonator cell containing a gas sample with particulates. The resonator cell has a resonant frequency dependent on temperature, pressure, and the relative humidity of the sample. The frequency of the square-wave is matched to the resonant frequency of the cell. The particles in the sample absorb and scatter the laser light resulting in a periodic heating of the surrounding gas within the cell at the resonance frequency. A microphone measures the resulting pressure wave (sound wave) generated by the periodic heating of gases and can be used to measure the absorption coefficient ( $B_{abs,\lambda}$ , in units of 1/Mm) of the sample. The scattering coefficient,  $B_{scat,\lambda}$  in 1/Mm, at each wavelength is measured via photomultiplier tube readings detecting signals from an integrating sphere within the instrument.

The theory of calibration for the PASS-3 stems from the instrument's ability to measure scattering, absorption, and extinction independently. The extinction coefficient ( $B_{ext,\lambda}$ ) is the sum of the scattering coefficient ( $B_{scat,\lambda}$ ) and the absorption coefficient ( $B_{abs,\lambda}$ ):

$$B_{ext,\lambda} = B_{scat,\lambda} + B_{abs,\lambda} \quad (2.1)$$

Using Beer's Law, Equation (2.2), the extinction coefficient at each wavelength is calculated by measuring the transmitted power through a filtered (particulate-free) sample ( $I_0$ ) and through a particle-laden sample ( $I$ ):

$$B_{ext,\lambda} = \frac{-1}{L} \ln \left( \frac{I_\lambda}{I_{0,\lambda}} \right) \cdot 10^6 \quad (2.2)$$

where  $L$  is the path length of the laser (0.2486 m in the PASS-3). Because this is a relative measurement, assuming the laser power detectors are linear, they do not need to be separately calibrated.

The scattering signal was calibrated first. Using a nebulizer system, spherical polystyrene latex (PSL) particles which strongly scatter and negligibly absorb light were sampled by the PASS-3. In this case, Equation (2.1) simplified to  $B_{ext,\lambda} = B_{scat,\lambda}$  which allowed the PASS-3 scattering readings to be calibrated by correcting the instrument's scattering reading to the extinction coefficient calculated by Equation (1.2).

The absorption coefficient was subsequently calibrated using strongly absorbing particles (i.e. soot from an inverted methane flame in this case). Since scattering from these particles was not negligible, the absorption signal was calibrated against the measured extinction minus the measured scattering. This can be shown by rearranging Equation (2.1):

$$B_{abs,\lambda} = B_{ext,\lambda} - B_{scat,\lambda} \quad (2.3)$$

where  $B_{ext,\lambda}$  is calculated via Equation (2.2) and previously calibrated  $B_{scat,\lambda}$  readings are taken from the instrument. Additional details and examples of calibration calculations are provided in Appendix B.

When only carbonaceous soot particles are being sampled, the measured absorption coefficient from the PASS-3 instrument can be converted to a soot volume fraction via Rayleigh-Debye-Gans (RDG) polydisperse fractal aggregate theory (Köylü and Faeth, 1996) shown in Equation (1.4). The RDG model is accurate to within 10% for PM that absorbs significantly more than it scatters, and for which primary particle diameter ( $d_p$ ) size falls within Rayleigh scattering (i.e.  $\pi \cdot d_p/\lambda < 0.3$ ) (Coderre et al., 2011).

$$f_v = \frac{\lambda B_{abs,\lambda}}{6\pi E(m)_\lambda} \cdot 10^3 \quad (2.4)$$

where:  $f_v$  is the soot volume fraction in ppb;

$\lambda$  is the laser wave length in nm; and

$E(m)_\lambda$  is the absorption soot refractive index function, estimated as  $0.332 \pm 0.0878$  ( $2\sigma$ ) for each wavelength (Johnson et al., 2013)

### **2.2.3.2 Laser-Induced Incandescence Instrument Calibration**

The LII is calibrated yearly. In March 2016, the LII was sent to the National Research Council's Measurement Science and Standards Department for calibration. To calibrate the LII, a soot source was directed to the LII and to a filter following the National Institute of Occupational Health and Safety, NIOSH, 5040 sample and analysis procedures. With controlled sampling time and flow rates, the total mass of soot measured on the filter was converted into a concentration in  $\text{mg}/\text{m}^3$ . Samples of three concentrations, each with three

sample points were collected. The concentration readings from the LII were plotted against the filter-calculated concentrations; the slope of the through-origin regression (LII on X, filter on Y) represented the calibration factor and was input into the instrument's software. The calibrated soot volume fraction range was 0.02 – 0.20 ppb.

#### **2.2.4 Experimental Methodology**

Measured concentration data of relevant combustion product species in the duct were streamed to the DAQ at 0.5 Hz. These data were collected for 5-12 minutes depending on the stability of the concentration readings. Concentrations were considered to be stable when the average concentration over the previous 20 seconds was within  $\pm 5\%$  of the average of the last 60 seconds. Because the temperature of the flare gas at the burner exit can affect sooting propensity (Guo et al., 2016), a standard warm-up protocol was developed. As the flame heats the burner, the flare gas can become pre-heated. The temperature of the outside surface of the burner was monitored in real-time and calculations were performed to determine temperature stability of the flare gas at the exit of the flare stack. The latest 10 data points (20 seconds) were fitted to a second-order polynomial, and the slope of the last point was calculated. Projecting 1000 seconds, the total rise in temperature was tracked. Plotting these temperature rises reveals a decaying exponential curve. Fitting this curve, a steadying time was predicted based on the time at which the rise in temperature over 1000 seconds would be less than 5°C. It was found that the changes seen in concentrations of the combustion species at temperatures rises less than or equal to 5°C per 1000 seconds was less than the precision error of the species yield measurements. It was clear then that the point at which the burner temperature had stabilized, the concentration readings had also stabilized.

Species yields were calculated via a methodology proposed in Corbin and Johnson (2014). Based on a mass-balance approach of carbon in the flare gas, combustion products, and ambient air, accurately measured concentrations of key species in the exhaust duct and ambient air can be used to calculate species yields (i.e. mass emission rate of a species per mass flow rate of flare gas). Uncertainties in these calculations are detailed in Corbin and Johnson (2014) and follow standard error propagation as outlined in ANSI/ASME (1985).

# Chapter 3

## Initial Results and Data Reduction

### 3.1 Summary and Design of Experiments

The present experiments were designed to attempt to provoke an effect on flare combustion emissions via the injection of various non-hydrocarbon aerosols into the flare gas stream. Parameters explored included liquid composition, liquid loading, and droplet size. The burner diameter (2"), flare gas composition (heavy-4), and flare gas flow rate (109.45 SLPM, 0.9 m/s exit velocity) were kept constant during all tests.

Table 3.1 summarizes the experiments performed which included two different median droplet sizes, six liquid types, and nine liquid loadings measured as percent of the mass of pure water per mass of flare gas. Experiment conditions with an asterisk in Table 3.1 indicate that multiple experiments were performed to investigate repeatability and approximate precision errors on individual test conditions.

**Table 3.1: Experimental Matrix**

	Liquid Loading [kg water/kg flare gas ×100%]								
	1	2	3	5	7	7.5	8.5	10	14.3
<b>Dry*</b>	-	-	-	-	-	-	-	-	-
<b>Distilled Water (DW)</b>	-	19 μm	-	19 μm	-	19 μm	-	19 μm*	19 μm
<b>Tap Water (TW)</b>	-	19 μm	-	19 μm	-	19 μm	-	19 μm	19 μm
<b>3.17% HCl</b>	-	19 μm	-	19 μm	-	19 μm	-	19 μm	19 μm
<b>9.51% HCl</b>	-	19 μm	-	19 μm	-	19 μm	-	19 μm	19 μm
<b>5.00% NaCl</b>	13 μm	19 μm	13 μm	19 μm 13 μm	13 μm	19 μm*	13 μm	19 μm	19 μm
<b>15.0% NaCl</b>	13 μm	19 μm*	13 μm	19 μm* 13 μm	13 μm	19 μm*	13 μm	19 μm*	19 μm*

\* Experiments were repeated multiple times (6× dry, 3× DW, 5× 5% NaCl, 5× each loading of 15% NaCl)

Injected liquid compositions were chosen to investigate the most prevalent species found in FB liquids, namely sodium anions and chlorine ions as discussed in the context of Figure 1.2. Using dry gas mixtures (no injected aerosols) and distilled water aerosols as base cases, aqueous solutions of NaCl (5% and 15% by weight) were chosen to represent the 25<sup>th</sup> and 95<sup>th</sup> percentiles of FW. Aqueous HCl was chosen as a third liquid type to inject into the flare (3.17% and 9.51% by mass). The concentrations of HCl were selected to correspond to the 5 and 15% salt solutions by matching the total mass percent of chlorine and water. Matching 5% NaCl with 3.17% HCl (and 15% NaCl with 9.51% HCl) allowed the effects of added Cl ions to be tested independently of the addition of Na cations while keeping the water loading constant between each pair of solutions.

Figure 3.1 shows a sample plot of measured carbon monoxide (CO) yield for flare tests with injected dry (black), 5% NaCl (red), 15% (pink) NaCl, and DW (blue) aerosols of nominal 19 μm diameter droplets. The horizontal axis indicates the mass of aerosolized

water in the injected solution as a function of the mass flow rate of flare gas (expressed in percent consistent with Table 3.1). The vertical axis plots the CO yield, where yields presented in this thesis are expressed as grams of the species of interest emitted per kg of flare gas (FG).

Each data point on Figure 3.1 shows uncertainties: solid error bars represent instrument bias error, and dotted error bars represent total error which includes instrument bias and precision calculated through multiple tests. As mentioned above, not every test condition was performed multiple times. The shaded band overlaid on the data points represents an estimated total uncertainty for those data points not repeated, based on a similar case's precision error as further discussed in Section 3.2. In the case of the 5% solution shown in Figure 3.1, the absolute precision calculated from five tests at 7.5% loading was extrapolated to the lower and higher loadings. For the 15% salt solution, repeated tests were conducted at each loading level and discussed in Section 3.2. The rationale for this was two-fold: first, the magnitude of yields and scattering and absorption readings of DW, TW, and HCl aerosol tests were of the same order over the range of liquid loading; and second, it was impractical to repeat every test condition summarized in Table 3.1 due to time constraints and the expense of the fuel gas supply.

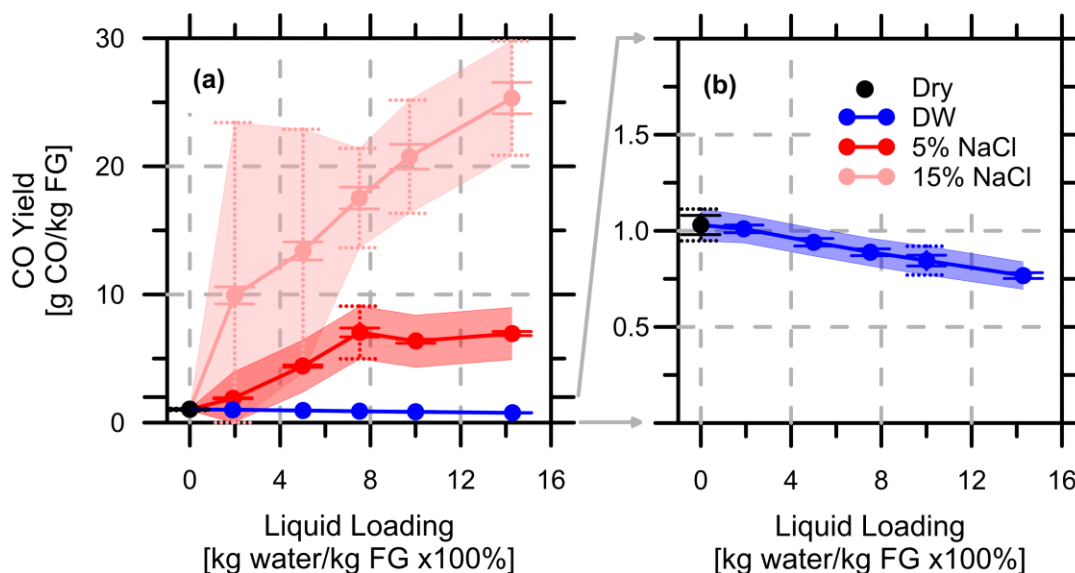


**Figure 3.1:** (a) CO yield of Heavy 4 flare gas at 109.45 SLPM versus liquid loading of injected 19  $\mu\text{m}$  (nominal) aerosols of 5% (red) and 15% (pink) aqueous NaCl. A comparable dry case (without injected aerosols) is also shown (black). Dotted error bars represent true total uncertainties, solid error bars represents bias, and shaded regions represent an extrapolated total uncertainty for bias-only measurements. Plot (b) is a re-scaled plot of (a) to better illustrate dry and DW test results and uncertainties.

### 3.2 Repeatability of Aerosol Injection System

As illustrated in Figure 3.1 (b), the precision errors in measured CO yields were very small ( $\sim 8\%$ ) for the dry flare gas experiments (black filled circle). Precision uncertainty was similarly and consistently small for the distilled water ( $\leq 8\%$ ). However, repeated tests of both salt solution experiments showed significantly larger apparent precision uncertainties – tests with the 5% NaCl solution (5 repeats at 7.5% loading) showed an initially calculated precision uncertainty of 29% and tests with 15% NaCl solutions (5 repeats at each of 5 loadings) revealed apparent precision uncertainties from 17% to 135%. This trend of anomalous uncertainties in measured species yields with the NaCl solutions was consistent for all measured gas species and particulate matter parameters (i.e. CO, CH<sub>4</sub>, and NO<sub>x</sub> yields and particulate matter absorption and scattering coefficients).

The results presented in Figure 3.1 were cause to suspect the atomizing system was not performing consistently between identical tests, especially with the NaCl solutions. This was further supported by visual observation of the atomizer nozzle during experiments. In some cases, the visible spray would appear to “sputter” intermittently such that a consistent and steady spray of aerosol droplet was not delivered to the flame. In extreme cases, the atomizer could stall completely, which was immediately apparent through a sudden drop in CO emissions back to levels of the dry case. When this occurred, the entire experiment had to be halted and restarted. If the stall was not immediately detected, unatomized liquid could collect in the base of the burner, requiring the gas lines to be purged, and the burner dismantled and cleaned.

During offline tests, it was discovered that increasing the power delivered to the atomizer could eliminate the disruptive stalling. However, this meant the operating point deviated from the manufacturer’s recommended power setting (see Section 2.1.3) and the intermittent sputtering behaviour was qualitatively worse. Since it was imperative to avoid full stalling of the atomizer to be able to run experiments, this meant some sputtering of the nozzle during measurements was unavoidable.

### **3.2.1 Data Processing and Outlier Detection of 5% and 15% Salt Solution Tests Cases**

Because of these observed and suspected inconsistencies in the performance of the atomizer during the tests conducted with 5% and 15% NaCl solutions, separate statistical analysis of the results was warranted. The objective of this analysis was to identify potential outlier cases in the measured yield data and solid-phase optical property data

measured during tests with both salt solutions which would be attributable to the unstable operation of the atomizer.

Figure 3.2 shows individual trials for the experiments with injected nominal 19  $\mu\text{m}$ , 15% NaCl aerosols. Single test results for all other cases are shown in Appendix D. Trial 1 (solid line) differs significantly from Trials 2 through 5, most notably at lower liquid loading levels. Trial 1 is thus suspected as an outlier, with effective operating conditions different than those of Trials 2 through 5.

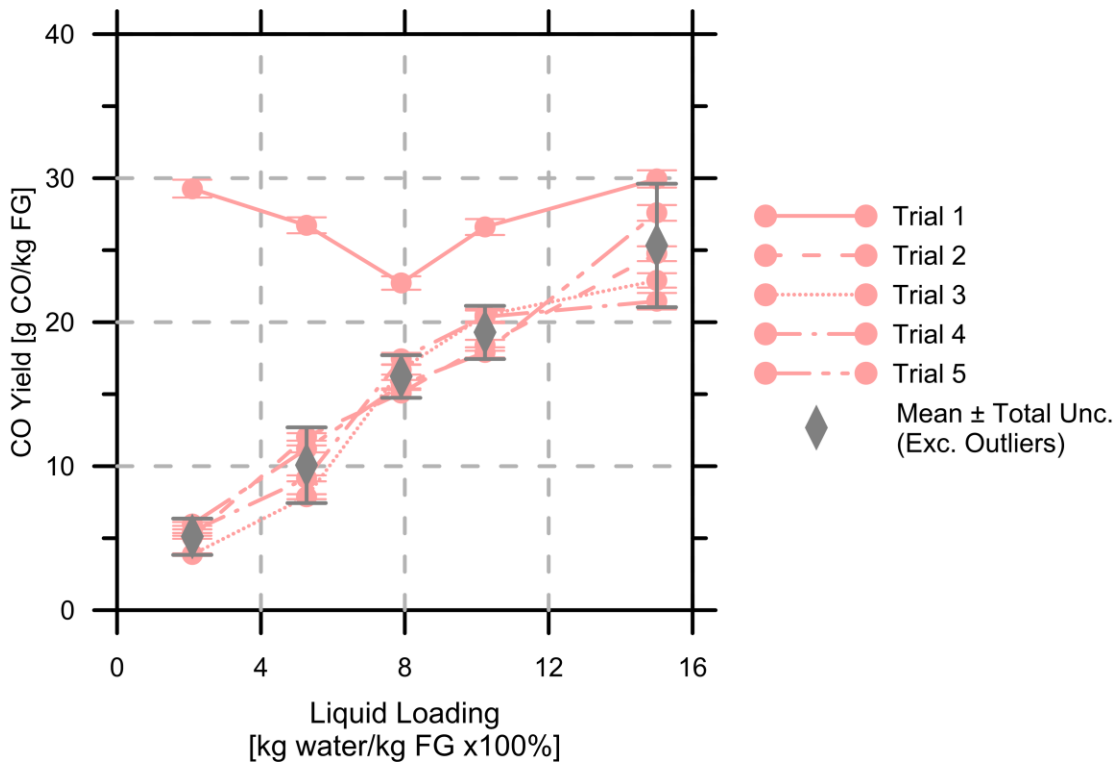


**Figure 3.2: CO yield of Heavy 4 flare gas at 109.45 SLPM versus liquid loading of 19  $\mu\text{m}$  15% aqueous NaCl. Instrument bias errors are included on each individual data point. Grey diamonds represent the average of the repeated trials at each liquid loading set point. Error bars on the diamonds are the calculated total uncertainty of the average excluding any outliers.**

To aid in the objective identification of outlier data as part of supporting meaningful conclusions from the data collected, Grubb's outlier detection test was used. The Grubb statistic (G) is calculated as:

$$G = \frac{x_{outlier} - \mu}{\sigma} \quad (3.1)$$

where:  $x_{outlier}$  is the suspected data point;

$\mu$  is the mean of the data set including the outlier and;

$\sigma$  is the standard deviation of the data set including the outlier.

The critical value ( $G_{crit}$ ) is calculated according to Equation (3.2)

$$G_{crit} = \frac{(n-1)t}{\sqrt{n(n-2+t^2)}} \quad (3.2)$$

where  $n$  is the number of tests and  $t$  is defined as the student t critical value at  $n-2$  degrees of freedom calculated at a chosen significance level ( $\alpha \leq 0.05$  in the present case such that the probability of false rejection of data, Type I error, was less than 5%). If  $G \geq G_{crit}$ , the suspected point is said to be an outlier within the specified confidence interval. Grubbs' test was chosen as it is suitable if the data set has a single suspected outlier, and is normally distributed when the outlier is excluded (Grubbs, 1950). The Shapiro-Wilks test was used to verify normality.

Table 3.2 summarizes the findings of the outlier and normality tests for the repeated measurements of CO, NOx, and CH<sub>4</sub> yield, and  $B_{abs,\lambda}$  and  $B_{scat,\lambda}$  for five liquid loadings of 15% NaCl. Each set of repeated measurements for each species or property was deemed normally distributed (per the Shapiro-Wilks test) when the outlier, if detected, was removed from the set. Only results from Trial 1 were detected as outliers for every

measured species or property. No outliers were detected for any measured property of the five repeated tests of 5% NaCl at 7.5% loading.

**Table 3.2: Summary of Grubbs' Test of outliers (Trial 1, 95% confidence) for repeated tests of 15% NaCl experiments.**

Measured Property	Liquid Loading [kg water/kg flare gas ×100%]				
	2% (15% NaCl)	5% (15% NaCl)	7.5% (15% NaCl)	10% (15% NaCl)	14.3% (15% NaCl)
CO Yield	✓	✓	✓	✓	
NOx Yield	✓	✓	✓	✓	✓
CH <sub>4</sub> Yield	✓	✓	✓	✓	
405 nm Abs.		✓		✓	✓
532 nm Abs.		✓	✓	✓	✓
870 nm Abs.		✓		✓	✓
405 nm Scat.	✓	✓	✓	✓	✓
532 nm Scat.	✓	✓	✓	✓	✓
870 nm Scat.	✓	✓			✓

✓ = Outlier

Final precision uncertainties (excluding the outlier data from Trial 1) were calculated by Equation (3.3):

$$P = \frac{t_{n-1,95\%}\sigma}{\sqrt{n}} \quad (3.3)$$

where:  $P$  is the precision error in absolute units;

$t$  is the two-tailed student  $t$  value at 95% with degrees of freedom of the number of repeated tests,  $n-1$ ; and

$\sigma$  is the sample standard deviation of the respective property or yield calculated during each repeated test.

Total uncertainty was calculated by adding  $P$  in quadrature with the average bias error found on each repeated point. The average of the non-outlier points and their associated total uncertainties are plotted as grey diamonds in Figure 3.2.

For the remainder of the results presented in this thesis: 15% NaCl test results will be presented as mean values with their associated total uncertainty excluding outliers. Dry, DW, and 5% NaCl repeated tests will be presented as averages of the data as collected with associated total uncertainties. For non-repeated test conditions, instrument bias uncertainties are shown along with estimated total uncertainties calculated based on the measured precision uncertainties of similar tests.

# Chapter 4

## Results and Discussion

### **4.1 Effect of Liquid Loading on Carbon Monoxide and Methane Emissions**

Figure 4.1 shows measured CO yields for the lab-scale flare with injected 19  $\mu\text{m}$  (nominal) droplets of DW, TW, 3.17% HCl, and 9.51% HCl. Also shown for comparison are CO yields from a reference dry case without injected droplets. As discussed in Section 3.2, solid error bars represent instrument bias, dotted error bars represent a true total uncertainty calculated with multiple measurements, and the shaded regions represent approximate total uncertainty for any unrepeated measurements. In the case of Figure 4.1, only dry and DW at 10% loading experiments were repeated; the shaded region on the remaining DW loadings and all loadings of TW, 3.17% HCl, and 9.51% HCl are the absolute total uncertainty of the DW at 10% loading.

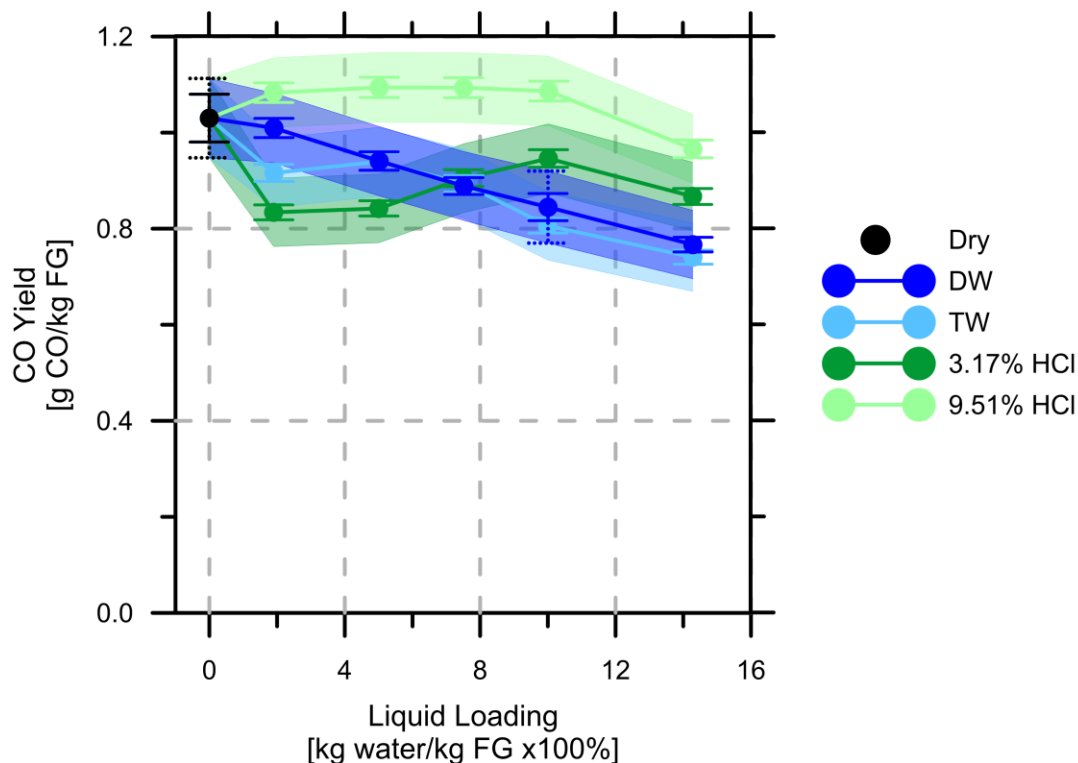


**Figure 4.1: CO yield vs liquid loading of dry (i.e. 0% loading), DW, TW, 3.17% HCl, and 9.51% HCl aerosols of median diameter of 19  $\mu\text{m}$ . Shaded bands represent approximate total uncertainties and error bars represent instrument bias. True total uncertainties were calculated for: dry; 10% loading of DW indicated by the dotted error bars.**

As the DW or TW loading was increased, the CO yield decreased by approximately 25% at the maximum droplet loading of 14.3% (i.e. the dry case CO yield of 1.03 g/kg FG decreased to 0.76 g/kg FG for DW and 0.74 g/kg FG for TW at 14.3% loading). The decreasing trend was consistent with the literature discussed in Section 1.4: the addition of water promotes the oxidation of CO via the water-gas shift reaction, effectively causing a decrease in the CO yield as water loading increases. Additionally, the added water should reduce the flame temperature which would increase the effectiveness of the forward reaction of the water-gas shift (see Section 1.4). Based on equilibrium calculations using NASA's Chemical Equilibrium with Applications (CEA) software, the adiabatic flame temperature at the maximum liquid loading of water would be expected to decrease by 27 K relative to a dry flame (from 2241 K to 2214 K). It is likely then that the majority of

the decrease in CO emissions was from water's chemical effect via the water-gas shift reaction rather than a thermal effect on the flame. Within the estimated experimental precision bands, injected TW (light blue) and DW (dark blue) had similar effects on CO yield over the range of liquid loadings tested. This could be expected since, as further detailed in Appendix C, tap water contained only minor quantities of contaminants, the highest concentrations of which were: sodium (~16 ppm), calcium (~8.4 ppm), chloride (~6.6 ppm), TDS (~2.67 ppm).

Effects of injected HCl solutions on CO yields were more complex, and may have been indicative of competing effects of added Cl and added water. Tests with injected 3.17% HCl acid solution (dark green) showed a sharper decrease in CO yield from dry to 2% liquid loading compared to the DW and TW results. However, after this initial decrease, CO yield then increased slightly over 2% to 7.5% loading where the trend aligned with results of DW and TW from 7.5% to 14.3% loading. With the 9.51% HCl solution, CO yield increase slightly from dry to 10% loading, before decreasing more steeply from 10% to 14.3% loading. Based on the literature discussed in Chapter 1.4, in isolation, chlorine would be expected to act as an OH radical scavenger, reducing the availability of the required radicals for CO oxidization reactions effectively increasing CO yield. However, the water in the solution could be expected to have the opposite effect.

As shown in Figure 4.2, injected 5% and 15% NaCl solutions had a very significant effect on CO yields, to the point that previously detailed effects with dry, water, and acid solutions seemed negligible by comparison. With the 5% salt solution, CO yield increased by a factor of ~7 from dry to 7.5% loading (0.86 g/kg FG to 7.03 g/kg FG), before levelling out as loading further increased to 14.3% loading. The CO yield trend with the injected

15% NaCl solution increased monotonically with loading up to 27.58 g/kg FG by 14.3% loading (a factor of 25 increase from the dry case). As the aqueous NaCl solution droplets are introduced to the flare gas and begin to evaporate due to the elevated temperatures, salt crystals will likely reform. However, not all droplets would have equal numbers of Na<sup>+</sup> and Cl<sup>-</sup> ions, which would lead to some release of free chlorine or sodium. It is also likely that NaCl crystals would subsequently melt or boil releasing additional free Na<sup>+</sup> and Cl<sup>-</sup> into the system. At 100 kPa, the melting and boiling points of NaCl crystal are 800.8°C and 1465°C, which are both well below the adiabatic flame temperature of 1941°C<sup>7</sup>. Vaporized NaCl could reform itself further in the flame or plume as the temperature decreases below the boiling point. Condensing NaCl could also provide a nucleation surface for soot to form, potentially creating internally-mixed aggregates of NaCl and carbon.

---

<sup>7</sup> Calculated using CEA for flare gas mixture of 74.54%v methane, 15.47%v ethane, 6.83%v propane, and 3.16%v butane with a maximum water loading of 14.3% (kg water/kg flare gas ×100%).

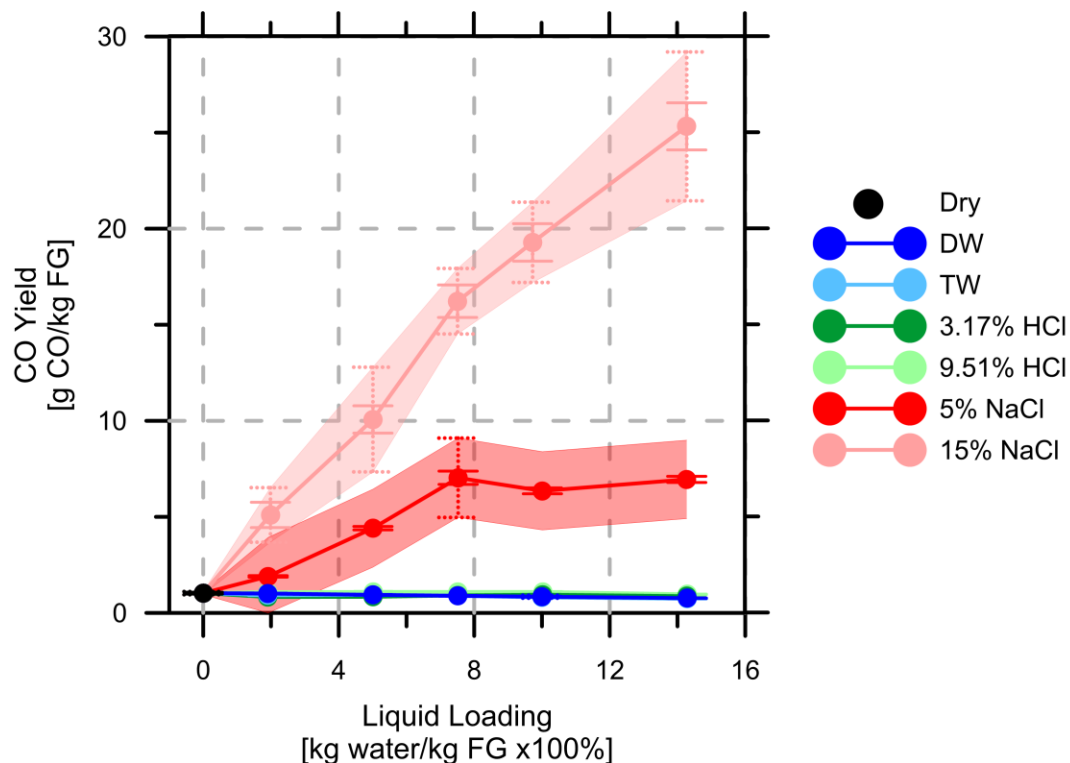


**Figure 4.2: CO yield vs. liquid loading of dry (i.e. 0% loading), DW, TW, 3.17% HCl, 9.51% HCl, 5% NaCl, and 15% NaCl aerosols of median diameter 19  $\mu\text{m}$ . Shaded bands represent approximate total uncertainties and error bars represent instrument bias. True total uncertainties were calculated for: dry; 10% loading of DW; 7.5% loading of 5% NaCl and; all loadings of 15% NaCl indicated by the dotted error bars.**

The mass flow rate of chlorine between 3.17% HCl and 5% NaCl (and 9.51% HCl and 15% NaCl) at each liquid loading (as defined by the total mass flow of water in the solution, not the mass of the solution) was designed to be of equal magnitude. Thus one would expect that if chlorine alone was the primary influencer affecting CO yield, the acid/salt pair would cause a similar effect. This was clearly not the case. The disparity in effect on CO yield thus allows for two speculative conclusions. First, the source of chlorine could play a large role in how it affects the combustion process and HCl as a source is not as effective as NaCl. HCl introduces hydrogen radicals that may affect other reactions in the combustion process, including critical chain-propagating and chain-terminating

reactions of the CO oxidation mechanism. Second, the sodium in the salt may be affecting CO yield.

The effect of water, salt, and acid aerosols on other gas-phase species were investigated. Figure 4.3 shows methane yield for 5% and 15% salt solutions injected as 19  $\mu\text{m}$  median diameter droplets. Similar to the CO yield results, methane yields with injected 5% NaCl solution increased steadily up to 7.5% loading, before levelling out at 0.285 g/kg FG by 14.3% loading. Methane yields with the injected 15% NaCl droplets increased monotonically from zero (dry case) to 1.90 g/kg FG at 14.3% loading. By contrast, water, and acid tests (not plotted) showed essentially zero methane emission, matching the dry case. That injected water droplets at tested loadings at or below 14.3% did not increase methane yield could be expected; steam injection experiments conducted by Torres et al. (2012) showed that methane production was only affected when injecting large amounts of water ( $\geq 50\%_{\text{m}}$  liquid loading). The difference in effects of HCl and salt solutions on  $\text{CH}_4$  yields paralleled that on CO yields. This result furthers the supposition that chlorine source and/or sodium are influential factors affecting the gas-phase combustion processes.

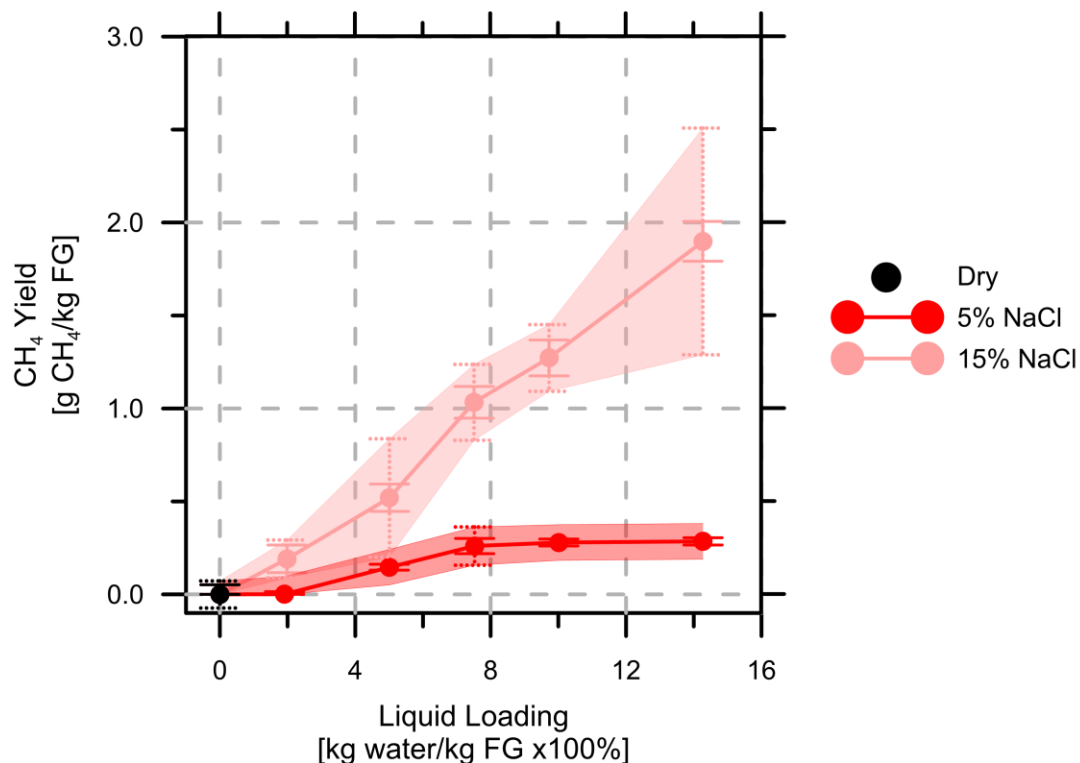


**Figure 4.3: CH<sub>4</sub> yield vs liquid loading of dry (i.e. 0% loading), 5% NaCl, and 15% NaCl aerosols of median diameter 19  $\mu\text{m}$ , and 5% NaCl and 15% NaCl aerosols of median diameter 13  $\mu\text{m}$ . Shaded bands represent approximate total uncertainties and error bars represent instrument bias. True total uncertainties were calculated for: dry; 7.5% loading of 5% NaCl (19  $\mu\text{m}$ ) and; all loadings of 15% NaCl (19  $\mu\text{m}$ ) indicated by the dotted error bars.**

Effects of droplet size were also investigated. Figure 4.4(a)-(b) compares CO and methane yields respectively from flames with injected 5% and 15% NaCl solutions via two nominal droplet diameters: 19  $\mu\text{m}$  (red and pink) and 13  $\mu\text{m}$  (dark purple and light purple). Within the estimated total uncertainty bounds, Figure 4.4(a)-(b) shows that changing the droplet size from 13 and 19  $\mu\text{m}$  had no apparent effect on CO or methane yield when loading was held constant. It is most likely that the droplet size distributions were not distinct enough from one another to induced detectable effects on emission yields. Similarly, it is also possible that any effect that might have occurred was undetectable within the experimental bias or precision. Lastly, given the estimated droplet lifetimes of <50 ms briefly discussed in Section 2.1.3, it is also likely that the 19  $\mu\text{m}$  nominal size is

below the critical droplet diameter for this flame. As discussed in Section 1.4, droplets introduced to the flame less than or equal to the critical size affected flame extinguishment equally.

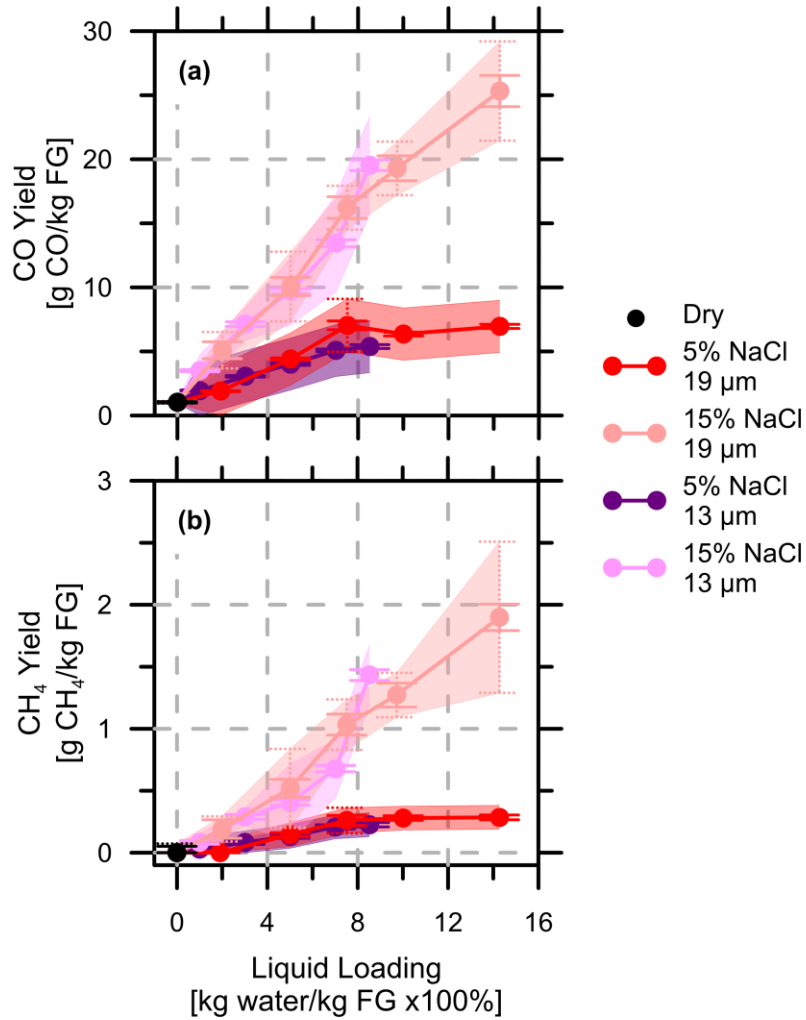


**Figure 4.4: CO yield vs liquid loading of dry (i.e. 0% loading), 5% NaCl, and 15% NaCl aerosols of median diameter 19 μm, and 5% NaCl and 15% NaCl aerosols of median diameter 13 μm. Shaded bands represent approximate total uncertainties and error bars represent instrument bias. True total uncertainties were calculated for: dry; 7.5% loading of 5% NaCl (19 μm) and; all loadings of 15% NaCl (19 μm) indicated by the error bars.**

## 4.2 Nitrogen Oxides (NO<sub>x</sub>)

Figure 4.5 shows NO<sub>x</sub> yields of flares with injected with DW, TW, HCl solutions (3.17% and 9.51%), and NaCl solutions (5% and 15%) of nominal 19 μm droplet size. NO<sub>x</sub> yields

of flares with injected DW, TW, and acid aerosols arguably showed a slight decrease as liquid loading level increased. Since the thermal mechanism (where production rate is exponentially dependent on temperature) is the dominant mode of NO<sub>x</sub> formation in turbulent, non-premixed flames (Turns, 2012), as discussed in Section 1.4 injected water could be expected to cool the flame leading to a decrease in NO<sub>x</sub> formation. However, any decrease seen in Figure 4.5 was within the estimated precision uncertainties of the measurements.

Both the chemical (via reactions with chlorine) and thermal (via vaporization of water) effects from these experiments were expected to decrease NO<sub>x</sub> formation as discussed in Chapter 1.4. Thus, it would be expected that the addition of chlorine via HCl to the flame would cause a greater decrease in NO<sub>x</sub> yield than tests with water. However, the observed trends in the acid solution tests were no different than those of the distilled water tests (within precision bounds). Similar to the characteristics of CO yields, the most dramatic effect on NO<sub>x</sub> were seen in the tests with injected salt solutions. NO<sub>x</sub> yields decreased with increased liquid loading and the effect was stronger for the higher concentration salt solution. For the 5% NaCl solution, measured NO<sub>x</sub> yields decreased by 20% -- from 1.71 g NO<sub>x</sub> / kg FG in the dry flame to 1.37 g/kg FG at 14.3% loading. Over the same loading range, NO<sub>x</sub> yields with the 15% NaCl solution decreased by 26% (to 1.26 g/kg FG). Although there was some overlap of precision bounds with DW, TW, and acid tests exists, both salt solution tests consistently created less NO<sub>x</sub>.

That corresponding pairs of HCl and NaCl solutions (with matching Cl loading) did not affect the flame equivalently again supports the preliminary conclusions discussed

in Section 4.1: either the source of chlorine is critical in how it affects the flame, or the sodium, as opposed to chlorine, is the dominant influencer of CO and NO<sub>x</sub> yield.

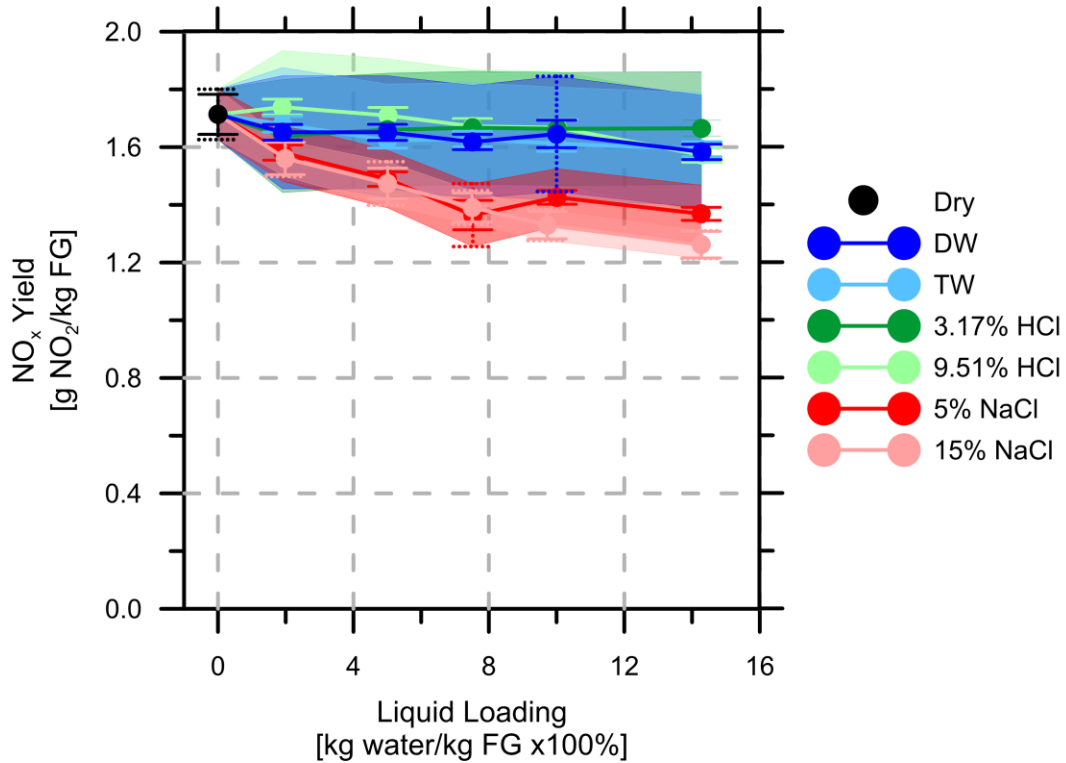


**Figure 4.5: NO<sub>x</sub> yield vs liquid loading of dry (i.e. 0% loading), DW, TW, 3.17% HCl, 9.51% HCl, 5% NaCl, and 15% NaCl aerosols of median diameter 19  $\mu\text{m}$ . Shaded bands represent approximate total uncertainties and error bars represent instrument bias. True total uncertainties were calculated for: dry; 10% loading of DW; 7.5% loading of 5% NaCl and; all loadings of 15% NaCl indicated by the dotted error bars.**

The effect of droplet size on NO<sub>x</sub> yield was also investigated. Figure 4.6 shows NO<sub>x</sub> yields of the flare injected with 5% and 15% NaCl aqueous solutions at nominal droplet sizes of 13  $\mu\text{m}$  and 19  $\mu\text{m}$ . There was no apparent effect of droplet size on observed NO<sub>x</sub> yields. As discussed with CO yield measurements, the difference in droplet size distributions could have been too small to induce a difference in measured species yields or the “critical” droplet size for this flare may have been at or above 19  $\mu\text{m}$ .

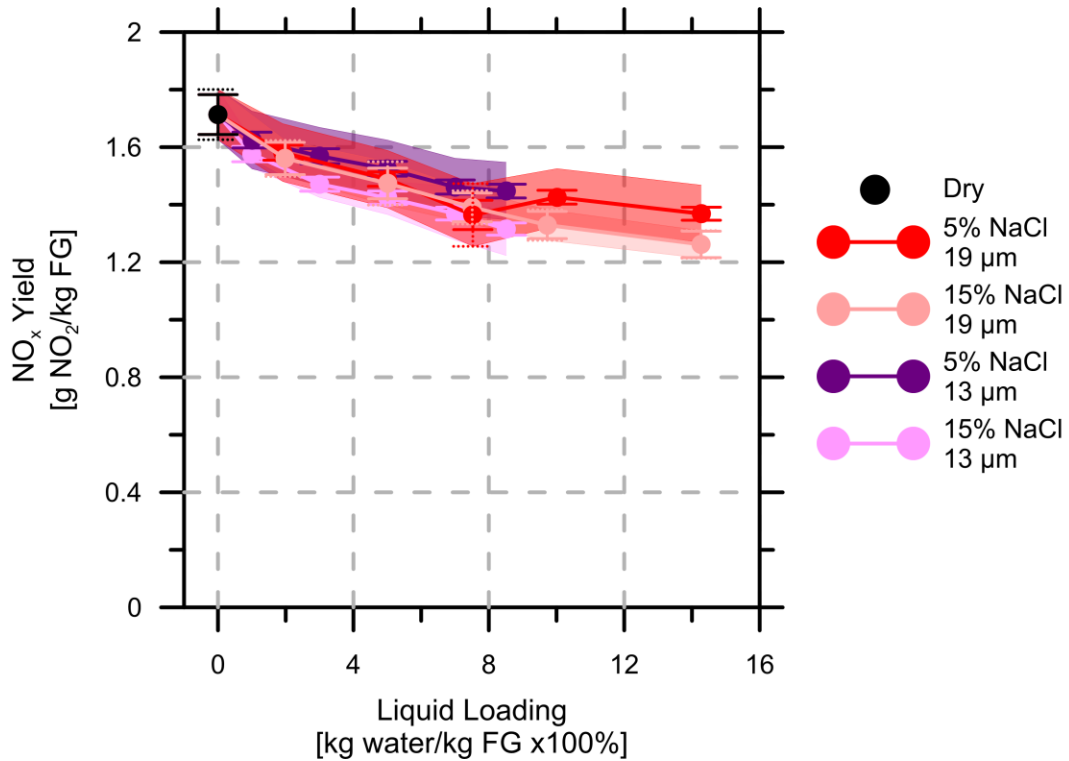


**Figure 4.6: NO<sub>x</sub> yield vs. liquid loading for 5% NaCl, and 15% NaCl aerosols of median diameter 13 and 19 μm. Shaded bands represent estimated total uncertainties and error bars represent calculated instrument bias. True total uncertainties were calculated for: dry; 7.5% loading of 5% NaCl (19 μm) and; all loadings of 15% NaCl (19 μm) indicated by the dotted error bars.**

### 4.3 Effect of Injected Aerosols on Emitted Particulate Matter

The total light extinction (sum of absorption and scattering) for DW, TW, and acid solution experiments is plotted in Figure 4.7. Considering the precision uncertainties as noted in Table 4.1, both water cases (DW and TW) caused a decrease in total extinction with increasing loading at all wavelengths, suggesting a decrease in the amount of emitted particulate. This result was expected – steam injection is a common practice in industrial flaring to reduce visible soot (Allen and Torres, 2011). Further, Kazemimanesh (2014) noted that both distilled water and 1% HCl decreased total particle number emissions from lab-scale methane flames. In the present results, the acid solutions (3.17% and 9.51% HCl) also showed decreases in the measured total light extinction at all three wavelengths.

However, absolute readings of scattering and absorption were similar between the water and acid tests.

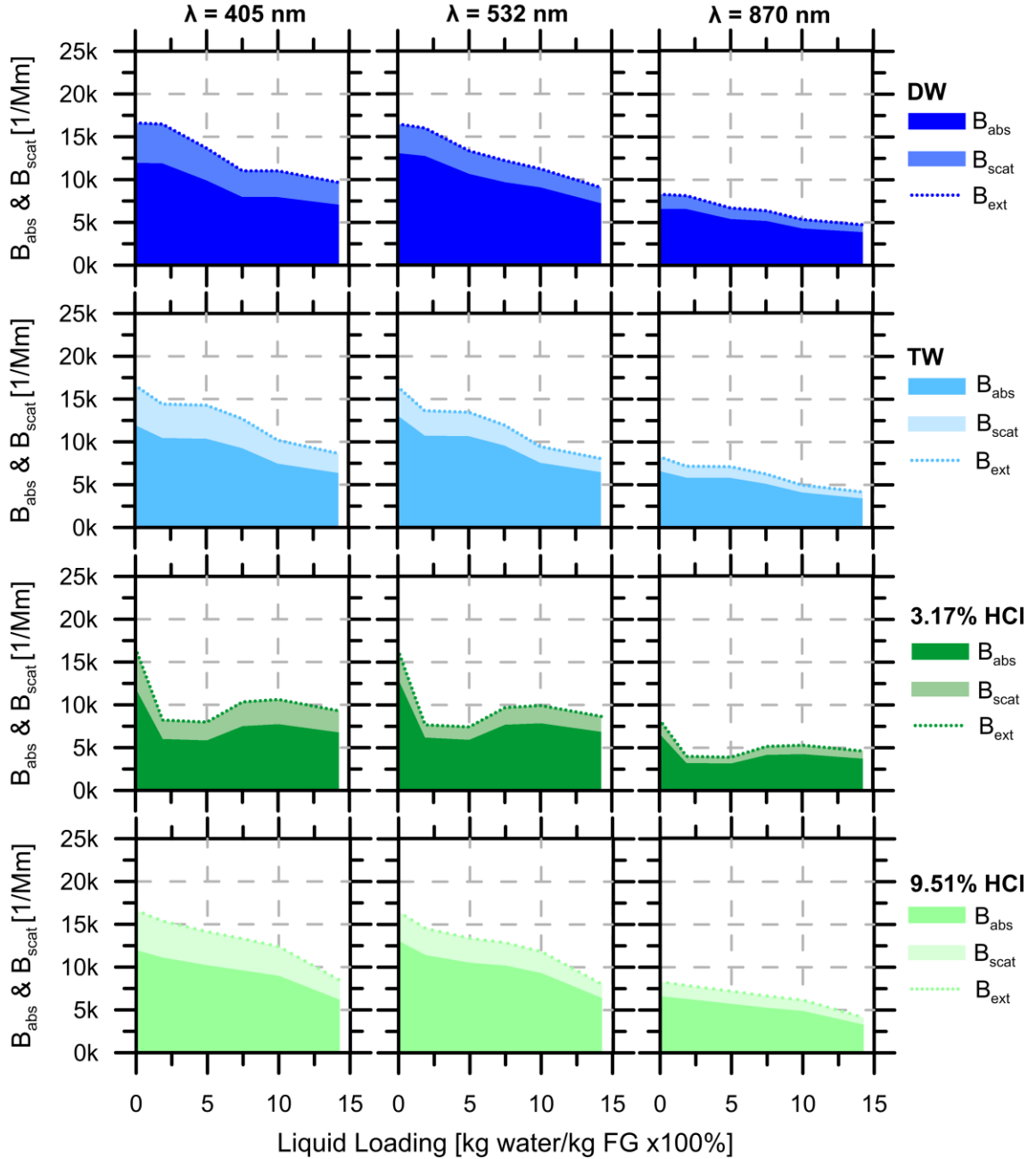


**Figure 4.7: Absorption (solid fill) and scattering (lighter stacked fill) coefficients vs. liquid loading for flames injected with 19  $\mu\text{m}$  aerosols of DW, TW, 3.17% HCl, and 9.51% HCl. The total extinction is represented by the sum of each component. Total uncertainties are presented in Table 4.1.**

**Table 4.1: Measured  $B_{\text{abs}}$  and  $B_{\text{scat}}$  and estimated uncertainties dry cases and tests with 19  $\mu\text{m}$  aerosols of DW, TW, 3.17% HCl, and 9.51% HCl.**

Test	405 nm		532 nm		870 nm	
	$B_{\text{abs}}$ [1/Mm]	$B_{\text{scat}}$ [1/Mm]	$B_{\text{abs}}$ [1/Mm]	$B_{\text{scat}}$ [1/Mm]	$B_{\text{abs}}$ [1/Mm]	$B_{\text{scat}}$ [1/Mm]
<b>Dry</b>						
-	11951± 944	13079± 508	6616± 1700	4662± 396	3404± 606	1675± 273
<b>DW</b>						
2% Loading	11902± *	12714± *	6576± *	4579± *	3295± *	1556± *
5% Loading	9885± *	10630± *	5404± *	3780± *	2706± *	1293± *
7.5% Loading	7932± *	9666± *	5175± *	3084± *	2532± *	1203± *
10% Loading	7932± 2450	9063± 420	4313± 730	3084± 328	2177± 1480	1051± 58
14.3% Loading	7057± *	7197± *	3886± *	2602± *	1839± *	854± *
<b>TW</b>						
2% Loading	10469± *	10723± *	5845± *	3948± *	2909± *	1344± *
5% Loading	10366± *	10640± *	5802± *	3910± *	2828± *	1323± *
7.5% Loading	9252± *	9536± *	5103± *	3450± *	2422± *	1148± *
10% Loading	7450± *	7549± *	4095± *	2746± *	1914± *	881± *
14.3% Loading	6332± *	6441± *	3428± *	2304± *	1597± *	727± *
<b>3.17% HCl</b>						
2% Loading	5994± *	6171± *	3228± *	2217± *	1516± *	768± *
5% Loading	5828± *	5924± *	3161± *	2152± *	1511± *	747± *
7.5% Loading	7508± *	7674± *	4151± *	2829± *	2036± *	1016± *
10% Loading	7727± *	7858± *	4248± *	2902± *	2088± *	1048± *
14.3% Loading	6771± *	6867± *	3728± *	2523± *	1801± *	895± *
<b>9.51% HCl</b>						
2% Loading	11091± *	11422± *	6274± *	4264± *	3119± *	1578± *
5% Loading	10193± *	10522± *	5739± *	3925± *	2861± *	1453± *
7.5% Loading	9611± *	10174± *	5256± *	3699± *	2694± *	1379± *
9.73% Loading	8961± *	9342± *	4898± *	3425± *	2475± *	1268± *
14.25% Loading	6163± *	6380± *	3293± *	2306± *	1629± *	829± *

The following symbols indicate that uncertainties were not directly calculated; estimated with value of precision for the respective property calculated by:

\*: 19  $\mu\text{m}$  aerosols of DW at 10% loading

Figure 4.8 shows the absorption, scattering, and total extinction coefficients measured during tests of the 5% and 15% salt solutions injected as either 13  $\mu\text{m}$  droplets (purple and light purple respectively) or 19  $\mu\text{m}$  droplets (red and pink respectively). For clarity, uncertainties are not shown on Figure 4.8 and instead are reported in Table 4.2. Noting the change in scale from Figure 4.7, Figure 4.8 shows the magnitudes of light scattering and absorption were significantly larger than in the water and acid tests, especially at high liquid loading levels. Absorption results of dry, water, and acid tests remained below 12.5k 1/Mm, whereas 5% and 15% NaCl caused absorption coefficients

of 23k and 54k 1/Mm respectively at maximum loading. The high absorption readings likely indicate a true increase in particulate matter. As NaCl is a strong scatterer and does not absorb at the PASS-3 wavelengths, it is unlikely that the higher absorption readings were due to the added presence of stand-alone NaCl particles. This would also be consistent with the gas-phase results where it was demonstrated that NaCl tests sharply increased other products of incomplete combustion (CO in Figure 4.3 and CH<sub>4</sub> in Figure 4.4).

As shown in Figure 4.8, there was no discernable difference in magnitude of absorption and scattering when the nominal droplet size of the injected NaCl solutions was changed from 13 μm to 19 μm. The similarities between the two droplet tests could yet indicate that there is “critical diameter” at or above 19 μm, below which changes in droplet size did not influence particulate emissions or CO, NO<sub>x</sub>, and CH<sub>4</sub> yields (as discussed in Section 4.1).

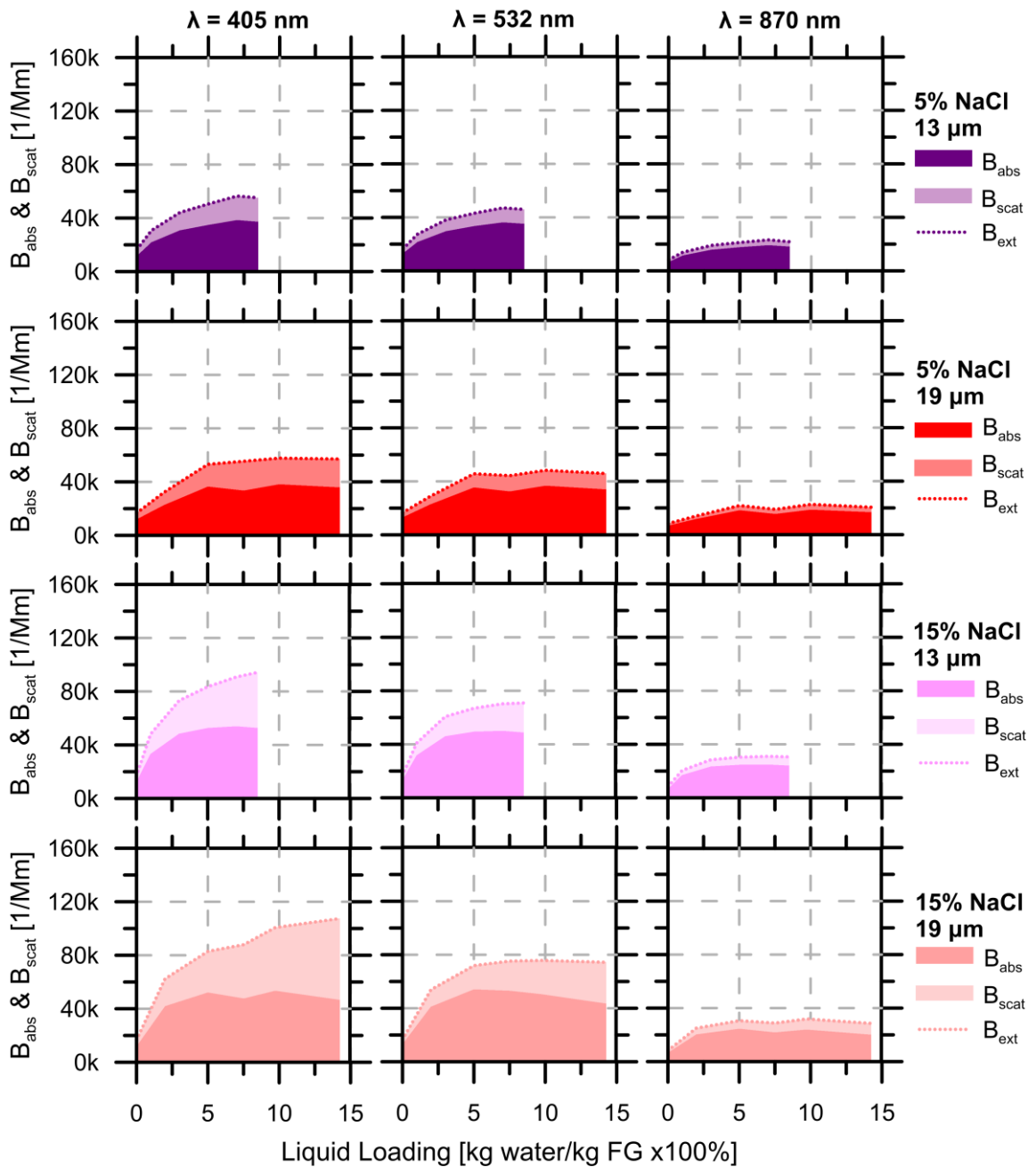


**Figure 4.8: Absorption (solid fill) and scattering (lighter stacked fill) coefficients vs. liquid loading of 5% NaCl, and 15% NaCl aerosols of 13  $\mu\text{m}$  and 19  $\mu\text{m}$  median diameter. See Table 4.2 for total uncertainty estimates.**

**Table 4.2: Measured  $B_{abs}$  and  $B_{scat}$  and estimated uncertainties tests with 19  $\mu\text{m}$  and 13  $\mu\text{m}$  aerosols of 5% and 15% NaCl.**

Test	405 nm		532 nm		870 nm	
	$B_{abs}$ [1/Mm]	$B_{scat}$ [1/Mm]	$B_{abs}$ [1/Mm]	$B_{scat}$ [1/Mm]	$B_{abs}$ [1/Mm]	$B_{scat}$ [1/Mm]
<b>5% NaCl, 13 <math>\mu\text{m}</math></b>						
1% Loading	21730± *	8997± *	21445± *	5932± *	11480± *	2425± *
3% Loading	30874± *	13337± *	29679± *	8438± *	15890± *	3239± *
5% Loading	34960± *	15624± *	33534± *	9659± *	17658± *	3614± *
7% Loading	38473± *	18013± *	36284± *	10844± *	19247± *	3907± *
8.5% Loading	37091± *	18128± *	35199± *	10748± *	17988± *	3732± *
<b>5% NaCl, 19 <math>\mu\text{m}</math></b>						
2% Loading	22660± *	9420± *	22559± *	6080± *	11561± *	2255± *
5% Loading	36337± *	16739± *	35311± *	10377± *	18148± *	3640± *
7.5% Loading	33453±5710	21962±3710	32341±6520	11951± 696	15440±3610	3491± 407
10% Loading	38149± *	19559± *	36554± *	11678± *	18712± *	3906± *
14.3% Loading	35695± *	21370± *	33907± *	11861± *	16785± *	3633± *
<b>15% NaCl, 13 <math>\mu\text{m}</math></b>						
1% Loading	33291± §	14890± §	31622± §	9227± §	17064± §	3387± §
3% Loading	48375± §	24888± §	46061± §	14657± §	23334± §	5019± §
5% Loading	52639± †	30941± †	49470± †	17484± †	24727± †	5598± †
7% Loading	53873± ‡	37023± ‡	50088± ‡	20128± ‡	24818± ‡	6106± ‡
8.5% Loading	52764± ‡	41627± ‡	48721± ‡	22159± ‡	24056± ‡	6545± ‡
<b>15% NaCl, 19 <math>\mu\text{m}</math></b>						
2% Loading	41900± 9510	20412± 2870	41028± 10600	12850± 2020	20160± 5470	4858± 720
5% Loading	52270± 1070	30612± 2680	53961± 6260	17939± 1640	24411± 466	6159± 319
7.5% Loading	47790± 7820	40155± 1930	53088± 3530	22206± 700	21754± 3920	7058± 638
9.73% Loading	53350± 4400	47432± 1240	50525± 2590	25287± 788	23783± 1910	8069± 1550
14.25% Loading	46571± 4010	60992± 3070	43457± 3380	30878± 1190	20035± 1500	8484± 616

The following symbols indicate that uncertainties were not directly calculated; estimated with value of precision for the respective property calculated by:

- \*: 19  $\mu\text{m}$  aerosols of 5% NaCl at 7.5% loading
- §: 19  $\mu\text{m}$  aerosols of 15% NaCl at 2% loading
- †: 19  $\mu\text{m}$  aerosols of 15% NaCl at 5% loading
- ‡: 19  $\mu\text{m}$  aerosols of 15% NaCl at 7.5% loading

Figure 4.9 shows the ratios of measured scattering to absorption coefficients ( $B_{scat,\lambda}/B_{abs,\lambda}$ ) of emitted particulate at 405 nm for dry, water, and acid tests. Similar plots for this ratio at 532 nm and 870 nm are shown in Appendix E. Within the estimated total uncertainties, there was no variation of the ratio among dry, distilled water, tap water, and acid tests. Additionally, the ratio does not appear to be dependent on liquid loading and ranged from 0.36 to 0.39 with uncertainties of order  $\pm 0.15$ .

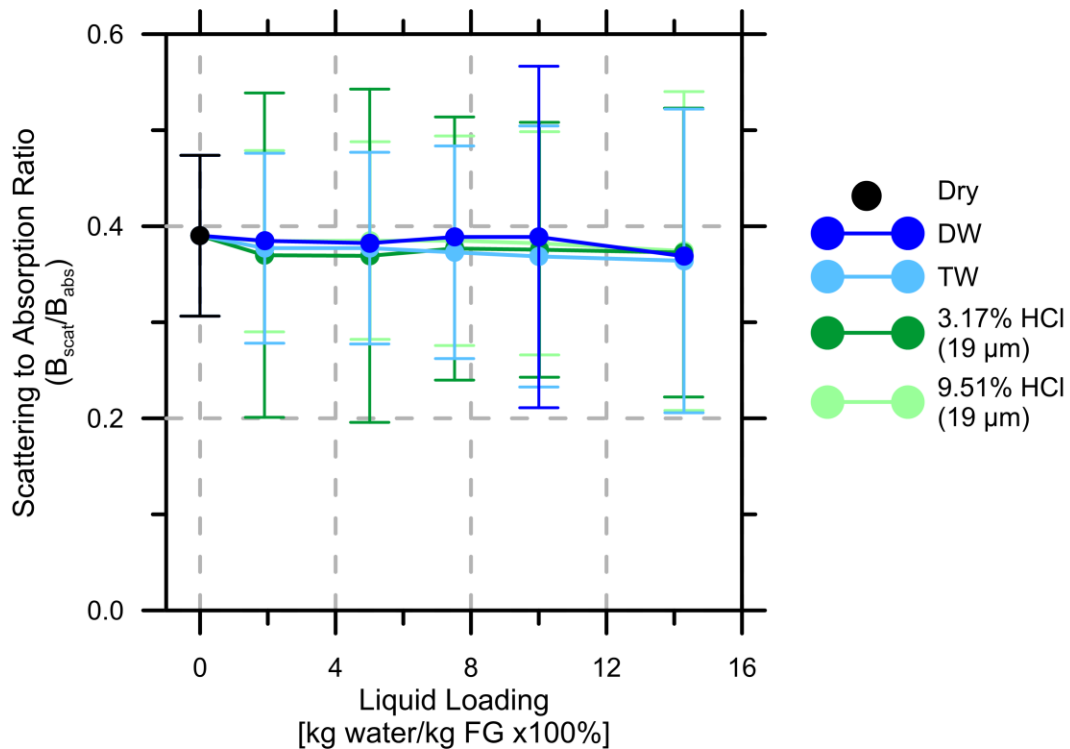


**Figure 4.9:** Measured scattering to absorption coefficient ratios at 405 nm for 19  $\mu\text{m}$  aerosols of DW, TW, 3.17% HCl and 9.51% HCl. Error bars represent total uncertainties, which were directly calculated for the dry flame and the flame with 19  $\mu\text{m}$  aerosols of DW at 10% loading. Plotted uncertainties for other cases were estimated based on the measured precision of a similar case.

Figure 4.10 shows scattering to absorption ratios at 405 nm for flares with injected 5% and 15% NaCl aerosols of nominal 13 and 19  $\mu\text{m}$  droplet size. Unlike results from water and acid tests, a dependency on liquid loading and concentration was observed. Red lines in Figure 4.10 show an increase in the proportion of scattered light with  $B_{scat,\lambda}/B_{abs,\lambda}$  at 405 nm increasing from 0.39 to 0.60 (dry to 14.3% loading). For the 19  $\mu\text{m}$  case only, an increase in the measured ratio was noted at a loading of 7.5% that rose beyond the general trend. While results from some of the repeated tests at 7.5% loading aligned with the general trend, the remaining (non-aligned) tests were also not statistically identified as outliers (see Section 3.2). It is possible that soot properties (as well as absolute values of scattering and absorption coefficients) are highly sensitive to either unidentified and unaccounted for procedural variations. This modest “spike” was seen at all wavelengths

but not during the same test at 13  $\mu\text{m}$  at that same loading (dark purple lines in Figure 4.10). It is thus suspected that the spike was an experimental issue rather than a physical phenomenon, as previous results indicate that droplet size tends to have little effect on emissions of solid and gas-phase species.

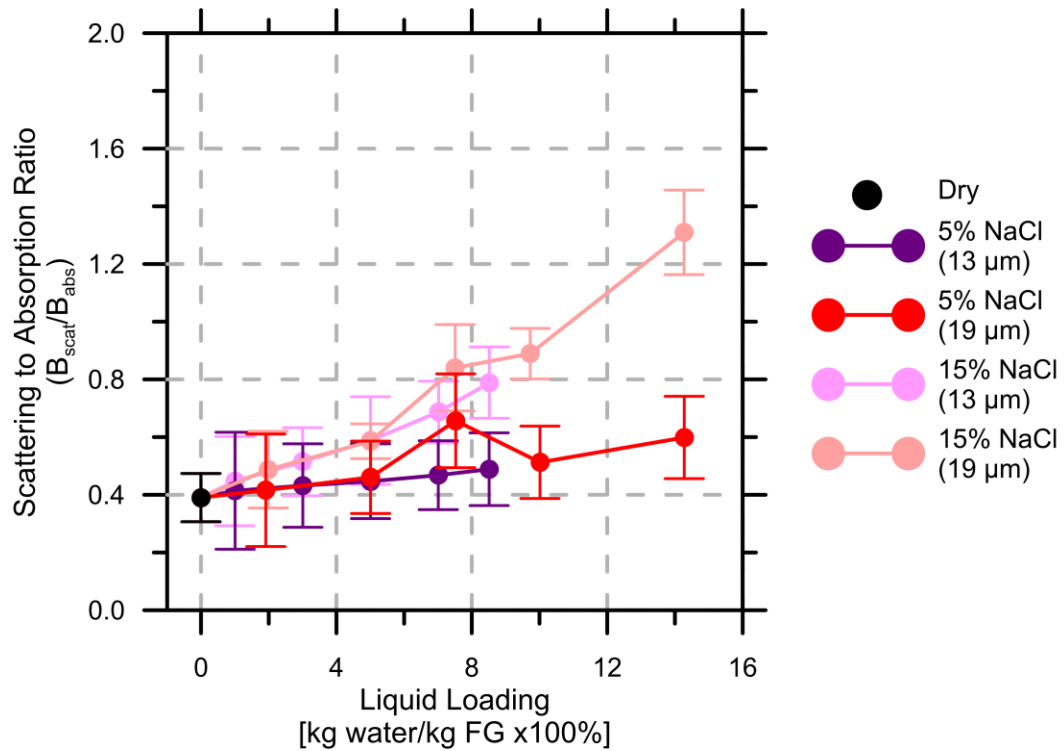


**Figure 4.10: Measured scattering to absorption coefficient ratios at 405 nm for 13 and 19  $\mu\text{m}$  aerosols of 5% and 15% NaCl solutions. Error bars represent total uncertainties, which were directly calculated for the dry flame and the flames with 19  $\mu\text{m}$  aerosols of 5% NaCl at 7.5% loading and 19  $\mu\text{m}$  aerosols of 15% NaCl at all loadings. Plotted uncertainties for other cases were estimated based on the measured precision of a similar case.**

Injected 15% NaCl aerosols induced an even stronger increase in the scattering to absorption ratio, from 0.39 to 1.31 (dry to 14.3% loading) at 405 nm. It is possible emitted stand-alone NaCl particles could be causing the increase in scattering readings as NaCl is a well-known scattering material (Li et al., 2015; Randles et al., 2004). Kazemimanesh (2014) performed preliminary measurements at the CLSF facility in which 7.8% salt aerosol were injected into turbulent diffusion flames. Based on particle mobility diameter

measurements of the emitted particulate, it was suggested that the fraction of stand-alone NaCl particles in the emitted particulate increased as the salt aerosol loading was increased from 2% to 7.8%<sup>8</sup>, eventually comprising the majority of the emitted particles. However, in the present case, the measured absorption coefficient readings also increased with increased loading of salt aerosols (though not to the same extent as scattering coefficients), which implies increases in other types of particles with stronger absorption characteristics.

Figure 4.11 compares the soot yields calculated from either the measured soot volume fraction given by the LII or the absorption coefficient given by the PASS-3 at 405 nm. Data for dry, water, and acid tests are plotted. Appendix E has similar plots derived from PASS-3 data at 532 nm and 870 nm. Soot yields were calculated following the methodology detailed in Corbin and Johnson (2014) as shown in Equation (1.3).

$$Y_{soot} = f_v \left( \frac{R_u T_{sample}}{P_{sample}} \right) \dot{n}_{plume} \rho_C \quad (4.1)$$

where  $Y_{soot}$  is the soot yield;  $f_v$  is the soot volume fraction in the duct,  $R_u$  is the universal ideal gas constant,  $T_{sample}$  and  $P_{sample}$  are the temperature and pressure of the gas at the sample point respectively,  $\dot{n}_{plume}$  is the molar flow rate of the duct gas, and  $\rho_C$  is the density of soot (1860 kg/m<sup>3</sup> (Johnson et al., 2013)). The LII instrument directly outputted the soot volume fraction used in Equation (1.1).

The PASS-3 outputted absorption coefficients which, assuming Rayleigh Debye Gans theory for fractal agglomerates, can be converted to soot yield as described by

---

<sup>8</sup> Fuel used contained 85.24% methane, 7.06% ethane, 3.11% propane, 1.44% butane, 1.91% carbon dioxide, and 1.24% nitrogen by volume. The increase in liquid loading was achieved by fixing the mass flow of liquid and reducing the flare gas flow rate from 267.55 SLPM to 30.4 SLPM.

Equation (2.4) (repeated here for clarity) so long as  $E(m)_\lambda$  at the wavelength of concern is known.

$$f_v = \frac{\lambda B_{abs,\lambda}}{6\pi E(m)_\lambda} \quad (2.4)$$

Combining Equation (2.1) and (1.1) reveals that  $Y_{soot}$  measured by the PASS-3 instrument is inversely proportional to  $E(m)_\lambda$ . Thus, soot yields from the PASS-3 could be scaled to match those calculated from the LII, which allowed an effective  $E(m)_\lambda$  at each wavelength to be estimated. In other words,  $E(m)_\lambda$  in Equation (1.1) was optimized to produce 1:1 fit between the PASS-3 results with the LII soot yields, which implied that  $E(m)_\lambda$  was 0.19 at 405 nm, 0.26 at 532 nm, and 0.22 at 870 nm. This is significant in that it suggests that soot particles created in a flare with injected water and HCl have optical properties similar to those found in literature for dry flame soot (Johnson et al., 2013). Although Kazemimanesh (2014) qualitatively suggested that from a limited set of (four to six) TEM images that soot morphology could vary between dry, water, and HCl (1%<sub>m</sub>) tests, the results of Figure 4.11 strongly suggest otherwise: i.e., particulate matter optical properties appear to be unaffected by the introduction of distilled water and HCl to the flame at 14.3% loading.

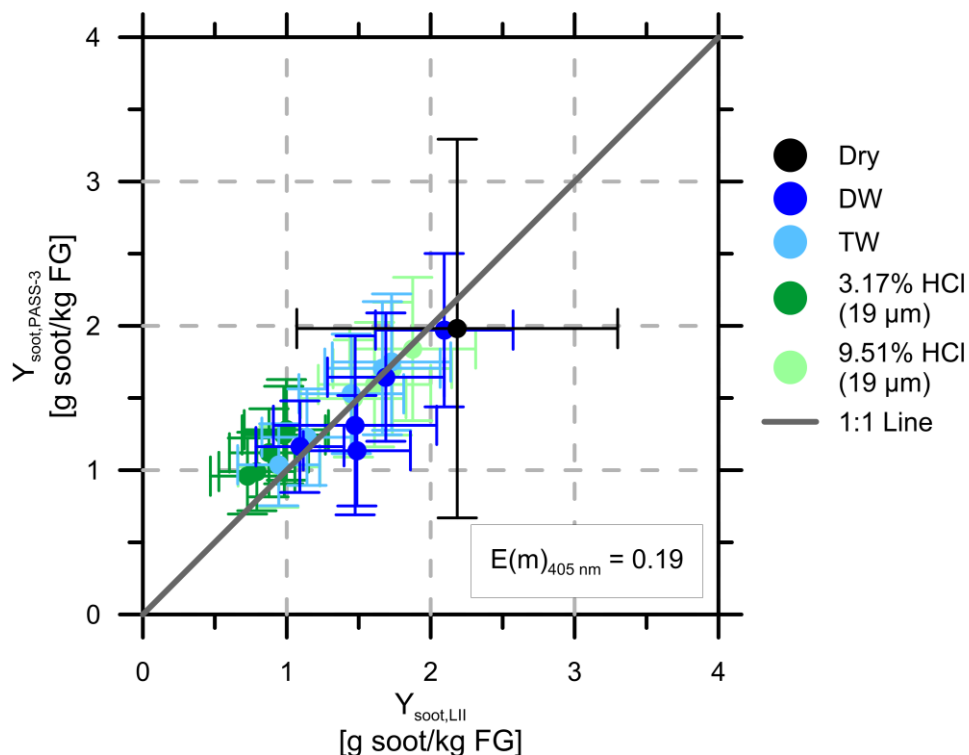


**Figure 4.11: Comparison of soot yields derived from PASS-3 measurements at 405 nm and LII measurements. Results are shown for the dry flame and for flames injected with 19  $\mu\text{m}$  aerosols of DW, TW, and 3.17% and 9.51% HCl solutions. An effective  $E(m)_\lambda$  value was estimated by scaling the soot yields derived from the PASS-3 measurements to match those derived from the LII measurements. Error bars represent total uncertainties, which were directly calculated for the dry flame and the flame with 19  $\mu\text{m}$  aerosols of DW at 10% loading and dry flames. Plotted uncertainties for other cases were estimated based on the measured precision of a similar case.**

Figure 4.12 compares LII and PASS-3 (405 nm) at derived soot yields for dry and 5% and 15% NaCl cases. Appendix E shows similar plots using PASS-3 data at 532 nm and 870 nm. Soot yields for the PASS-3 data were calculated using the optimized  $E(m)_\lambda$  value determined for the dry, water, and acid cases as described above. Compared to Figure 4.11, Figure 4.12 shows no clear correlation between the LII and PASS-3 data when salts are injected into the flame. Soot yields predicted based on the PASS-3 absorption readings were significantly higher than those predicted by the LII. As discussed, it is suspected that salt injection results in an increase in total particulate matter. However, the lack of correlation between the LII and PASS-3 readings suggests that the forms of the particulate matter emitted by the dry flames and NaCl flames are inherently different. In principal,

the LII instrument should be insensitive to NaCl aerosols as the particles do not absorb at the excitation wavelengths of 532 and 1064 nm (Lundgren et al., 2013; Li, 1982). Similarly, since pure NaCl particles are strong scatterers and very weak absorbers at the measurement wavelengths<sup>9</sup>, the perceived increase in soot yield with the PASS-3 (which is based on the measured absorption per Equation (2.2)) is not readily explained by the direct emission of NaCl (Lundgren et al., 2013). Instead, these results could suggest that the effective  $E(m)_\lambda$  value for the emitted particulate is changing with NaCl injection, where changing  $E(m)_\lambda$  affects the LII and PASS-3 instruments differently. In turn, this is an indication that the internal structure of the emitted particulate may be changed when NaCl is introduced into the flame rather than (or in addition to) any direct emission of pure NaCl particles.

Figure 4.12 also implies that the disagreement between the LII and PASS-3 readings is larger as the NaCl concentration in the injected aerosols is increased. Aerosols of 15% NaCl solution show higher perceived soot yields (higher absorption) from the PASS-3 than aerosols of 5% NaCl. However, the LII readings for 5% and 15% solutions were approximately equal. This suggests that the magnitude of inferred changes in the particle structure is sensitive to the NaCl loading.

---

<sup>9</sup> Single scattering albedo (i.e. scattering coefficient over extinction coefficient) of NaCl aerosols is greater than 0.998 in the 250-1530 nm range (Lundgren et al., 2013).

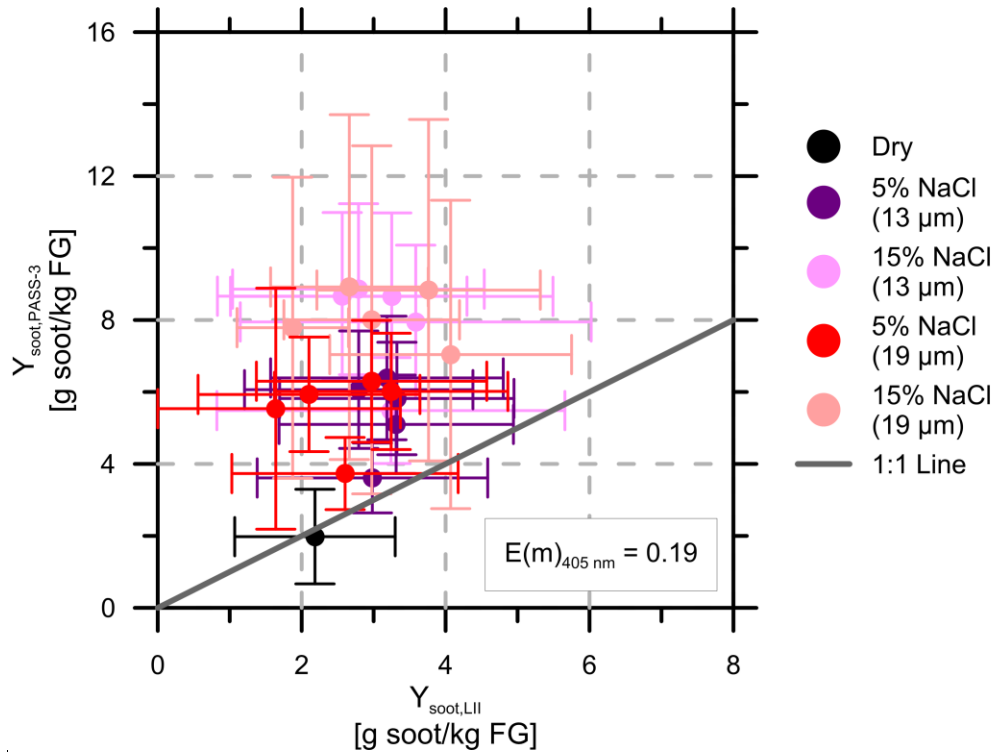


**Figure 4.12: Perceived soot yields from the LII measurements versus the PASS-3 measurements at 405 nm from flames with injected 13 and 19  $\mu\text{m}$  aerosols of 5% and 15% NaCl solutions. Error bars represent total uncertainties, which were directly calculated for the 19  $\mu\text{m}$  aerosols of 5% NaCl at 7.5% loading and 19  $\mu\text{m}$  aerosols of 15% NaCl at all loadings. Plotted uncertainties for other cases were estimated based on the measured precision of a similar case.**

Without extractive sampling, or detailed optical property knowledge of any PM created, it is difficult to draw quantitative conclusions about the form of the emitted particulate. However, the results from the experiments conducted for this thesis strongly suggest that entrained aerosols can affect flare performance and demonstrate the need for further investigation into potential alterations in flare emissions that might occur if flowback fluids are entrained into the flare stream.

# Chapter 5

## Conclusions and Recommendations

Gas- and particulate-phase emissions from a lab-scale flare with injected aerosols were measured. The effect on emissions by varying liquid loading level, liquid type, and droplet size were investigated. Tested aerosol compositions included distilled water, tap water, HCl solutions (3.17% and 9.51% by mass), and aqueous NaCl solutions (5% and 15% by mass). These aerosols were generated via ultrasonic atomization resulting in nominal median droplet sizes of 13  $\mu\text{m}$  or 19  $\mu\text{m}$ . To isolate for potential effects of chlorine on flare emissions, concentrations of Cl in the acid solutions were matched to those of the salt solutions.

CO yields with injected DW or TW aerosols decreased slightly and by similar amounts as the loading increased. Changes in CO yields with injected acid solutions were similarly modest, however the trends were more complex and appeared to be influenced by opposing effects from water (decreases CO yield) and chlorine (increases CO yield). By contrast, injection of aqueous salts strongly increased CO emissions. Injected 5% NaCl solutions caused a sharp increase in the CO yield up to 5% loading, before the trend levelled out at an approximately 7 $\times$  increase in the CO yield over the dry case at the maximum loading of 14.3%. Injected 15% NaCl solutions induced a monotonic increase in CO emissions up to 25 $\times$  the yield of the dry case at the maximum liquid loading of 14.3%. Additional experiments showed that the CO yield trends were identical when the nominal injected droplet diameter was changed from 13  $\mu\text{m}$  to 19  $\mu\text{m}$ .

NO<sub>x</sub> yield decreased slightly with injection of 13 μm and 19 μm nominal diameter aerosols of DW, TW, and 3.17% or 9.51% HCl, though changes over the range of liquid loading were within estimated total uncertainty bounds. NaCl solutions showed a stronger decreasing trend, with NO<sub>x</sub> yields dropping by 25% at the maximum liquid loading.

Methane yield remained negligible for dry, DW, TW, and acid tests. Small quantities of methane were detected with salt experiments, reaching approximately 0.25 g/kg FG with 5% NaCl, and 1.8 g/kg FG with 15% NaCl. As for the CO and NO<sub>x</sub> yields, droplet size appeared to have no effect on methane yield.

The differences in gas-phase emissions between tests of corresponding salt-acid pairs with matched Cl loading (i.e. 5% NaCl and 3.17% HCl; 15% NaCl and 9.51% HCl) suggested that the mode of chlorine injection was a significant factor in how it affected emissions (e.g. where for HCl injection, H ions also entered the flame) and/or that sodium was the dominant species influencing the change in emissions from dry or water base cases.

Light scattering and absorption coefficients of the emitted particulate were also measured. Injected water and acid solutions induced similarly weak dependencies of scattering and absorption on liquid loadings within the range tested. It was especially interesting that measured scattering to absorption ratios for the water and acid solutions at all loadings were approximately equal to the dry case results within experimental uncertainties. Additionally, estimated soot yields from either LII readings and absorption measurements aligned well in all cases for these solutions. This indicates that neither water nor HCl influenced the measurable optical properties (scattering, absorption, and  $E(m)_\lambda$ ) of the emitted particulate matter at the tested concentrations and loadings

Like the gaseous phase products, particulate-phase emissions were much more strongly affected by injected salt solutions than by injected water or acid solutions. In contrast to the water and acid tests, scattering and absorption with injected salt solutions increased with liquid loading. The effect was also stronger for the higher concentration (15%) NaCl solution. Contrary to results with water and acid, scattering to absorption ratios calculated for salt tests were markedly different that of the dry flame, and the difference increased with liquid loading. Comparing LII and light absorption measurements indicated that there are likely absorbing particles that are not detected by the LII and/or that the structure and absorption characteristics of the emitted particulate (i.e.  $E(m)_\lambda$ ) were changed by injection of NaCl solutions into the flame. This would suggest that beyond possible direct emission of highly-scattering NaCl particles, internally mixed soot-NaCl particulate or other modified carbon based particles were being created.

## 5.1 Future Recommendations

Based on the results of this thesis, several suggestions for further work are recommended. Though it is clear that aqueous NaCl aerosols in flames had a significant effect on gas- and particulate-phase combustion emissions, the results from the present experiments are inconclusive in determining the primary influence of these alterations. Introducing other sources of chlorine and sodium (such as hydrogen chloride or Cl in the gas phase) would help isolate the species responsible for the observed large effects on CO yield and particulate matter quantity and characteristics.

The observed changes in light scattering to absorption ratios and the divergence with LII readings indicate a need to examine the emitted particulate composition. An

elemental carbon/organic carbon analyzer (EC/OC) was recently acquired which will permit measurement of the carbonaceous components in emitted particulate. Combined with LII and PASS-3 readings, this will aid in creating a clearer understanding of the effects of NaCl on particulate emissions. Additionally, extractive sampling procedures with TEM or SEM images, as conducted in Kazemimanesh (2014), are being developed for future experiments.

Considering the lack of repeatability with some tests discussed in Chapter 3.2 a new aerosol injection system may need to be devised to eliminate these issues. Future tests will include more repeated experiments to fully account for any precision uncertainties.

Chlorinated combustion systems are known to create polychlorinated dibenzo-*p*-dioxins and furans (PCDD/F) as well as polychlorinated biphenyl (PCBs) (Stanmore, 2004). These highly toxic, carcinogenic, and bio-accumulating species are created in specific temperature ranges, with and without certain catalysts, and via solid- or gas-phase pathways. Extractive sampling for these compounds would greatly benefit the experiments, further enabling thorough comprehension of the potential effects of non-hydrocarbon liquid aerosols on combustion emissions from flares.

# References

- AER, (2006). Directive 058: Oilfield waste management requirements for the upstream petroleum industry. Calgary, AB, Alberta Energy Regulator (AER). Available at: <http://www.ercb.ca/directives/Directive058.pdf>
- AER, (2012). Directive 059: Well Drilling and Completion Data Filing Requirements (Released: December 19, 2012). Calgary, AB, Alberta Energy Regulator (AER). Available at: <https://www.aer.ca/rules-and-regulations/directives/directive-059>
- AER, (2016a). ST60B: Upstream Petroleum Industry Flaring and Venting Report Industry Performance for Year Ending December 31, 2014. ST-60B-2015, Calgary, AB, Alberta Energy Regulator (AER). Available at: <http://aer.ca/documents/sts/ST60B-2015.pdf>
- AER, (2016b). Directive 060: Upstream Petroleum Industry Flaring, Incinerating, and Venting. Calgary, AB. Available at: <http://www.aer.ca/rules-and-regulations/directives/directive-060>
- Allen, D.T. and Torres, V.M., (2011). TCEQ 2010 Flare Study Final Report. PGA No. 582-8-862-45-FY09-04, Austin, TX, Texas Commission on Environmental Quality (TCEQ). Available at: [http://www.tceq.texas.gov/assets/public/implementation/air/rules/Flare/2010flares\\_tudy/2010-flare-study-final-report.pdf](http://www.tceq.texas.gov/assets/public/implementation/air/rules/Flare/2010flares_tudy/2010-flare-study-final-report.pdf)
- Alley, B., Beebe, A., Rodgers, J., and Castle, J.W., (2011). Chemical and physical characterization of produced waters from conventional and unconventional fossil fuel resources. *Chemosphere*. 85:74–82.
- ANSI/ASME, (1985). ANSI/ASME PTC 19.1 - Part 1 – Measurement Uncertainty, Instruments and Apparatus. New York, NY, United States. Available at: [http://gost-snip.su/download/asme\\_ptc\\_19\\_12005\\_test\\_uncertainty](http://gost-snip.su/download/asme_ptc_19_12005_test_uncertainty)
- API, (2012). API Standard 521 - Guide for Pressure-Relieving and Depressuring Systems (Interpretation Request).
- Arthur, J.D., Bohm, B., and Layne, M., (2008). *Hydraulic Fracturing Considerations for Natural Gas Wells of the Marcellus Shale*. In The Ground Water Protection Council 2008 Annual Forum. The Ground Water Protection Council, pp.1–17.
- Arthur, J.D., Langhus, B.G., and Patel, C., (2005). Technical Summary of Oil & Gas Produced Water Treatment Technologies. Tulsa, OK, ALL Consulting, LLC.
- Atreya, A., Crompton, T., and Suh, J., (2000). A Study Of The Chemical And Physical Mechanisms Of Fire Suppression By Water. *Fire Saf. Sci.* 6:493–504.

- Balashov, V.N., Engelder, T., Gu, X., Fantle, M.S., and Brantley, S.L., (2015). A model describing flowback chemistry changes with time after Marcellus Shale hydraulic fracturing. *Am. Assoc. Pet. Geol. Bull.* 99:143–154.
- Barbot, E., Vidic, N.S., Gregory, K.B., and Vidic, R.D., (2013). Spatial and temporal correlation of water quality parameters of produced waters from devonian-age shale following hydraulic fracturing. *Environ. Sci. Technol.* 47:2562–2569.
- BC Oil & Gas Commission, (2015). Industry bulletin - Electronic Submission of Hydraulic Fracture Data. Available at: <https://www.bcogc.ca/node/8257/download>
- BC Oil & Gas Commission, (2016). Flaring and Venting Reduction Guideline. Available at: <http://www.bcogc.ca/node/5916/download>
- BC Oil and Gas Commission, (2010). Oil and Gas Waste Regulation. Available at: [http://www.bclaws.ca/civix/document/id/loo84/loo84/32\\_254\\_2005](http://www.bclaws.ca/civix/document/id/loo84/loo84/32_254_2005)
- Blondes, M.S., Gans, K.D., Rowan, E.L., Thordsen, J.J., Reidy, M.E., Engle, M.A., Kharaka, Y.K., and Thomas, B., (2016). U.S. Geological Survey National Produced Waters Geochemical Database v2.2 (PROVISIONAL). Reston, Virginia. Available at: <http://energy.usgs.gov/EnvironmentalAspects/EnvironmentalAspectsofEnergyProductionandUse/ProducedWaters.aspx#3822349-data>
- Blouquin, R. and Joulin, G., (1998). *On the quenching of premixed flames by water sprays: Influences of radiation and polydispersity*. In Symposium (International) on Combustion. pp.2829–2837.
- BP, (2015). Statistical Review of World Energy 2015. Available at: [bp.com/statisticalreview](http://bp.com/statisticalreview)
- Capo, R.C., Stewart, B.W., Rowan, E.L., Kolesar Kohl, C.A., Wall, A.J., Chapman, E.C., Hammack, R.W., and Schroeder, K.T., (2014). The strontium isotopic evolution of Marcellus Formation produced waters, southwestern Pennsylvania. *Int. J. Coal Geol.* 126:57–63.
- CFR, (2016). 40CFR60.5375 (2016). Available at: <https://www.ecfr.gov/cgi-bin/text-idx?node=sp40.7.60.0000>
- Chang, W.D., Karra, S.B., and Senkan, S.M., (1987). A computational study of chlorine inhibition of CO flames. *Combust. Flame.* 69:113–122.
- Chelliah, H.K., (2007). Flame inhibition/suppression by water mist: Droplet size/surface area, flame structure, and flow residence time effects. *Proc. Combust. Inst.* 31 II:2711–2719.

- Clark, C. and Veil, J., (2015). U.S. Produced water volumes and management practices. Available at: [http://www.circleofblue.org/waternews/wp-content/uploads/2010/09/ANL\\_EVS\\_\\_R09\\_produced\\_water\\_volume\\_report\\_2437.pdf](http://www.circleofblue.org/waternews/wp-content/uploads/2010/09/ANL_EVS__R09_produced_water_volume_report_2437.pdf)
- Coderre, A.R., Thomson, K.A., Snelling, D.R., and Johnson, M.R., (2011). Spectrally-Resolved Light Absorption Properties of Cooled Soot from a Methane Flame. *Appl. Phys. B*. 104:175–188.
- Conrad, B.M. and Johnson, M.R., (2017). Field Measurements of Black Carbon Yields from Gas Flaring. *Environ. Sci. Technol.*. 51:1893–1900.
- Corbin, D.J., (2014). Methodology and Experiments to Determine Soot and NO<sub>x</sub> Yields from a Vertical Lab-Scale Flare Burning Alkane-Mixtures and Ethylene. (*M.A.Sc. Thesis*). Carleton University.
- Corbin, D.J. and Johnson, M.R., (2014). Detailed Expressions and Methodologies for Measuring Flare Combustion Efficiency, Species Emission Rates, and Associated Uncertainties. *Ind. Eng. Chem. Res.*. 53:19359–19369.
- Cowie, B.R., James, B., Nightingale, M., and Mayer, B., (2014). Determination of the stable isotope composition and total dissolved solids of Athabasca oil sands reservoir porewater: Part 2. Characterization of McMurray Formation waters in the Suncor-Firebag field. *Am. Assoc. Pet. Geol. Bull.*. 98:2143–2160.
- Dethlefs, K.M. and Schladert, A.F., (1976). The Effect of Steam on Flame Temperature, Burning Velocity and Carbon Formation in Hydrocarbon Flames. *Combust. Flame*. 27:205–215.
- Dollar, P.S., Frape, S.K., and McNutt, R., (1991). Geochemistry of formation waters, southwestern Ontario, Canada and southern Michigan, USA: Implications for origin and evolution. Open File Report 5743, Ontario Geological Survey. Available at: <http://www.geologyontario.mndmf.gov.on.ca/mndmfiles/pub/data/imaging/OFR5743/OFR5743.pdf>
- Dresel, P.E. and Rose, A.W., (2010). Chemistry and origin of oil and gas well brines in western Pennsylvania. Available at: <http://www.marcellus.psu.edu/resources/PDFs/brines.pdf>
- Elsner, M. and Hoelzer, K., (2016). Quantitative Survey and Structural Classification of Hydraulic Fracturing Chemicals Reported in Unconventional Gas Production. *Environ. Sci. Technol.*. 50:3290–3314.
- Elvidge, C.D., Zhizhin, M., Baugh, K., Hsu, F., and Ghosh, T., (2016). Methods for Global Survey of Natural Gas Flaring from Visible Infrared Imaging Radiometer Suite Data. *Energies*. 9:14.

- Fleming, J.W., Williams, B.A., and Sheinson, R.S., (2002). Suppression Effectiveness of Aerosols: The Effect of Size and Flame Type. Washington, D.C. Available at: [http://www.nist.gov/manuscript-publication-search.cfm?pub\\_id=909166](http://www.nist.gov/manuscript-publication-search.cfm?pub_id=909166)
- FracFocus, (2011). FracFocus is Live. <http://fracfocus.org/node/27> (accessed January 27, 2016)
- FracFocus, (2012). BC Oil & Gas Commission Creates Canadian FracFocus Website. <http://fracfocus.ca/node/333> (accessed January 26, 2016)
- Fuss, S.P., Chen, E.F., Yang, W., Kee, R.J., Williams, B.A., and Fleming, J.W., (2002). *Inhibition of Premixed Methane/Air Flames By Water Mist*. In Proceedings of Combustion Institute. Combustion and Flame, pp.361–368.
- Gallegos, T.J. and Varela, B.A., (2015a). Data Regarding Hydraulic Fracturing Distributions and Treatment Fluids, Additives, Proppants, and Water Volumes Applied to Wells Drilled in the United States from 1947 through 2010. Reston, Virginia, United States Geological Survey. Available at: <https://pubs.usgs.gov/ds/0868/pdf/ds868.pdf>
- Gallegos, T.J. and Varela, B.A., (2015b). Trends in Hydraulic Fracturing Distributions and Treatment Fluids, Additives, Proppants, and Water Volumes Applied to Wells Drilled in the United States from 1947 through 2010— Data Analysis and Comparison to the Literature. 2014–5131, United States Geological Survey. Available at: <https://pubs.er.usgs.gov/publication/sir20145131>
- Gandossi, L., (2013). An overview of hydraulic fracturing and other formation stimulation technologies for shale gas production. EUR 26347 EN, European Commisison Joint Research Center Technical Reports. Available at: <https://www.google.ca/url?sa=t&rct=j&q=&esrc=s&source=web&cd=1&cad=rja&uact=8&ved=0ahUKEwjboVcCmtnTAhVK64MKHaHaAi0QFggqMAA&url=http%3A%2F%2Fpublications.jrc.ec.europa.eu%2Frepository%2Fbitstream%2F1111111%2F30129%2F1%2Fan%2520overview%2520of%2520hydraul>
- Gokulakrishnan, P. and Lawrence, A.D., (1998). An Experimental Study of the Inhibiting Effect of Chlorine in a Fluidized Bed Combustor. *Combust. Flame*. 652:640–652.
- Government of Saskatchewan, (2015a). Directive S-10: Saskatchewan Upstream Petroleum Industry Associated Gas Conservation Directive Record of Change. Saskatchewan Ministry of Energy and Resources. Available at: [https://www.google.ca/url?sa=t&rct=j&q=&esrc=s&source=web&cd=1&cad=rja&uact=8&ved=0ahUKEwjfgb-HI9nTAhVp6IMKHQ4\\_BiMQFggjMAA&url=http%3A%2F%2Fwww.publications.gov.sk.ca%2Fredirect.cfm%3Fp%3D76076%26i%3D85153&usg=AFQjCNGKiYJzJWqcQOWY2nAcozj8jTHAjQ&sig2=sS2pc](https://www.google.ca/url?sa=t&rct=j&q=&esrc=s&source=web&cd=1&cad=rja&uact=8&ved=0ahUKEwjfgb-HI9nTAhVp6IMKHQ4_BiMQFggjMAA&url=http%3A%2F%2Fwww.publications.gov.sk.ca%2Fredirect.cfm%3Fp%3D76076%26i%3D85153&usg=AFQjCNGKiYJzJWqcQOWY2nAcozj8jTHAjQ&sig2=sS2pc) [March 1, 2017]
- Government of Saskatchewan, (2015b). Directive S-20: Saskatchewan Upstream Flaring and Incineration. Regina, SK, Saskatchewan Ministry of Energy and Resources.

Available at:

[https://www.google.ca/url?sa=t&rct=j&q=&esrc=s&source=web&cd=1&cad=rja&uact=8&ved=0ahUKEwjPpN\\_9ltnTAhUW24MKHX0CDa4QFggnMAA&url=http%253A%252F%252Fpublications.gov.sk.ca%252Fdocuments%252F310%252F85154-Directive%252520S-20%252520%252520Saskatchewan%252520Upstream%252520Flaring%25](https://www.google.ca/url?sa=t&rct=j&q=&esrc=s&source=web&cd=1&cad=rja&uact=8&ved=0ahUKEwjPpN_9ltnTAhUW24MKHX0CDa4QFggnMAA&url=http%253A%252F%252Fpublications.gov.sk.ca%252Fdocuments%252F310%252F85154-Directive%252520S-20%252520%252520Saskatchewan%252520Upstream%252520Flaring%25)

Grahame, T.J., Klemm, R., and Schlesinger, R.B., (2014). Public health and components of particulate matter: The changing assessment of black carbon. *J. Air Waste Manage. Assoc.* 64:620–660.

Gregory, K.B., (2010). Water Management Associated with Hydraulic Fracturing. *Elements*. 7:181–186.

Grubbs, F.E., (1950). Sample Criteria for Testing Outlying Observations. *Ann. Math. Stat.* 21:27–58.

Guo, H., Liu, F., Smallwood, G.J., and Gülder, Ö.L., (2016). The flame preheating effect on numerical modelling of soot formation in a two-dimensional laminar ethylene-air diffusion flame.

Haghshenas, A. and Nasr-El-Din, H.A., (2014). Effect of dissolved solids on reuse of produced water at high temperature in hydraulic fracturing jobs. *J. Nat. Gas Sci. Eng.* 21:316–325.

Haluszczak, L.O., Rose, A.W., and Kump, L.R., (2013). Geochemical evaluation of flowback brine from Marcellus gas wells in Pennsylvania, USA. *Appl. Geochemistry*. 28:55–61.

Harper, J., (2008). The Marcellus Shale—An Old “New” Gas Reservoir in Pennsylvania. *Pennsylvania Geol.* 38:2–13.

Hayes, T., (2009). Sampling and Analysis of Water Streams Associated with the Development of Marcellus Shale Gas.

Hobbs, M., Frape, S., Shouakar-Stash, O., and Kennell, L., (2011). Regional Hydrogeochemistry—Southern Ontario. NWMO DGR-TR-2011-12, Nuclear Waste Management Organization. Available at: [http://www.opg.com/generating-power/nuclear/nuclear-waste-management/Deep-Geologic-Repository/Documents/GSR/4.1.2\\_Regional-Hydrogeochemistry---Southern-Ontario.pdf](http://www.opg.com/generating-power/nuclear/nuclear-waste-management/Deep-Geologic-Repository/Documents/GSR/4.1.2_Regional-Hydrogeochemistry---Southern-Ontario.pdf)

Hua Yang, M., Hamins, A., and Puril, I.K., (1994). The Structure of inhibited Counterflowing Nonpremixed Flames. *Combust. Flame*. 98:107–122.

IHS, PIDM - Petroleum Information Data Model.

<https://www.ihs.com/products/petroleum-information-data-model-pidm.html>

- Johnson, M.R. and Coderre, A.R., (2012). Compositions and greenhouse gas emission factors of flared and vented gas in the western Canadian sedimentary basin. *J. Air Waste Manage. Assoc.* 62:992–1002.
- Johnson, M.R., Devillers, R.W., and Thomson, K.A., (2013). A Generalized Sky-LOSA Method to Quantify Soot/Black Carbon Emission Rates in Atmospheric Plumes of Gas Flares. *Aerosol Sci. Technol.* 47:1017–1029.
- Johnson, M.R. and Tyner, D.R., (2015). Analysis of Reported Operational Phase Emissions from Hydraulically Fractured Gas Wells in Alberta. Technical Report Prepared for Environment Canada (K8A42-14-0015), Carleton University, Ottawa, Canada.
- Kazemimanesh, M., (2014). Effects of Non-hydrocarbon Liquids on Particulate Emissions of Flares. University of Alberta.
- Kazemimanesh, M., Kostiuk, L.W., Johnson, M.R., Fleck, B., and Olfert, J.S., (2012). *Exploratory Investigation of the Effects of Distilled Water, Tap Water, and Salt Water on Flare Particulate Emissions*. In Combustion Institute Canadian Section Spring Technical Meeting. Toronto, ON.
- Kharaka, Y.K. and Hanor, J.S., (2007). *Deep fluids in the continents: Sedimentary basins*. In Treatise on Geochemistry. Amsterdam, Netherlands, Elsevier.
- Köylü, Ü.Ö. and Faeth, G.M., (1996). Spectral extinction coefficients of soot aggregates from turbulent diffusion flames. *J. Heat Transfer*. 118:415–421.
- Lampe, D.J. and Stolz, J.F., (2015). Current perspectives on unconventional shale gas extraction in the Appalachian Basin. *J. Environ. Sci. Health. A. Tox. Hazard. Subst. Environ. Eng.* 50:434–46.
- Lazzarini, A.K., Krauss, R.H., Chelliah, H.K., and Linteris, G.T., (2000). Extinction conditions of non-premixed flames with fine droplets of water and water/NaOH solutions. *Proc. Combust. Inst.* 28:2939–2945.
- Lentati, A.M. and Chelliah, H.K., (1998). Dynamics of Water Droplets in a Counterflow Field and their Effect on Flame Exinction. *Combust. Flame*. 115:158–179.
- Li, H.H., (1982). Refractive index of alkaline earth halides and its wavelength and temperature derivatives. *J. Phys. Chem. Ref. Data*. 9:161–290.
- Li, X., Liu, L., Zhao, J., and Tan, J., (2015). Optical Properties of Sodium Chloride Solution Within the Spectral Range from 300 to 2500 nm at Room Temperature. *Appl. Spectrosc.* 69:635–640.
- Lundgren, K., Vogel, B., Vogel, H., and Kottmeier, C., (2013). Direct radiative effects of sea salt for the Mediterranean region under conditions of low to moderate wind speeds. *J. Geophys. Res. Atmos.* 118:1906–1923.

- Maguire-Boyle, S.J. and Barron, A.R., (2014). Organic compounds in produced waters from shale gas wells. *Environ. Sci. Process. Impacts*. 16:2237–2248.
- Martini, A.M., Walter, L.M., Budat, J.M., Ku, T.C.W., Kaiser, C.J., and Schoell, M., (1998). Genetic and temporal relations between formation waters and biogenic methane: Upper Devonian Antrim shale, Michigan Basin, USA. *Geochim. Cosmochim. Acta*. 62:1699–1720.
- McElreath, D., (2011). *Comparison of Hydraulic Fracturing Fluids Composition with Produced Formation Water following Fracturing – Implications for Fate and Transport*. In Proceedings of the Technical Workshops for the Hydraulic Fracturing Study: Fate and Transport. Arlington, VA, U.S. Environmental Protection Agency (US EPA).
- McEwen, J.D.N. and Johnson, M.R., (2012). Black Carbon Particulate Matter Emission Factors for Buoyancy Driven Associated Gas Flares. *J. Air Waste Manage. Assoc.* 62:307–321.
- McIntosh, J.C. and Walter, L.M., (2005). Volumetrically significant recharge of Pleistocene glacial meltwaters into epicratonic basins: Constraints imposed by solute mass balances. *Chem. Geol.* 222:292–309.
- McIntosh, J.C., Walter, L.M., and Martini, A.M., (2002). Pleistocene recharge to midcontinent basins: Effects on salinity structure and microbial gas generation. *Geochim. Cosmochim. Acta*. 66:1681–1700.
- Michel, M.M., Reczek, L., Granops, M., Rudnicki, P., and Piech, A., (2015). Pretreatment and desalination of flowback water from the hydraulic fracturing. *Desalin. Water Treat.* 57:1–10.
- Miller, J.A. and Bowman, C.T., (1989). Mechanism and Modeling of Nitrogen Chemistry in Combustion. *Progress Energy Combust. Sci.* 15:287–338.
- Modak, A.U., Abbud-Madrid, A., Delplanque, J.P., and Kee, R.J., (2006). The effect of mono-dispersed water mist on the suppression of laminar premixed hydrogen-, methane-, and propane-air flames. *Combust. Flame*. 144:103–111.
- Morgan, W.L. and Rosocha, L.A., (2012). The physics and plasma chemistry of an RF needle in a saltwater aerosol. *IEEE Trans. Plasma Sci.* 40:3174–3184.
- NEB, (2017a). Marketable Natural Gas Production in Canada. National Energy Board (NEB). Available at: <https://www.neb-one.gc.ca/nrg/sttstc/ntrlgs/stt/mrktblntrlgsprdctn-eng.html>
- NEB, (2017b). 2016 Estimated Production of Canadian Crude Oil and Equivalent. National Energy Board (NEB). Available at: <https://www.neb-one.gc.ca/nrg/sttstc/crdlndptrlmprdct/stt/stmtdprdctn-eng.html>

- Nevers, N. De, (1995). *Air Pollution Control Engineering* P. H. King, ed. McGraw-Hill.
- Osborn, S.G. and McIntosh, J.C., (2010). Chemical and isotopic tracers of the contribution of microbial gas in Devonian organic-rich shales and reservoir sandstones, northern Appalachian Basin. *Appl. Geochemistry*. 25:456–471.
- Prasad, K., Li, C., and Kailasanath, K., (1998). Optimizing water-mist injection characteristics for suppression of coflow diffusion flames. *Symp. Combust.* 27:2847–2855.
- Randles, C.A., Russell, L.M., and Ramaswamy, V., (2004). Hygroscopic and optical properties of organic sea salt aerosol and consequences for climate forcing. *Geophys. Res. Lett.* 31:1–4.
- Sakurai, I., Suzuki, J., Kotani, Y., Naito, H., and Yoshida, A., (2013). Extinguishment of propane/air co-flowing diffusion flames by fine water droplets. *Proc. Combust. Inst.* 34:2727–2734.
- Stanmore, B., (2004). The formation of dioxins in combustion systems. *Combust. Flame*. 136:398–427.
- Steliga, T., Kluk, D., and Jakubowicz, P., (2015). Analysis of chemical and toxicological properties of fluids for shale hydraulic fracturing and flowback water. *Polish J. Environ. Stud.* 24:2185–2196.
- Torres, V.M., Herndon, S.C., and Allen, D.T., (2012). Industrial Flare Performance at Low Flow Conditions. 2. Steam- and Air-Assisted Flares. *Ind. Eng. Chem. Res.* 51:12569–12576.
- Turns, S.R., (2012). *An Introduction to Combustion: Concepts and Applications* 3rd ed. USA, McGraw-Hill.
- Tyner, D.R. and Johnson, M.R., (2014). Emission Factors for Hydraulically Fractured Gas Wells Derived Using Well- and Battery-level Reported Data for Alberta, Canada. *Environ. Sci. Technol.* 48:14772–14781.
- U.S. EIA, (2016a). Natural Gas Vented and Flared (Summary).  
[https://www.eia.gov/dnav/ng/ng\\_sum\\_lsum\\_a\\_EPG0\\_vgv\\_mmc\\_f\\_a.htm](https://www.eia.gov/dnav/ng/ng_sum_lsum_a_EPG0_vgv_mmc_f_a.htm) (accessed September 5, 2016)
- U.S. EIA, (2016b). U.S. Field Production of Crude Oil.  
<https://www.eia.gov/dnav/pet/hist/LeafHandler.ashx?n=PET&s=MCRFPUS1&f=A> (accessed September 5, 2016)
- U.S. EIA, (2016c). Shale in the United States.  
[https://www.eia.gov/energy\\_in\\_brief/article/shale\\_in\\_the\\_united\\_states.cfm#tight\\_oil](https://www.eia.gov/energy_in_brief/article/shale_in_the_united_states.cfm#tight_oil) (accessed September 5, 2016)

- U.S. EPA, (2004). Evaluation of Impacts to Underground Sources of Drinking Water by Hydraulic Fracturing of Coalbed Methane Reservoirs. EPA 816-R-04-003, Washington, D.C., United States Environmental Protection Agency. Available at: [www.epa.gov/safewater/uic/cbmstudy.html](http://www.epa.gov/safewater/uic/cbmstudy.html)
- U.S. EPA, (2015). Analysis of Hydraulic Fracturing Fluid Data from the FracFocus Chemical Disclosure Registry 1.0. Available at: [https://www.google.ca/url?sa=t&rct=j&q=&esrc=s&source=web&cd=1&cad=rja&uact=8&ved=0ahUKEwj68L\\_AldnTAhUn44MKHdb0AgAQFggsMAA&url=https%3A%2F%2Fwww.epa.gov%2Fsites%2Fproduction%2Ffiles%2F2015-03%2Fdocuments%2Ffracfocus\\_analysis\\_report\\_and\\_appendices\\_final\\_03](https://www.google.ca/url?sa=t&rct=j&q=&esrc=s&source=web&cd=1&cad=rja&uact=8&ved=0ahUKEwj68L_AldnTAhUn44MKHdb0AgAQFggsMAA&url=https%3A%2F%2Fwww.epa.gov%2Fsites%2Fproduction%2Ffiles%2F2015-03%2Fdocuments%2Ffracfocus_analysis_report_and_appendices_final_03)
- U.S. House of Representatives, (2011). Chemicals Used in Hydraulic Fracturing. Available at: [http://democrats.energycommerce.house.gov/sites/default/files/documents/Hydraulic Fracturing Report 4.18.11.pdf](http://democrats.energycommerce.house.gov/sites/default/files/documents/Hydraulic%20Fracturing%20Report%204.18.11.pdf)
- URS Corporation, (2011). Water Related Issues Associated with Gas Production in The Marcellus Shale. Fort Washington, PA, US, New York State Energy Research and Development Authority. Available at: <https://www.google.ca/url?sa=t&rct=j&q=&esrc=s&source=web&cd=1&cad=rja&uact=8&ved=0ahUKEwjN86nvlNnTAhUpxYMKHTj2Dt4QFgg5MAA&url=https%3A%2F%2Fwww.nyserda.ny.gov%2F%2Fmedia%2FFiles%2FPublications%2FPSPSER%2FNYSERDA%2Fng%2FURS-Report-2011-Mar.pdf&usg=AFQjCNH>
- Vengosh, A., Jackson, R.B., Warner, N., Darrah, T.H., and Kondash, A., (2014). A Critical Review of the Risks to Water Resources from Unconventional Shale Gas Development and Hydraulic Fracturing in the United States. *Environ. Sci. Technol.* 48:8334–8348.
- Vidic, R.D., Brantley, S.L., Vandenbossche, J.M., Yoxtheimer, D., and Abad, J.D., (2013). Impact of shale gas development on regional water quality. *Science* (80-). 340:826–835.
- Wang, J. and Anthony, E.J., (2009). CO oxidation and the inhibition effects of halogen species in fluidised bed combustion. *Combust. Theory Model.* 13:105–119.
- Warner, N.R., Darrah, T.H., Jackson, R.B., Millot, R., Kloppmann, W., and Vengosh, A., (2014). New tracers identify hydraulic fracturing fluids and accidental releases from oil and gas operations - SI. *Environ. Sci. Technol.* 48:12552–12560.
- Wasylshen, R. and Fulton, S., (2012). Reuse of Flowback & Produced Water for Hydraulic Fracturing in Tight Oil. Petroleum Technology Alliance of Canada (PTAC). Available at: <http://www.ptac.org/projects/151>
- Wei, X., Wang, Y., Liu, D., and Sheng, H., (2009). Influence of HCl on CO and NO emissions in combustion. *Fuel*. 88:1998–2003.

- Whitten, B.L., Morgan, W.L., and Bardsley, J.N., (1982). Monte-Carlo calculations of two-and three-body ionic recombination. *J. Phys. B At. Mol. Phys.* 15:319–326.
- Worden, R.H., (1996). Controls on Halogen Concentrations in Sedimentary Formation Waters. *Mineral. Mag.*. 60:259–274.
- Wu, D., Wang, Y., Wei, X., Li, S., and Guo, X., (2016). Experimental investigation and numerical simulation of CO oxidation with HCl addition. *Fuel.* 179:221–228.
- Xu, Y., Adefidipe, O.A., and Dehghanpour, H., (2015). Estimating fracture volume using flowback data from the Horn River Basin: A material balance approach. *J. Nat. Gas Sci. Eng.*. 25:253–270.
- Yang, W. and Kee, R.J., (2002). The effect of monodispersed water mists on the structure, burning velocity, and extinction behavior of freely propagating, stoichiometric, premixed, methane-air flames. *Combust. Flame.* 130:322–335.
- Yoshida, A., Kashiwa, K., Hashizume, S., and Naito, H., (2015). Inhibition of counterflow methane/air diffusion flame by water mist with varying mist diameter. *Fire Saf. J.*. 71:217–225.
- Zhou, H., Meng, A., Long, Y., Li, Q., and Zhang, Y., (2015). A review of dioxin-related substances during municipal solid waste incineration. *Waste Manag.*. 36:106–18.
- Ziemkiewicz, P.F. and Thomas, H.Y., (2015). Evolution of water chemistry during Marcellus Shale gas development: A case study in West Virginia. *Chemosphere.* 134:224–31.

# Appendix A

## Machine Drawings of the Atomizing Burner

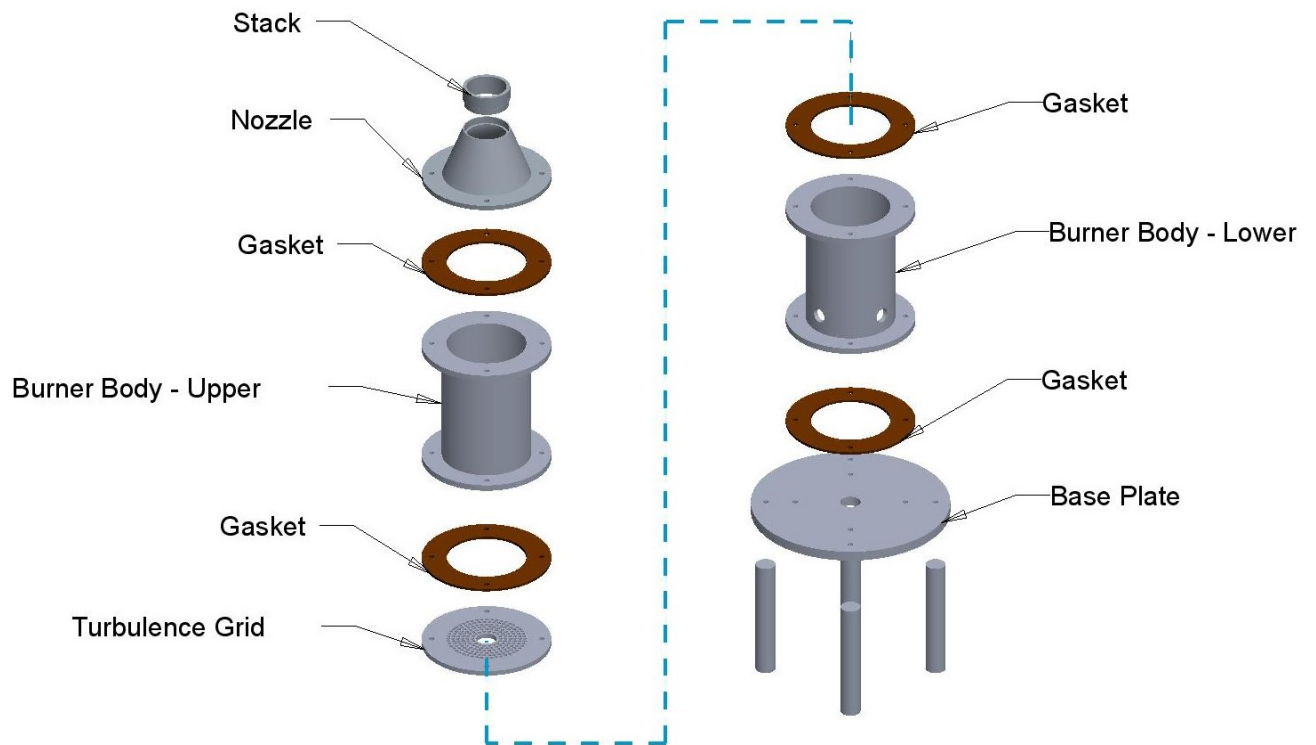


Figure A.1: Assembly drawing of atomizing burner

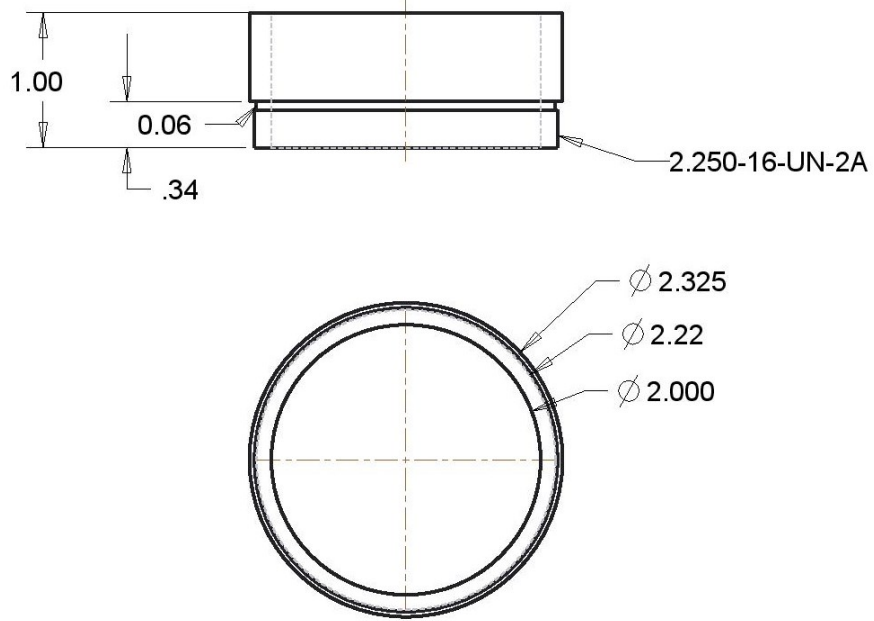


Figure A.2: Machine drawing of 1" high stack for 2" diameter burner (Units in inches).

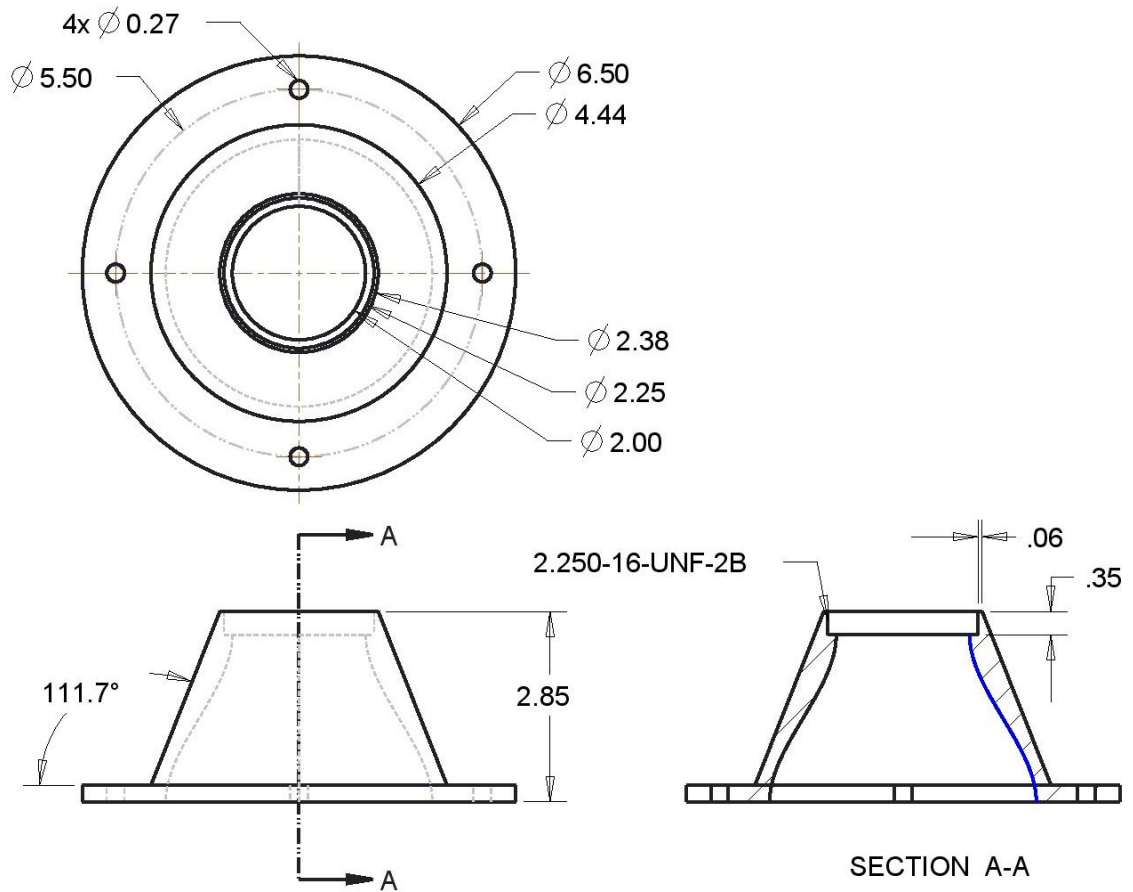


Figure A.3: Machine drawing of 2" exit diameter burner (Units in inches).

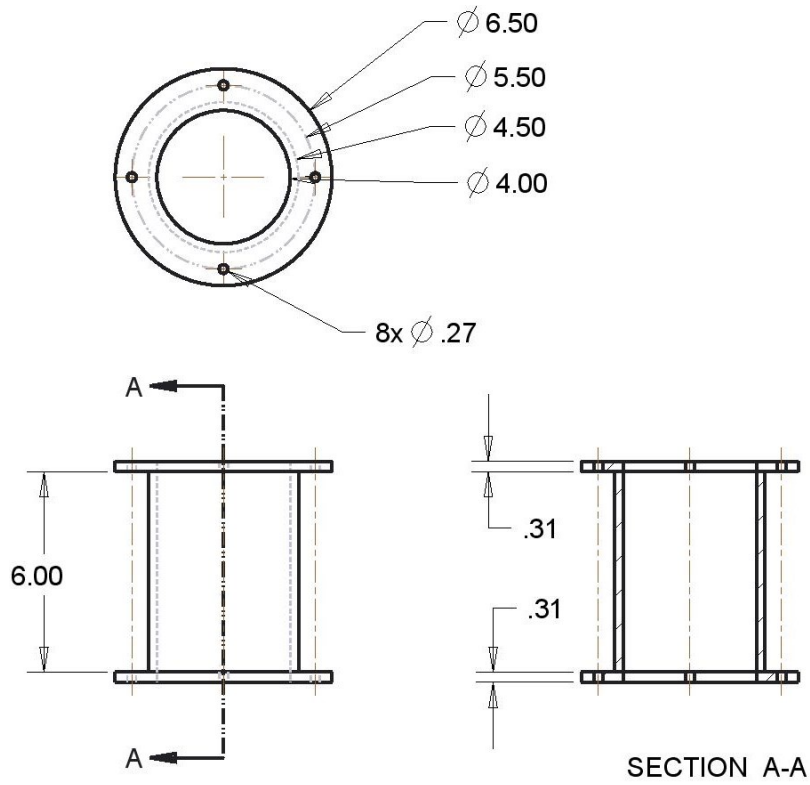


Figure A.4: Machine drawing of the top of the burner body (Units in inches)

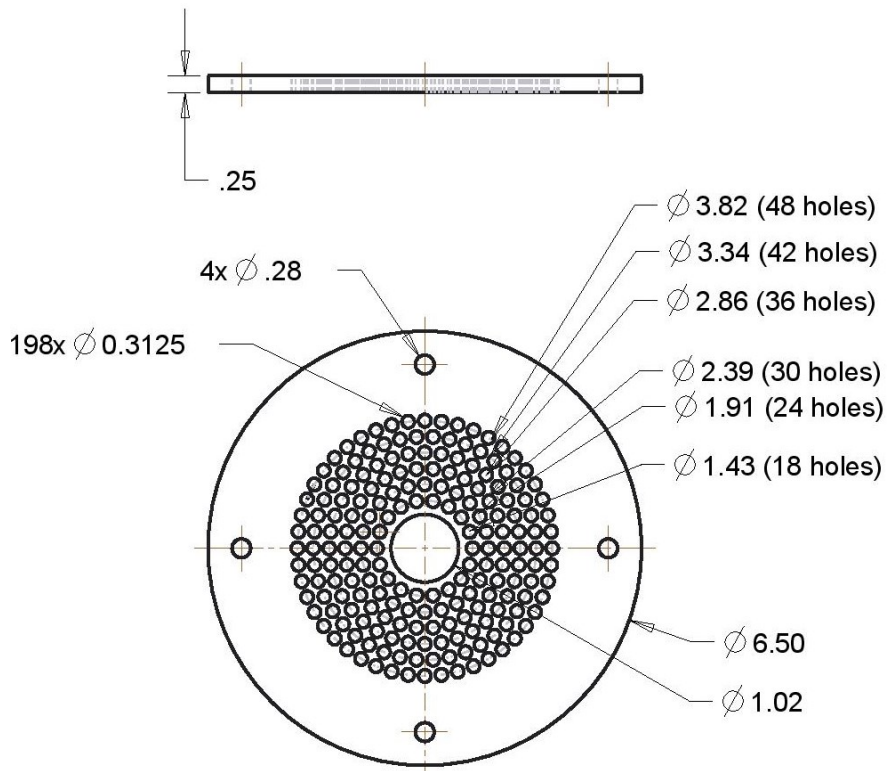


Figure A.5: Machine drawing of turbulence grid (Units in inches)

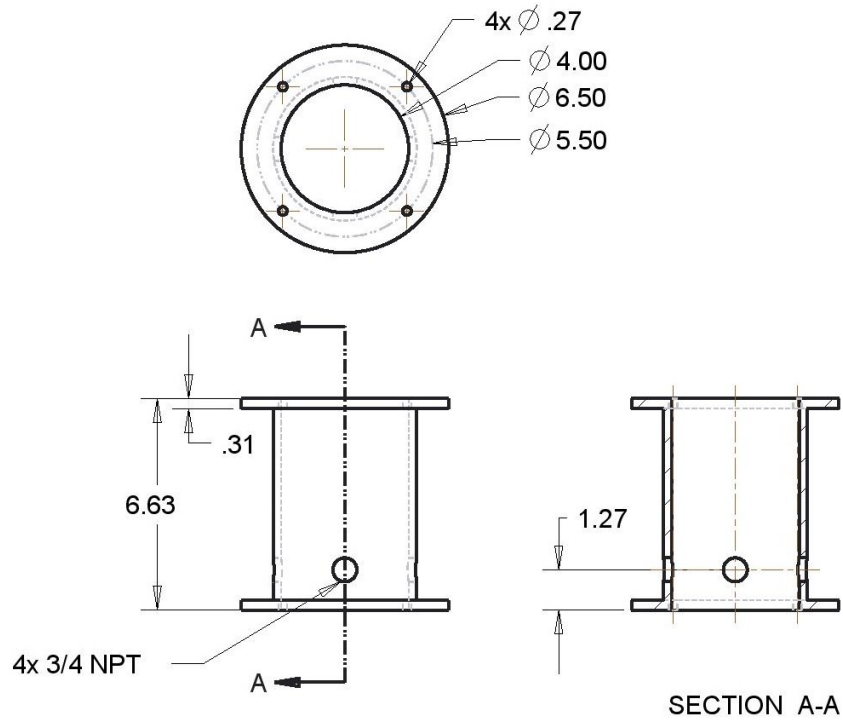


Figure A.6: Drawing of burner body bottom with four 1/2" NPT fuel inlet ports (Units in inches)

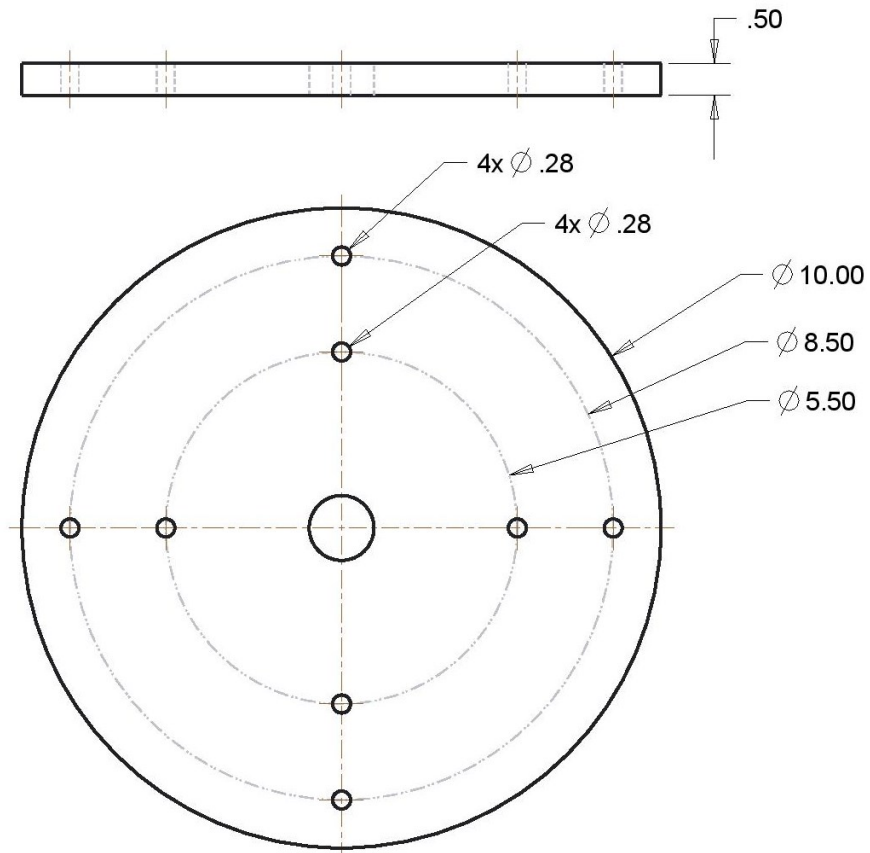
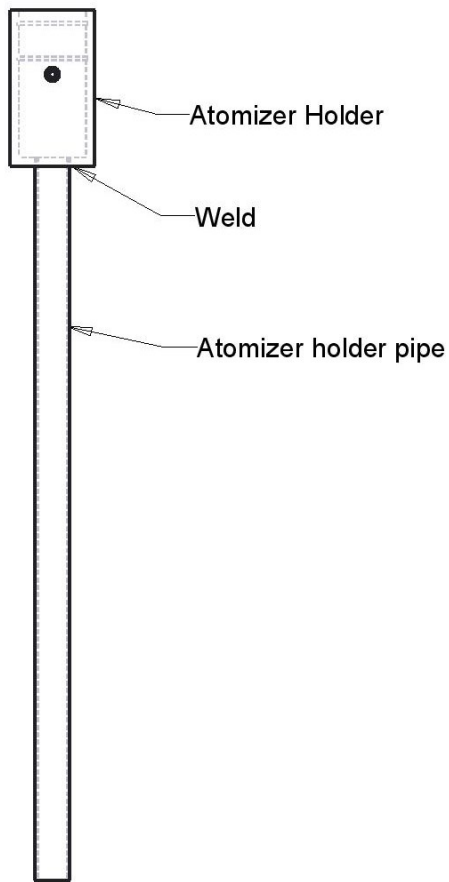


Figure A.7: Burner base plate with liquid injection port in centre (Units in inches)



**Figure A.8: Example assembly of atomizer holder**

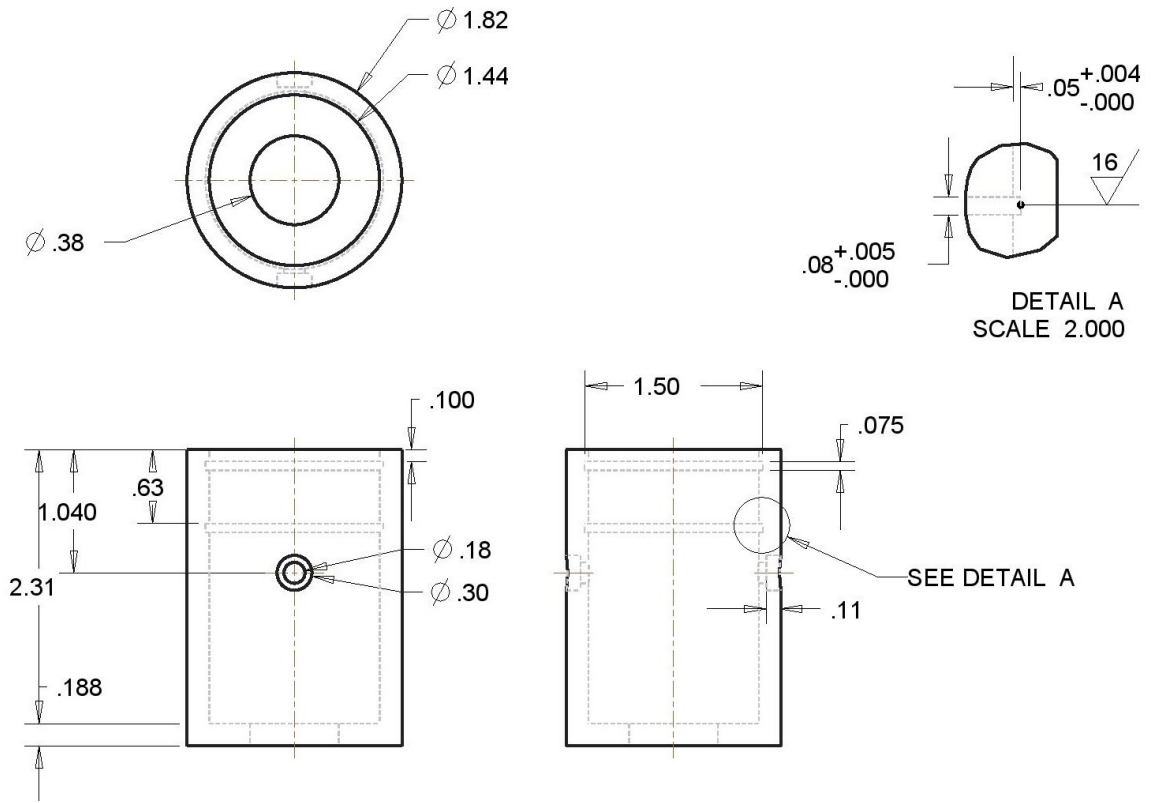


Figure A.9: Machine drawing for 120 kHz nozzle holder (Units in inches)

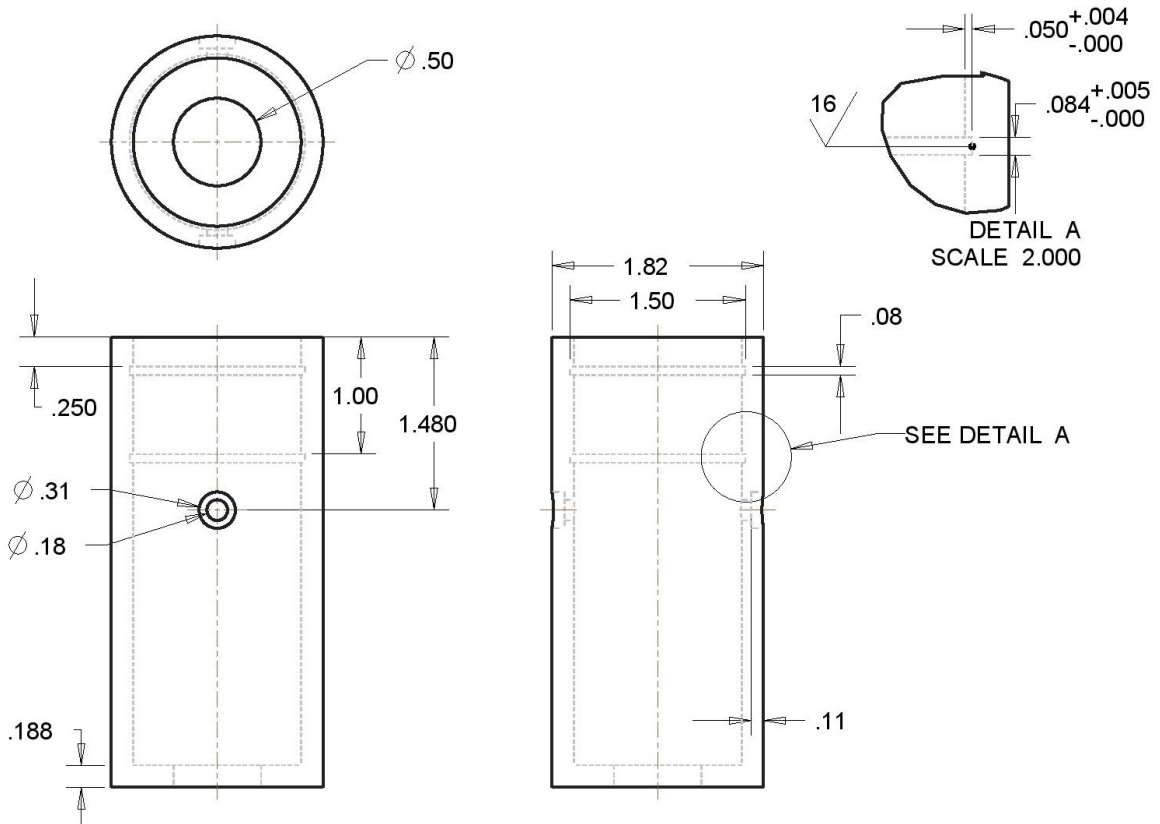
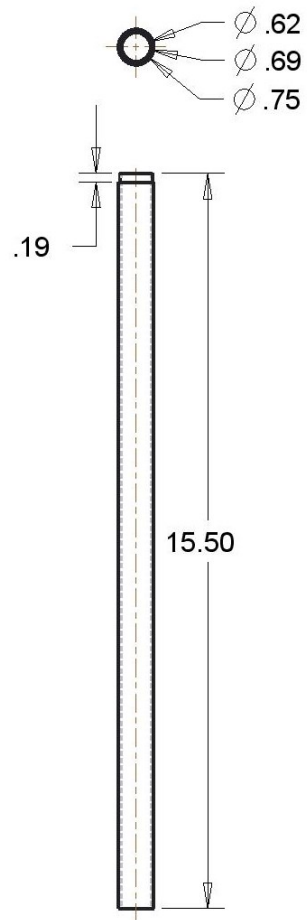


Figure A.10: Machine drawing of 180 kHz nozzle holder (Units in inches)



**Figure A.11: Nozzle holder stem (Units in inches)**

# Appendix B

## Calibration Procedure for Absorption and Scattering Coefficients

The calibration procedure of the PASS-3 instrument is based on the ability of the instrument to measure scattering ( $B_{scat,\lambda}$ ), absorption ( $B_{abs,\lambda}$ ), and extinction ( $B_{ext,\lambda}$ ) coefficients independently where:

$$B_{ext,\lambda} = B_{scat,\lambda} + B_{abs,\lambda} \quad (\text{B.1})$$

Extinction coefficient (at all three measurement wavelengths) can be directly measured following Beer's law in the form of Equation (2.2) (copied again here for clarity):

$$B_{ext,\lambda} = \frac{-1}{L} \ln\left(\frac{I_\lambda}{I_{0,\lambda}}\right) \cdot 10^6 \quad (\text{2.2})$$

where  $I$  is the laser power measured after passing through a particulate laden sample,  $I_0$  is the laser power measured when particulate is filtered out of the sample, and  $L$  is the path length of the laser (i.e. the length of the cell, 0.2486 m in this case). Given a linear detector response, this measurement requires no separate calibration.

Data for the scattering calibration were collected by sampling strongly-scattering particles (polystyrene latex, PSL, spheres) suspended in air. Because light absorption by the PSL particles was negligible,  $B_{abs,\lambda}$  could be removed from Equation (B.1), which simplified to Equation (B.2).

$$B_{ext,\lambda} = B_{scat,\lambda} \quad (\text{B.2})$$

The PASS-3 instruments internal measurement of  $B_{ext,\lambda}$  could then be used to calibrate the measurement of  $B_{scat,\lambda}$ . The particle-laden air was created with a nebulizer provided by DMT (M/N: PAG). The PSL spheres used for scattering calibration were of nominal diameter  $269 \pm 5$  nm (NIST traceable, Thermo Fisher Scientific M/N: 09980027) and were initially suspended in liquid water. The nebulized PSL spheres-liquid and air mixture was directed through a diffusion drier filled with desiccant (McMaster-Carr M/N: 2181K97). Figure B.1 shows the flow path of the nebulizer and the delivery of the PSL spheres to the PASS-3.

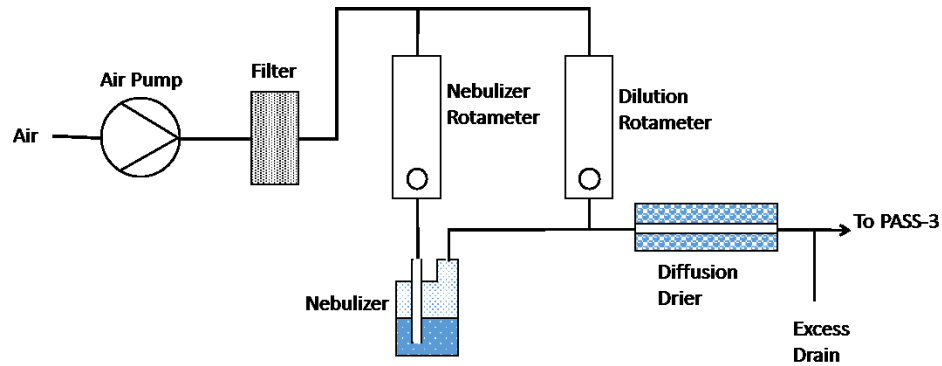


**Figure B.1: DMT nebulizer flow diagram. The nebulizer is used to deliver dry, PSL-laden air to the PASS-3.**

Manufacturer instructions suggested that during calibration of  $B_{scat,\lambda}$ , an extinction measurement ( $B_{ext,\lambda}$ ) could be found by taking a laser power reading of filtered air ( $I_0$ ) and un-filtered ( $I$ ) for 2-4 minutes each. However, during initial testing and calibration of the PASS-3, the drift in the measured laser powers over the suggested interval was found to be non-negligible. Further experimentation revealed this issue could be eliminated by measuring  $I_0$  immediately before and after a measurement of the  $I$ , and fitting the data to obtain a more accurate reference  $I_0$  value. Figure B.2 shows sample data obtained via this

procedure in which a 40 second measurement of an PSL laden sample (black) was preceded and followed by a measurement of a particle-free (filtered) sample (red). A linear least squares regression was applied to the  $I_0$  and  $I$  readings (red and black lines respectively in Figure B.2) to account for and laser drift during the calibration. The crosses on the fit lines indicate the corresponding values used to calculate  $B_{ext,\lambda}$  for the scattering calibration. It should be noted that the scattering and absorption coefficient readings were stable throughout this process as the instrument internally could account for laser fluctuations and drift.

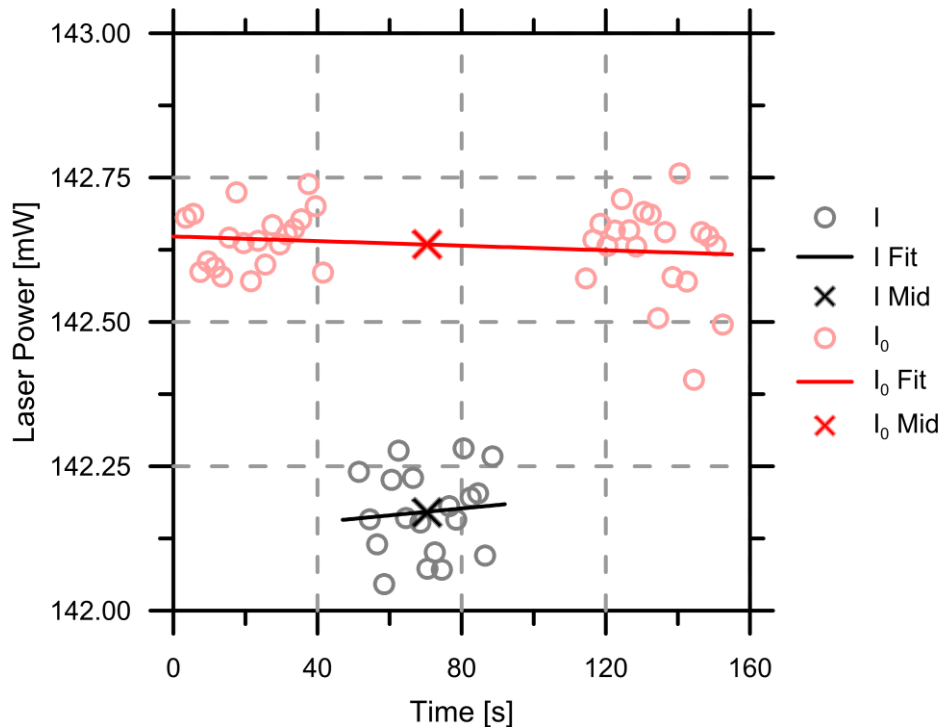


**Figure B.2: Example data from PASS-3 calibration. Pre- and post-zero laser power readings represent  $I_0$  (red circles) and the laser power reading during sampling with PSL or soot represent  $I$  (black circles). The X marks represented the  $I_0$  and  $I$  signal at the midpoint of the filtered and non-filtered linear fit and are used in the attenuation calculation.**

Uncertainties on  $I$  and  $I_0$  mid-time laser power estimates along the fit were calculated via a 99% confidence interval of the chosen mid-point. Total uncertainties on  $B_{ext,\lambda}$  were subsequently found by standard uncertainty propagation methodology outlined

by the American National Standards Institute (ANSI) and the American Society of Mechanical Engineers (ASME). Partial derivatives of  $B_{ext,\lambda}$  as calculated by Equation (2.2) with respect to each variable (in this case  $I$  and  $I_0$ ) were solved for and multiplied by the uncertainties of the pertinent variable. The final values (two in this case) were added in quadrature.

This procedure was repeated at varying scattering and attenuation coefficients by changing the PSL sphere concentration in the aqueous mixture, or the dilution air stream. Once 20-30 data points were collected, a MATLAB code was used to parse and process the laser power and scattering coefficient data. The code offered the option to remove any points that appear erroneous. Points were only removed if it was noted that some experimental issue occurred during the calibration (e.g., the pump of the nebulizer stopped in the middle of a reading) or if the scattering reading was lower than the detection limit causing, for example,  $I_0$  to be smaller than  $I$ .

Figure B.3 shows an example of the result of the scattering calibration procedure. The MATLAB code calculated a weighted through-origin linear regression (RTO), the slope of which was the calibration coefficient for the selected wavelength. Each point on Figure B.3 comprised a set of data like that shown in Figure B.2. The coefficients were input into the PASS-3's software by multiplying the current scattering calibration by the "new" calibration.

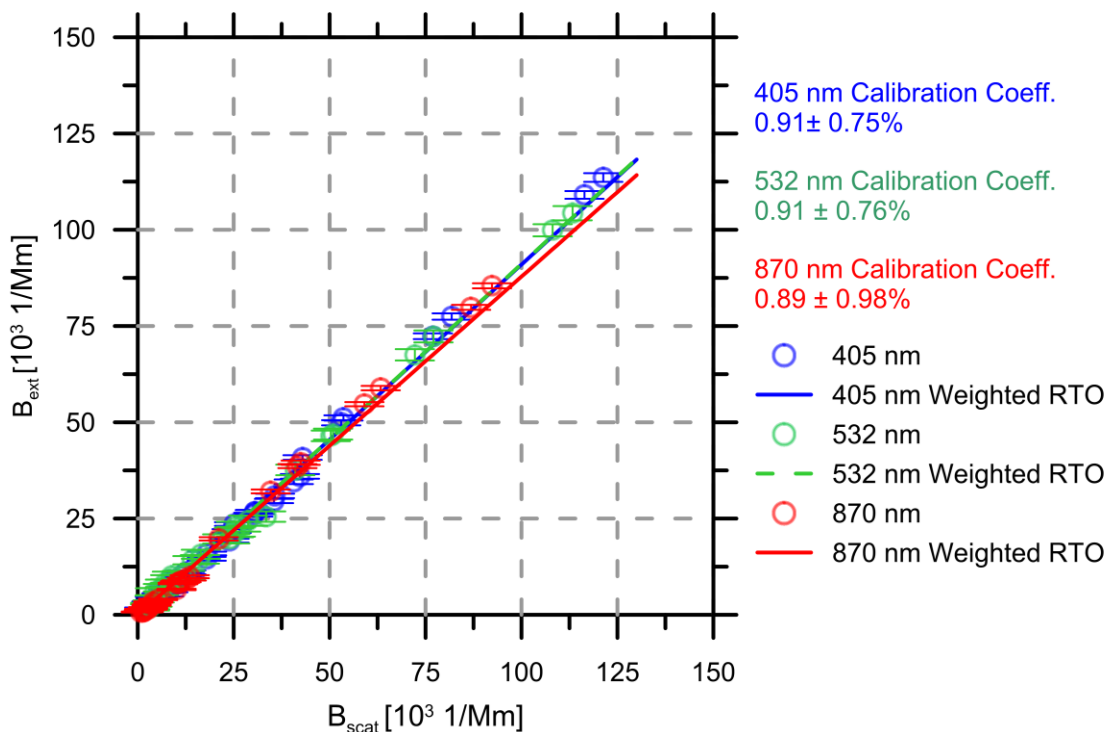


**Figure B.3: Example calibration result. Weighted linear regression through the origin of calibration points.**

The absorption calibration followed a similar procedure to that of the scattering calibration. However, the aerosol source was changed to a highly absorbing material, in this case black carbon or “soot” generated from an inverted burner. The burner was located at the National Research Council’s Measurement Science and Standards Laboratory. A and a flow diagram of the burner is shown in Figure B.4. Soot from the methane flame was diluted with clean compressed air to achieve multiple levels of absorption within the desired range. The methane fuel flow rate was set at 1.381 SLPM and combustion air flow rate was set at 18.85 SLPM (both controlled by Brooks MFCs, M/N: 5851). Primary and secondary dilution air was from two injection diluters (M/N: Dekati DI-1000) each providing an approximate dilution ratio of 1:8. Tertiary dilution was supplied by a 15 SLPM MFC drawn by a vacuum pump. To control the dilution, the MFC was set at 2 SLPM intervals from closed to its maximum flow rate at 15 SLPM. The primary and

secondary diluters were heated and kept a constant temperature of 100°C. When necessary, the secondary diluter was removed to achieve concentrations at the upper limit of the desired calibration range.

Because the scattering coefficient from the soot was not negligible, the (calibrated) scattering readings were subtracted from the calculated  $B_{ext,\lambda}$  values and plotted in the same manner as Figure B.3 (i.e.  $B_{abs,\lambda}$  on the X-axis,  $B_{ext,\lambda} - B_{scat,\lambda}$  on the Y-axis), propagating through the confidence intervals of the scattering coefficients. Figures similar to Figure B.2 and Figure B.3 were output by the MATLAB code. Error propagation included the uncertainties on the scattering coefficients found in the previous step of the calibration procedure. The slope of the fits were the absorption calibration coefficients. This wavelength-specific value was input into the instrument's internal software. The uncertainty of any scattering or absorption coefficient was then input into the flare data processing LabVIEW VI and outputs included absorption and scattering coefficients with their respective absolute uncertainties in 1/Mm.

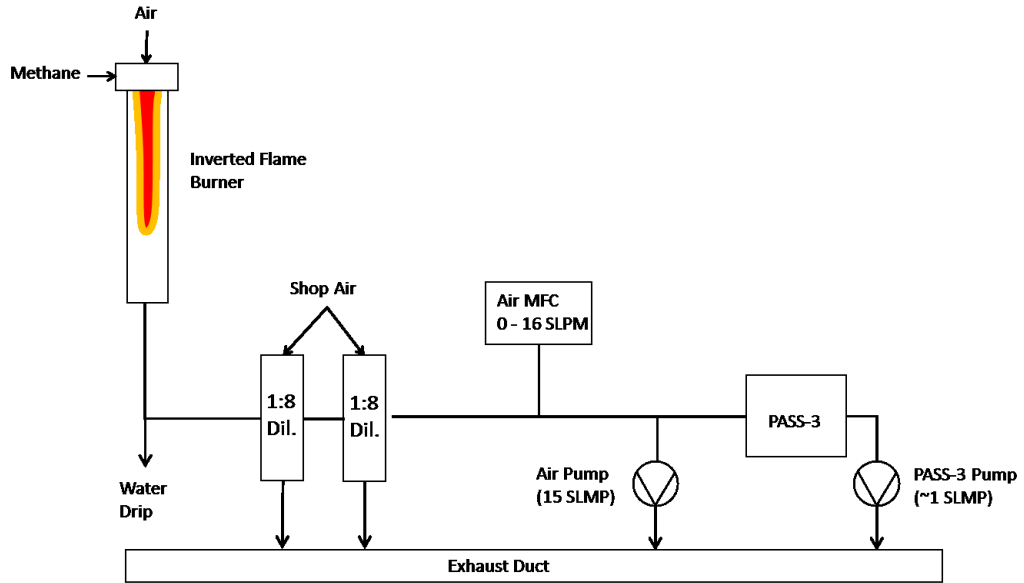


Figure B.4: NRC inverted flame burner and dilution system for delivering absorbing particle source to the PASS-3 for  $B_{abs,\lambda}$  calibration.

# Appendix C

## Tap Water Chemical Composition

**Table C.1: Properties and Anion Analysis Results of Aerosolized Tap Water**

<b>Species</b>	<b>Units</b>	<b>Value</b>	<b>Method MDL</b>
<b>Anion Sum</b>	mg/L	1.33	N/A
<b>Cation Sum</b>	mg/L	1.34	N/A
<b>Bicarb. Alkalinity (calc. as CaCO<sub>3</sub>)</b>	mg/L	29	1
<b>Calculated TDS</b>	mg/L	84	1
<b>Hardness (CaCO<sub>3</sub>)</b>	mg/L	30	1
<b>Conductivity</b>	μS/cm	140	1
<b>Saturation pH (@ 20°C)</b>	N/A	8.95	N/A
<b>Total Ammonia-N</b>	mg/L	0.22	0.05
<b>Dissolved Organic Carbon</b>	mg/L	2.7	0.2
<b>Dissolved Sulphate (SO<sub>4</sub>)</b>	mg/L	27	1
<b>Dissolved Chloride (Cl)</b>	mg/L	6.6	1
<b>Nitrite (N)</b>	mg/L	ND	0.01
<b>Nitrate (N)</b>	mg/L	0.13	0.1

**Table C.2: Dissolved Metal Analysis Results of Aerosolized Tap Water**

<b>Species</b>	<b>Units</b>	<b>Value</b>	<b>Method MDL</b>
<b>Dissolved Aluminum (Al)</b>	$\mu\text{g/L}$	45	5
<b>Dissolved Antimony (Sb)</b>	$\mu\text{g/L}$	ND	0.5
<b>Dissolved Arsenic (As)</b>	$\mu\text{g/L}$	ND	1
<b>Dissolved Barium (Ba)</b>	$\mu\text{g/L}$	14	2
<b>Dissolved Beryllium (Be)</b>	$\mu\text{g/L}$	ND	0.5
<b>Dissolved Boron (B)</b>	$\mu\text{g/L}$	ND	10
<b>Dissolved Cadmium (Cd)</b>	$\mu\text{g/L}$	ND	0.1
<b>Dissolved Calcium (Ca)</b>	$\mu\text{g/L}$	8400	200
<b>Dissolved Chromium (Cr)</b>	$\mu\text{g/L}$	ND	5
<b>Dissolved Cobalt (Co)</b>	$\mu\text{g/L}$	ND	0.5
<b>Dissolved Copper (Cu)</b>	$\mu\text{g/L}$	9.2	1
<b>Dissolved Iron (Fe)</b>	$\mu\text{g/L}$	ND	100
<b>Dissolved Lead (Pb)</b>	$\mu\text{g/L}$	1	0.5
<b>Dissolved Magnesium (Mg)</b>	$\mu\text{g/L}$	2100	50
<b>Dissolved Manganese (Mn)</b>	$\mu\text{g/L}$	ND	2
<b>Dissolved Molybdenum (Mo)</b>	$\mu\text{g/L}$	ND	0.5
<b>Dissolved Nickel (Ni)</b>	$\mu\text{g/L}$	ND	1
<b>Dissolved Phosphorus (P)</b>	$\mu\text{g/L}$	ND	100
<b>Dissolved Potassium (K)</b>	$\mu\text{g/L}$	730	200
<b>Dissolved Selenium (Se)</b>	$\mu\text{g/L}$	ND	2
<b>Dissolved Silicon (Si)</b>	$\mu\text{g/L}$	2200	50
<b>Dissolved Silver (Ag)</b>	$\mu\text{g/L}$	ND	0.1
<b>Dissolved Sodium (Na)</b>	$\mu\text{g/L}$	16000	100
<b>Dissolved Strontium (Sr)</b>	$\mu\text{g/L}$	41	1
<b>Dissolved Thallium (Tl)</b>	$\mu\text{g/L}$	ND	0.05
<b>Dissolved Titanium (Ti)</b>	$\mu\text{g/L}$	ND	5
<b>Dissolved Uranium (U)</b>	$\mu\text{g/L}$	ND	0.1
<b>Dissolved Vanadium (V)</b>	$\mu\text{g/L}$	ND	0.5
<b>Dissolved Zinc (Zn)</b>	$\mu\text{g/L}$	ND	5

# Appendix D

## Repeatability Tests

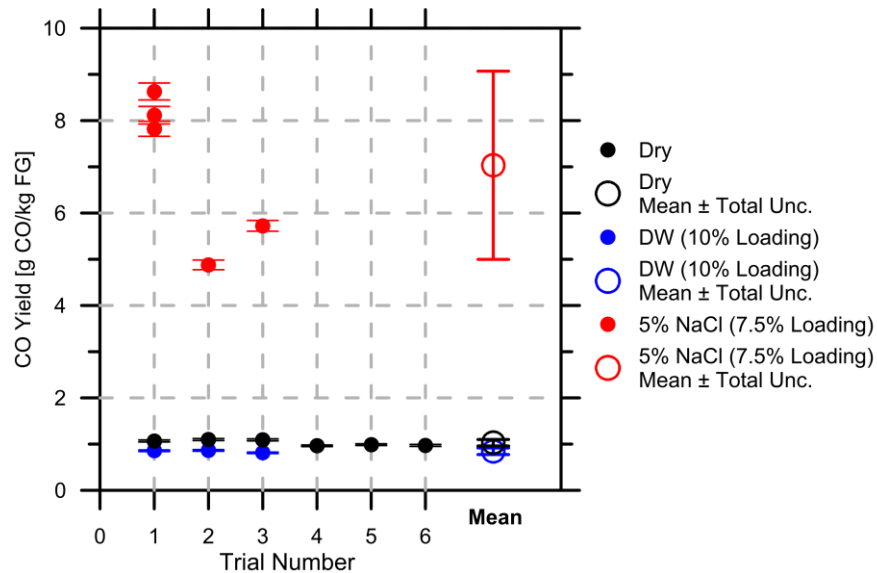


**Figure D.1: CO yield of Heavy 4 flare gas at 109.45 SLPM at dry conditions and versus liquid loading of 19  $\mu\text{m}$  of DW and 5% aqueous NaCl. Instrument bias errors are included on each individual data point. Open circles represent the average of the repeated trials at each liquid loading set point. Error bars on the closed circles are instrument bias and error bars on the open circles are the calculated total uncertainty of the average excluding any outliers.**

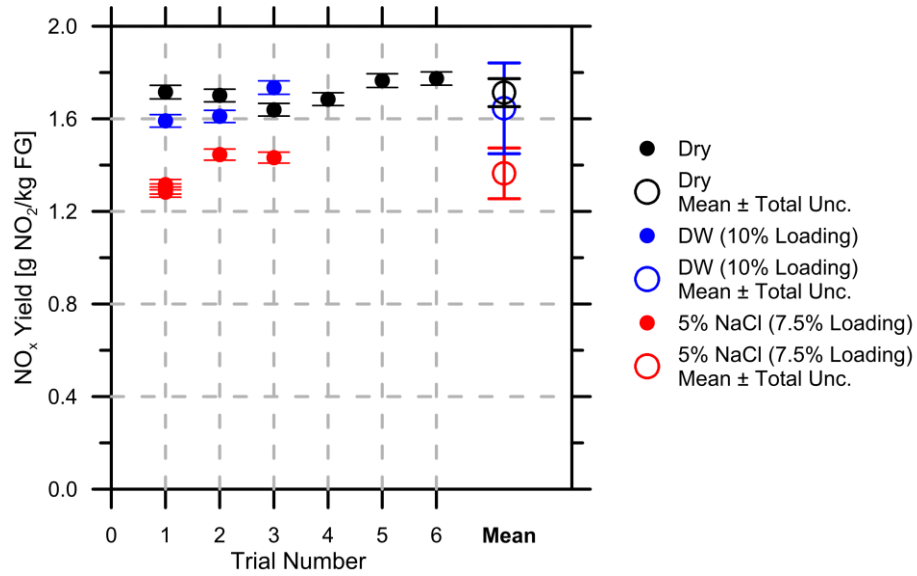


**Figure D.2: NO<sub>x</sub> yield of Heavy 4 flare gas at 109.45 SLPM at dry conditions and versus liquid loading of 19 μm of DW and 5% aqueous NaCl. Instrument bias errors are included on each individual data point. Open circles represent the average of the repeated trials at each liquid loading set point. Error bars on the closed circles are instrument bias and error bars on the open circles are the calculated total uncertainty of the average excluding any outliers.**

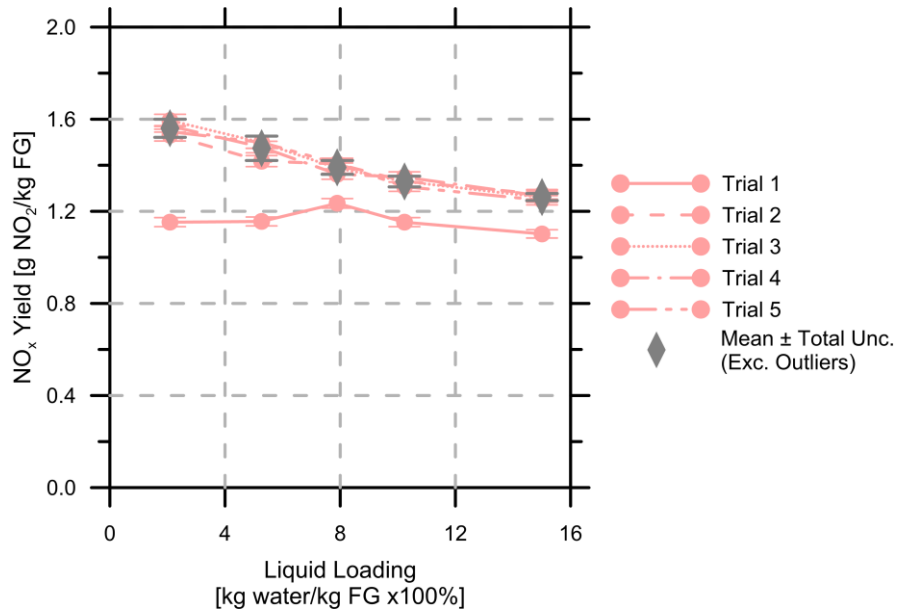


**Figure D.3: NO<sub>x</sub> yield of Heavy 4 flare gas at 109.45 SLPM versus liquid loading of 19 μm 15% aqueous NaCl. Instrument bias errors are included on each individual data point. Grey diamonds represent the average of the repeated trials at each liquid loading set point. Error bars on the diamonds are the calculated total uncertainty of the average excluding any outliers.**

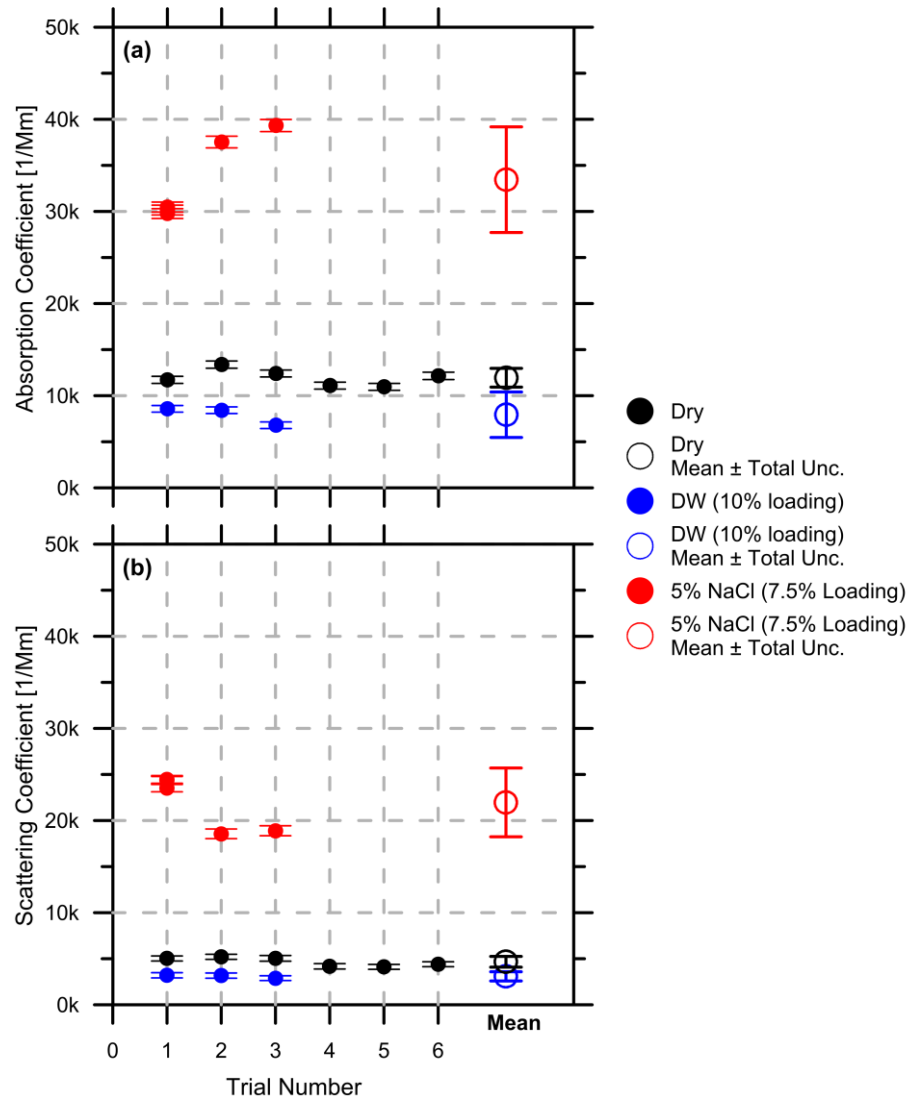


**Figure D.4: (a) absorption and (b) scattering coefficients at 405 nm of Heavy 4 flare gas at 109.45 SLPM at dry conditions and versus liquid loading of 19  $\mu\text{m}$  of DW and 5% aqueous NaCl. Instrument bias errors are included on each individual data point. Open circles represent the average of the repeated trials at each liquid loading set point. Error bars on the closed circles are instrument bias and error bars on the open circles are the calculated total uncertainty of the average excluding any outliers.**

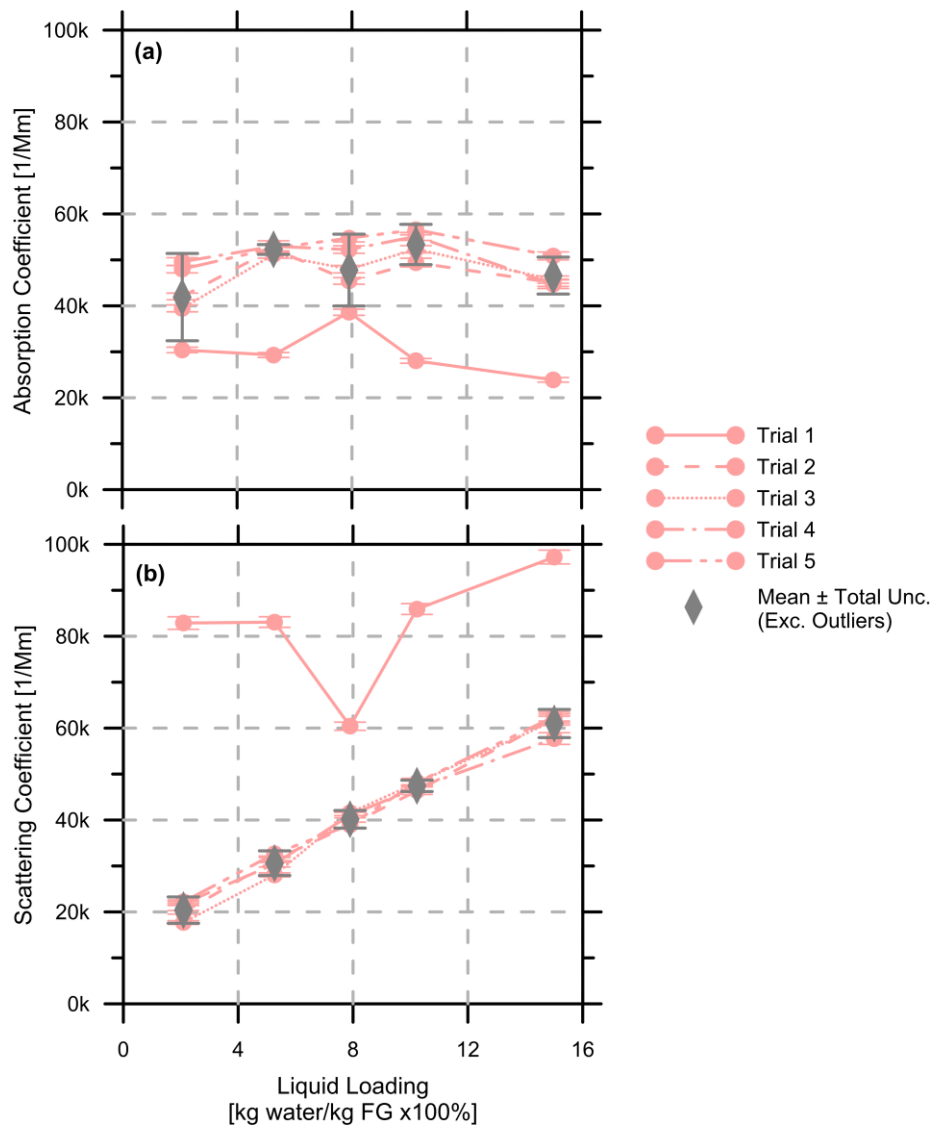


**Figure D.5: (a) absorption and (b) scattering coefficients at 405 nm of Heavy 4 flare gas at 109.45 SLPM versus liquid loading of 19  $\mu\text{m}$  15% aqueous NaCl. Instrument bias errors are included on each individual data point. Grey diamonds represent the average of the repeated trials at each liquid loading set point. Error bars on the diamonds are the calculated total uncertainty of the average excluding any outliers.**

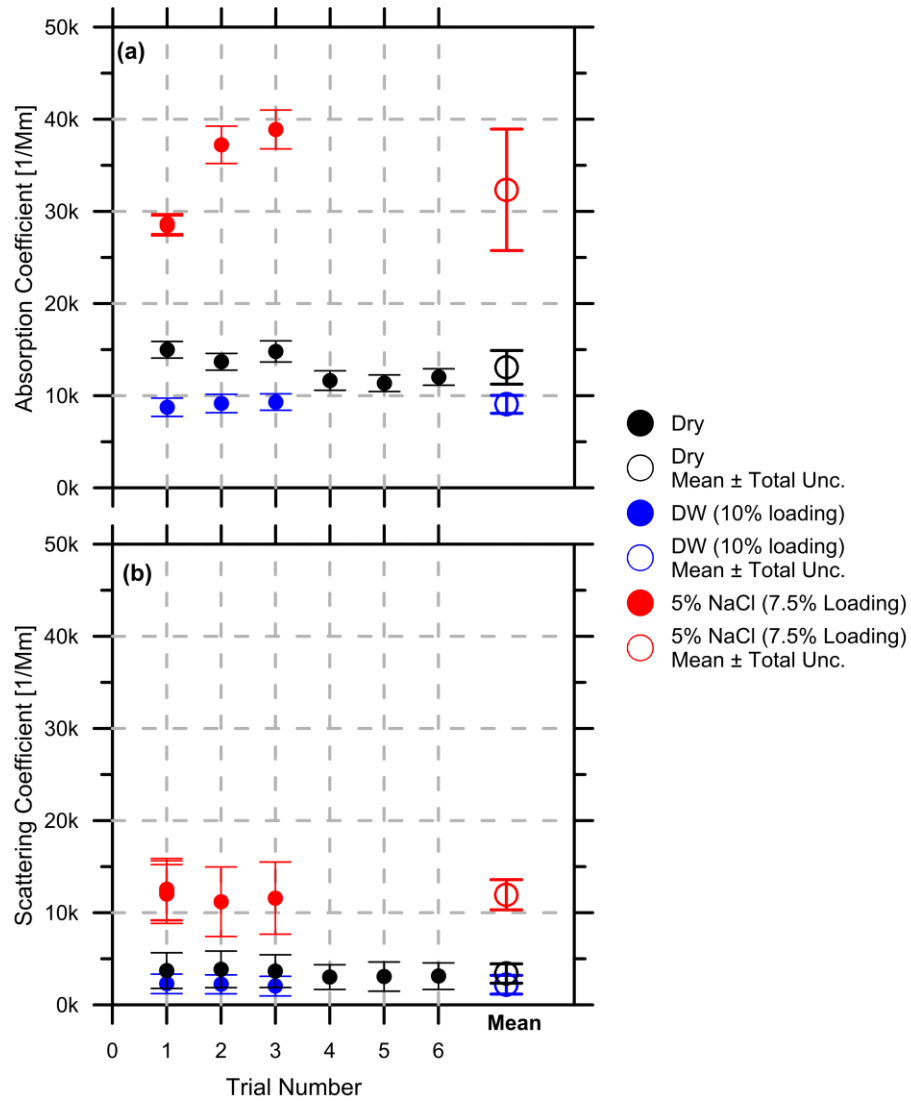


**Figure D.6: (a) absorption and (b) scattering coefficients at 532 nm of Heavy 4 flare gas at 109.45 SLPM at dry conditions and versus liquid loading of 19  $\mu\text{m}$  of DW and 5% aqueous NaCl. Instrument bias errors are included on each individual data point. Open circles represent the average of the repeated trials at each liquid loading set point. Error bars on the closed circles are instrument bias and error bars on the open circles are the calculated total uncertainty of the average excluding any outliers.**

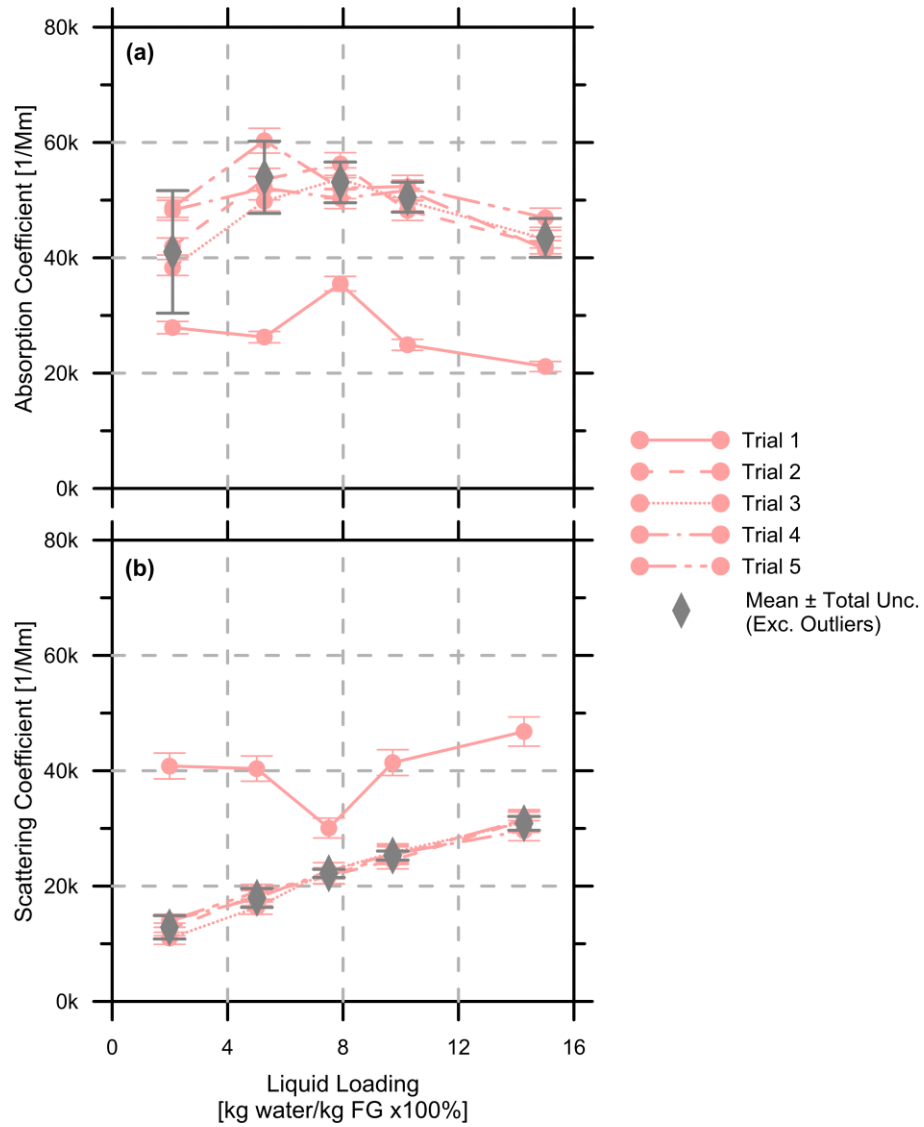


**Figure D.7: (a) absorption and (b) scattering coefficients at 532 nm of Heavy 4 flare gas at 109.45 SLPM versus liquid loading of 19  $\mu\text{m}$  15% aqueous NaCl. Instrument bias errors are included on each individual data point. Grey diamonds represent the average of the repeated trials at each liquid loading set point. Error bars on the diamonds are the calculated total uncertainty of the average excluding any outliers.**

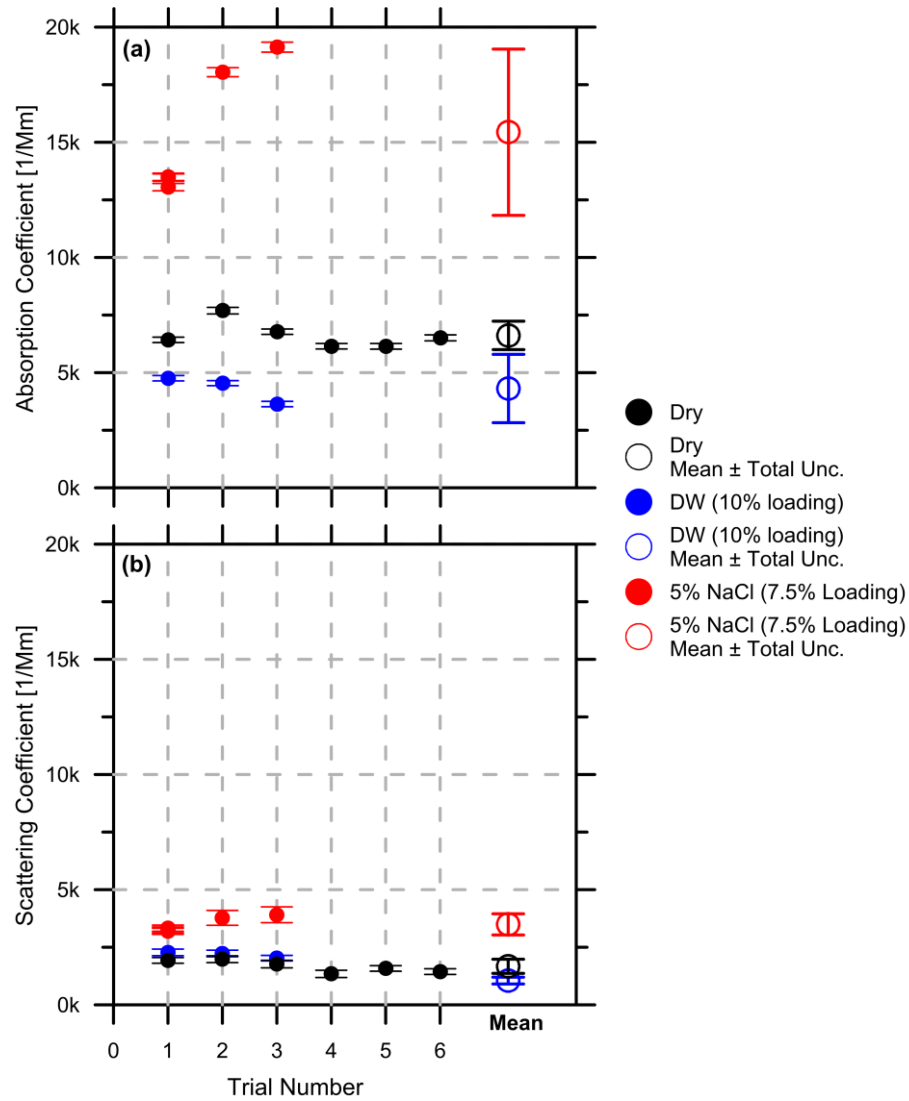


**Figure D.8: (a) absorption and (b) scattering coefficients at 870 nm of Heavy 4 flare gas at 109.45 SLPM at dry conditions and versus liquid loading of 19  $\mu\text{m}$  of DW and 5% aqueous NaCl. Instrument bias errors are included on each individual data point. Open circles represent the average of the repeated trials at each liquid loading set point. Error bars on the closed circles are instrument bias and error bars on the open circles are the calculated total uncertainty of the average excluding any outliers.**

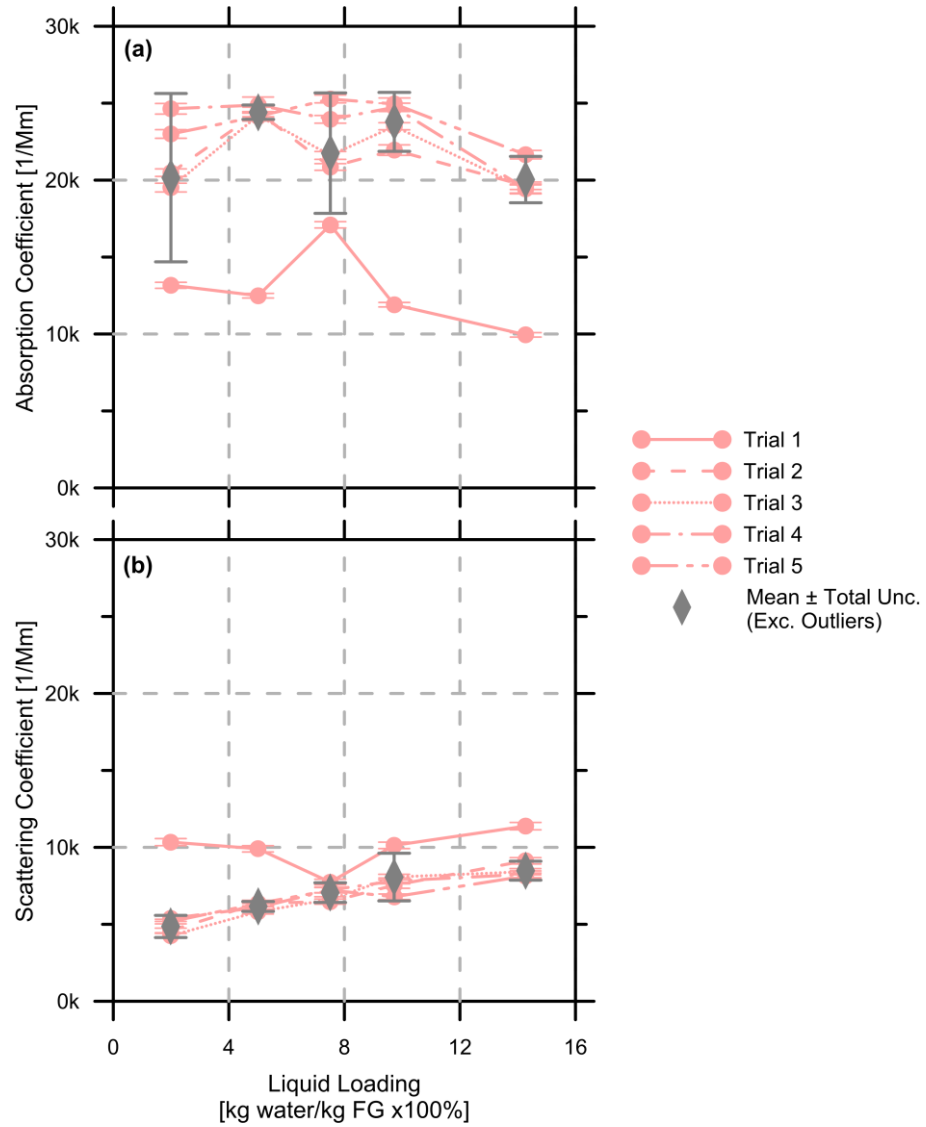


**Figure D.9: (a) absorption and (b) scattering coefficients at 870 nm of Heavy 4 flare gas at 109.45 SLPM versus liquid loading of 19  $\mu$ m 15% aqueous NaCl. Instrument bias errors are included on each individual data point. Grey diamonds represent the average of the repeated trials at each liquid loading set point. Error bars on the diamonds are the calculated total uncertainty of the average excluding any outliers.**

# Appendix E

## Scattering and Absorption Characteristics at 532 nm and 870 nm

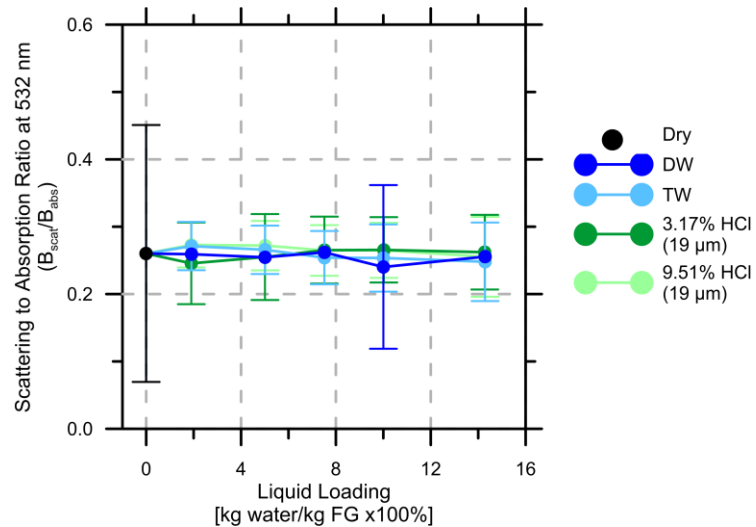


**Figure E.1:** Measured scattering to absorption coefficient ratios at 532 nm for 19 μm aerosols of DW, TW, 3.17% HCl and 9.51% HCl. Error bars represent total uncertainties, which were directly calculated for the dry flame and the flame with 19 μm aerosols of DW at 10% loading. Plotted uncertainties for other cases were estimated based on the measured precision of a similar case.

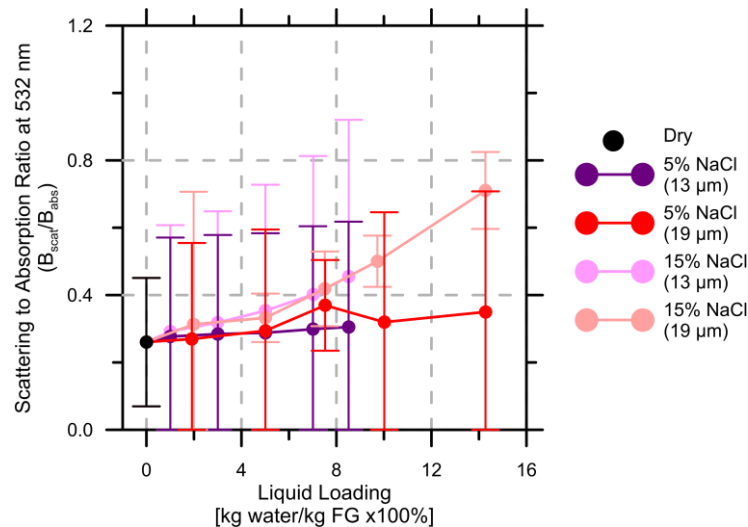


**Figure E.2:** Measured scattering to absorption coefficient ratios at 532 nm for 13 and 19 μm aerosols of 5% and 15% NaCl solutions. Error bars represent total uncertainties, which were directly calculated for the dry flame and the flames with 19 μm aerosols of 5% NaCl at 7.5% loading and 19 μm aerosols of 15% NaCl at all loadings. Plotted uncertainties for other cases were estimated based on the measured precision of a similar case.

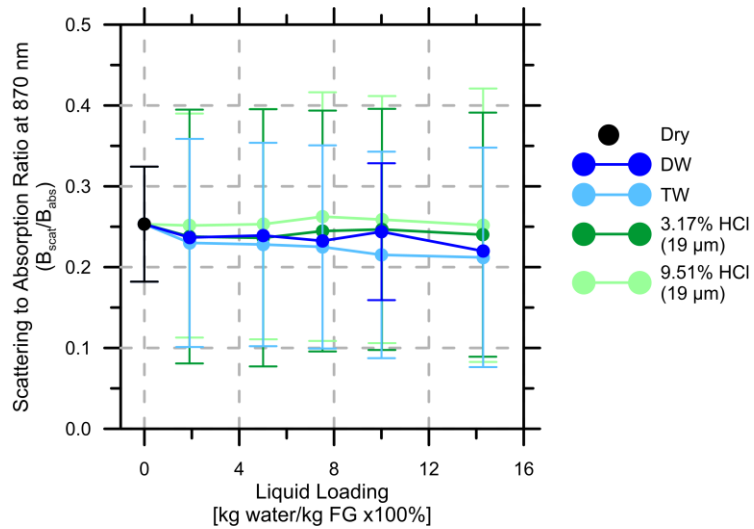


**Figure E.3: Measured scattering to absorption coefficient ratios at 870 nm for 19 μm aerosols of DW, TW, 3.17% HCl and 9.51% HCl. Error bars represent total uncertainties, which were directly calculated for the dry flame and the flame with 19 μm aerosols of DW at 10% loading. Plotted uncertainties for other cases were estimated based on the measured precision of a similar case.**

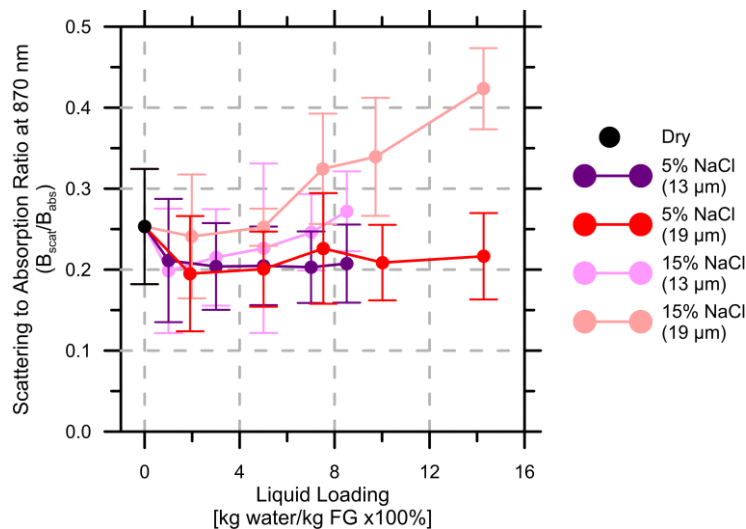


**Figure E.4: Measured scattering to absorption coefficient ratios at 870 nm for 13 and 19 μm aerosols of 5% and 15% NaCl solutions. Error bars represent total uncertainties, which were directly calculated for the dry flame and the flames with 19 μm aerosols of 5% NaCl at 7.5% loading and 19 μm aerosols of 15% NaCl at all loadings. Plotted uncertainties for other cases were estimated based on the measured precision of a similar case.**

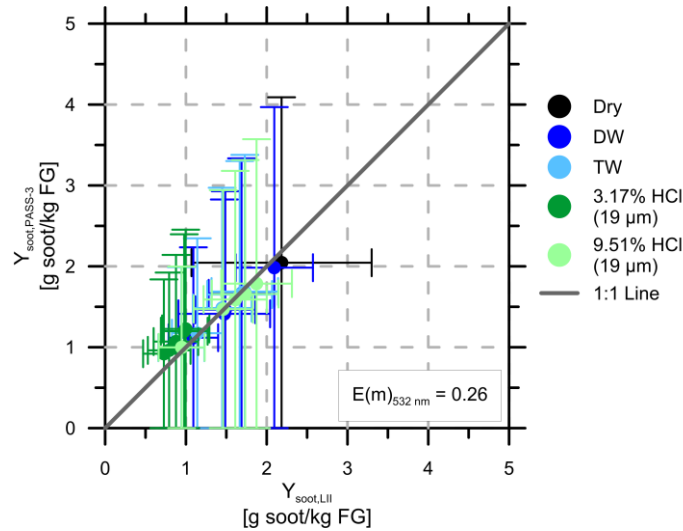


**Figure E.5: Comparison of soot yields derived from PASS-3 measurements at 532 nm and LII measurements. Results are shown for the dry flame and for flames injected with 19  $\mu\text{m}$  aerosols of DW, TW, and 3.17% and 9.51% HCl solutions. An effective  $E(m)_\lambda$  value was estimated by scaling the soot yields derived from the PASS-3 measurements to match those derived from the LII measurements. Error bars represent total uncertainties, which were directly calculated for the dry flame and the flame with 19  $\mu\text{m}$  aerosols of DW at 10% loading and dry flames. Plotted uncertainties for other cases were estimated based on the measured precision of a similar case.**

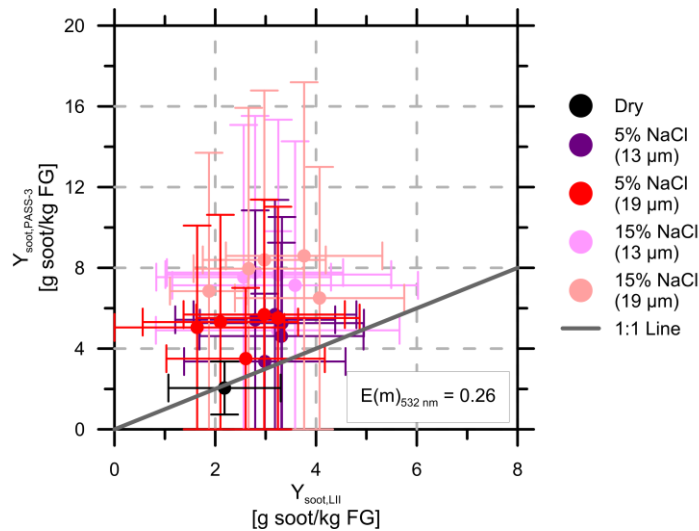


**Figure E.6: Perceived soot yields from the LII measurements versus the PASS-3 measurements at 532 nm from flames with injected 13 and 19  $\mu\text{m}$  aerosols of 5% and 15% NaCl solutions. Error bars represent total uncertainties, which were directly calculated for the 19  $\mu\text{m}$  aerosols of 5% NaCl at 7.5% loading and 19  $\mu\text{m}$  aerosols of 15% NaCl at all loadings. Plotted uncertainties for other cases were estimated based on the measured precision of a similar case.**

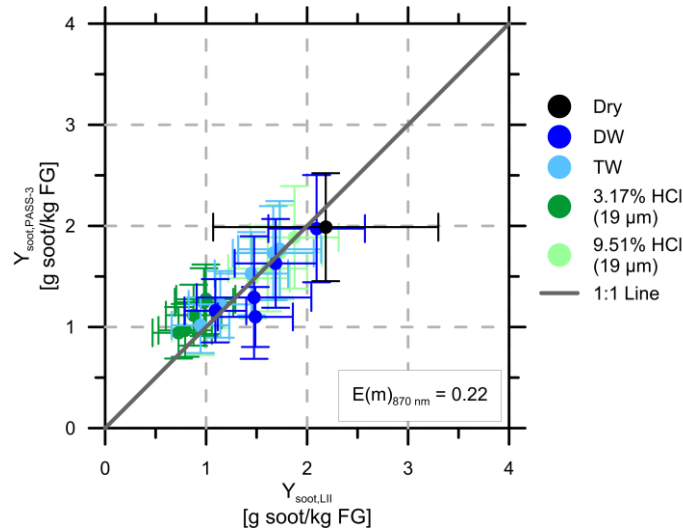


**Figure E.7: Comparison of soot yields derived from PASS-3 measurements at 870 nm and LII measurements. Results are shown for the dry flame and for flames injected with 19  $\mu\text{m}$  aerosols of DW, TW, and 3.17% and 9.51% HCl solutions. An effective  $E(m)_\lambda$  value was estimated by scaling the soot yields derived from the PASS-3 measurements to match those derived from the LII measurements. Error bars represent total uncertainties, which were directly calculated for the dry flame and the flame with 19  $\mu\text{m}$  aerosols of DW at 10% loading and dry flames. Plotted uncertainties for other cases were estimated based on the measured precision of a similar case.**

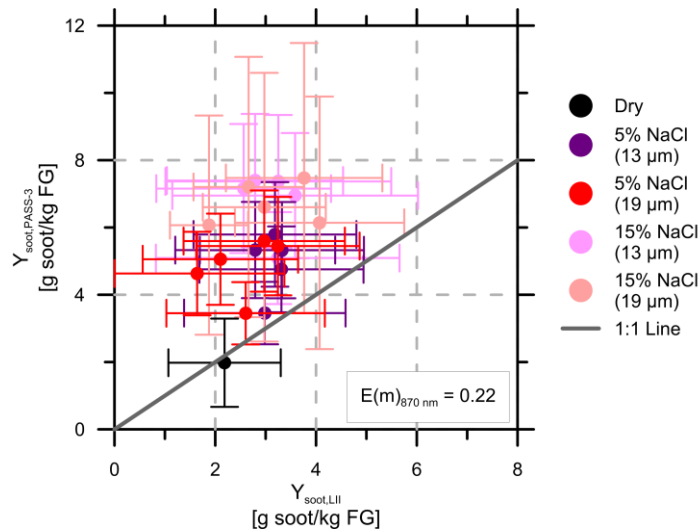


**Figure E.8: Perceived soot yields from the LII measurements versus the PASS-3 measurements at 870 nm from flames with injected 13 and 19  $\mu\text{m}$  aerosols of 5% and 15% NaCl solutions. Error bars represent total uncertainties, which were directly calculated for the 19  $\mu\text{m}$  aerosols of 5% NaCl at 7.5% loading and 19  $\mu\text{m}$  aerosols of 15% NaCl at all loadings. Plotted uncertainties for other cases were estimated based on the measured precision of a similar case.**